Ultrasonic Atomization—Its Periodic Characteristics Involving Liquid-Fountain Oscillations Associated with Mist Generation

Graduate School of Science and Engineering
Doshisha University

Author: Xiaolu WANG
Supervisor: Prof. Katsumi TSUCHIYA

Kyoto, Japan
March, 2023

Contents

Chapter 1

General Introduction

Ultrasonic wave is a sinusoidal pressure wave with frequencies higher than the limit of the human hearing range, usually around 16 or 20 kHz. These waves are often classified according to criteria of their power, frequency and application, as summarized in **Fig. 1.1** and **Table 1.1** (Legay *et al.*, 2011; Yao *et al.*, 2020).

Waves between 20 and approximately 100 kHz are defined as "low frequency ultrasound" or "power ultrasound," which is usually transmitted at high power levels (> 10 W) (Legay *et al.*, 2011; Yao *et al.*, 2020). The potential of power ultrasound involves physical and chemical processes. The physical processes are mainly due to the mechanical effects of high intensity waves in a medium, while the chemical processes are the chemical effects caused by ultrasonic cavitation in liquids. Its high intensity ultrasonic irradiation can disrupt a fluid bulk to produce cavitation or acoustic steaming, which has a powerful macroscopic effect for heat transfer enhancement. Thus, it is generally used for heat and mass transfer processes intensification (Huo *et al.*, 2018; Liu *et al.*, 2018; Buliard-Sauret *et al.*, 2019).

In the intermediate range of 100 kHz–1 MHz, it is known as intermediate or moderate ultrasound (Tamidi *et al.*, 2021). In this range, ultrasound waves propagate through liquid medium and generate various types of flow motion even at a molecular scale (Rahimi *et al.*, 2013). It is widely applied in sonochemical reactor to increase the sonochemical reaction rate. It has been shown that, for sonochemical yield, mid-range frequency ~300–500 kHz are those that are most productive (Beckett and Hua, 2001; Koda *et al.*, 2003; Yasuda *et al.*, 2007; Kanthale *et al.*, 2008).

Above 1 MHz, it is considered "high frequency ultrasound" or "low power ultrasound" (usually less than 10 W) and does not affect the medium of propagates (Legay *et al.*, 2011; Tamidi *et al.*, 2021). It is therefore particularly used for medical diagnostics or nondestructive material control (Patterson and Miller, 2019).

One of the primary applications of ultrasound technology—liquid atomization—spans a wide range of frequencies from 20 kHz to 5 MHz, and is important in many industrial processes, including spray drying (Aghamohammadi *et al.*, 2019; Arun *et al.*, 2020), film coating

(Guan *et al.*, 2020; Khan *et al.*, 2020), incineration and combustion of liquid fuels (Meng *et al.*, 2016), the manufacture of emulsions (nano-emulsions) (Zhu *et al.*, 2017), etc. The most significant advantages of ultrasonic atomization over conventional atomization are the production of particles of the same size and low energy consumption.

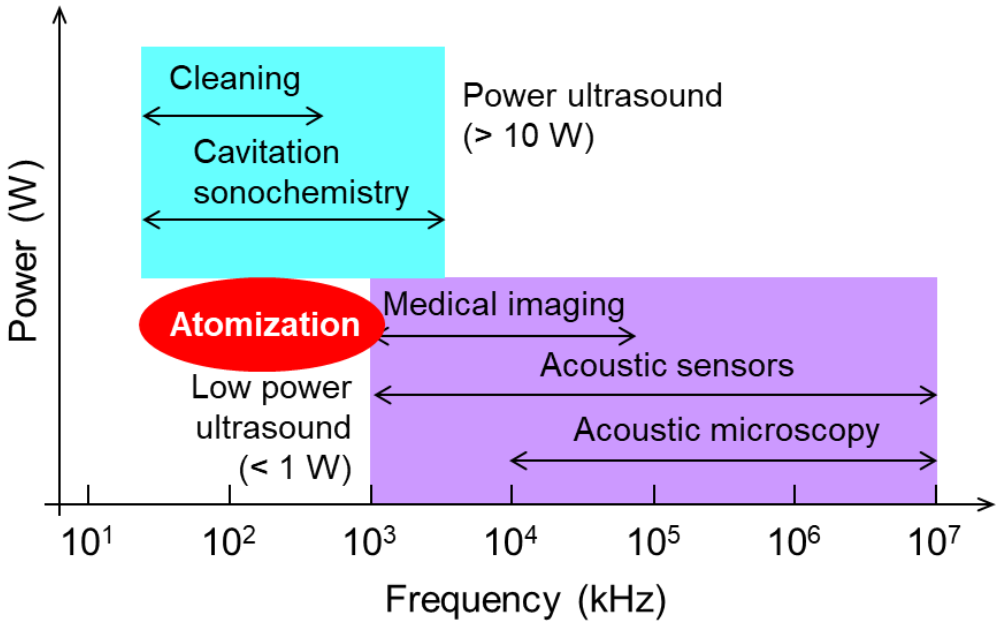

Figure 1.1 Utilizations of ultrasound according to frequency and power (from Legay *et al.*, 2011).

According to the mechanism of sound wave generation, ultrasonic atomizers are classified into two general types: electrical-driven types and gas-driven types. Electrically driven types of ultrasonic atomizers are divided into two main categories: piezoelectric ceramic transducers and variable magnet transducers. Piezoelectric ceramic transducers are widely used in the industry, mostly as horn types or plate types, the comparison of which is illustrated in **Table 1.2**. For ultrasonic horns, the piezoelectric transducer is placed inside a nozzle and has a low flow rate through the transducer, which is affected by mechanical waves. This process usually requires the fluid to be transported through other devices such as pumps, connecting pipes, and nozzles. It is known as the dynamic fluid method (Mirzabe *et al.*, 2022). In most cases, it uses low frequency ultrasound in the range of 20–100 kHz and atomizes droplets of 10–200 μm in size (Raian and Pandit, 2001; Ramisetty *et al.*, 2013; Zhang *et al.*, 2021; Zhang and Yuan, 2022). For plate transducers, the piezoelectric transducer is installed in the

bottom of the container, and a volume of fluid with a certain height is poured into the container, which is called the static fluid method. The method is characterized by irradiation at a high driving frequency (MHz), a liquid fountain will emerge from its free surface and micro- to nano-sized droplets could be generated rpm the fountain (Donnelly *et al.*, 2004; Yasuda *et al.*, 2005; Kobara *et al.*, 2010; Kirpalani and Suzuki, 2011; Kudo *et al.*, 2017).

Table 1.1 Some industrial uses of ultrasound (after Yao *et al.*, 2020)

Process	Field	Application/benefits/fundamental theory
Solid-liquid	Welding	Nonlinear effects (cavitation and acoustic flow) Improved mechanical properties, adept surface quality, improved material flow, and uniform grain growth.
	De-icing	ultrasonic piezoelectric actuators can produce high frequency vibrations and local shears at the locations of ice accretion to weaken the interface and subsequently deice the surface with normal impulse forces. More energy saving.
Liquid-liquid	Chemical reactions	Mannich-type reactions, Aza-Michael reactions, stille coupling reactions, oxidation reactions, phase transfer catalyzed reactions, chemical synthesis and catalytic transesterification process. Higher reaction rate or shorter reaction time, lower energy consumption, better catalyst effectiveness and less use of hazardous raw materials participating.
	Heat transfer enhancement	Cavitation produces a bundle of jet-flow that enhance fluid mixing, reduce thermal boundary layer of the solid–liquid interface, suppress the formation of fouling, and hence increase convective heat transfer coefficient.
	Extraction	Bioactive compounds extraction from natural products including herb, plants, vegetables and fruits. Intensify the extraction process, shorten the extraction time and increase yield of extracts.
	Atomization	Humidification, aroma diffusion, film coating, spray drying. Short processing time, Under normal temperature and pressure, non-thermal process, liquid-liquid separation without chemical reaction.
	Cleaning	Ultrasonic cleaning uses high-frequency, high-intensity sound waves in a liquid to facilitate or enhance the removal of foreign contaminants from surfaces submerged in an ultrasonically activated liquid. Clean a submerged component by the generation and implosion of cavitation bubbles on the fouled surface.
	Oil recovery	Ultrasonic crude oil viscosity reduction, ultrasonic demulsification/dehydration, ultrasonic plugging removal, ultrasonic descaling/ anti-scaling. High adaptability, simple operation, low cost and no pollution to environment
Gas-liquid	Drying	Synergistically with other drying techniques, such as convective drying, microwaves, vacuum and freezing, to accelerate the drying process. Greatly accelerate the drying process and shorten the drying time without causing a noticeable temperature increase in the materials.
	Air cleaning	Industrial gas cleaning, new dust removal technology. Orthokinetic and hydrodynamic interactions are the predominant mechanisms, while other effects, such as radiation force, acoustic streaming, and turbulence, can play an important role in promoting these interactions.

An ultrasonic horn operating at low frequencies produces primarily travelling waves that favor the production of larger bubbles that collapse violently and are unstable in nature. This contributes to both an increase in radical production and bubbles instability. Conversely, a plate transducer operating at high frequencies may be advantageous with the acoustic streaming generated which hinders coalescence, and increases the growth rate and mass transfer, contributing to further instability and fragmentation (Wood *et al.*, 2017). In addition to their smaller size, the particles have a more uniform size distribution, increasing their absorption by plant tissue. Due to these advantages, plate atomizers are widely used not only in industry but also in the fields of fine chemicals, pharmaceutical, medical device manufacturing and biotechnology (Naidu *et al.*, 2022).

Table 1.2 Comparison of solutions atomized by different ultrasonic devices

Atomization devices	Driving frequency	Particle peak size (μm)	Solution	References
Horn type (Dynamic fluid method)	36, 54, 60, 80 kHz	10–140	Water, Glycerol Ethanol	Zhang and Yuan (2022)
	36 kHz	30–110	Water, Glycerol SDS	Zhang *et al.* (2021)
	20, 40, 130 kHz	60–200	Water, Glycerol Methanol, CMC	Ramisetty *et al.* (2013)
	20 kHz	50–200	Glycerol, SLS	Raian and Pandit (2001)
Plate type (Static fluid method)	200, 430, 950 kHz 1.6, 2.4 MHz	0.01–10	Water	Kudo *et al.* (2017)
	2.4 MHz	4–8	Water, Ethanol	Kirpalani and Suzuki (2011)
	2.4 MHz	0.01–1	Water, Ethanol	Kobara *et al.* (2010)
	2.4 MHz	1–8	Ethanol	Yasuda *et al.* (2005)
	1.52–2.42 MHz	2–4	Water, Glycerol	Donnelly *et al.* (2004)

References

Aghamohammadi, S., M. Haghighi and A. Ebrahimi, "Pathways in particle assembly by ultrasound-assisted spray-drying of kaolin/SAPO-34 as a fluidized bed catalyst for methanol to light olefins," *Ultrason. Sonochem.*, **53**, 237–251 (2019). https://doi.org/10.1016/j.ultsonch.2019.01.009.

Arun, B. S., V. Mariappan and V. Maisotsenko, "Experimental study on combined low temperature regeneration of liquid desiccant and evaporative cooling by ultrasonic atomization," *Int. J. Refrig.*, **112**, 100–109 (2020). https://doi.org/10.1016/j.ijrefrig.2019.11.023.

Beckett, M. A. and I. Hua, "Impact of ultrasonic frequency on aqueous sonoluminescence and sonochemistry," *J. Phys. Chem. A.*, **105,** 3796–3802 (2001). https://doi.org/10.1021/jp003226x.

Bulliard-Sauret, O., J. Berindei, S. Ferrouillat, L. Vignal, A. Memponteil, C. Poncet, J. M. Leveque and N. Gondrexon, "Heat transfer intensification by low or high frequency ultrasound: Thermal and hydrodynamic phenomenological analysis," *Exp. Therm Fluid Sci.*, **104**, 258–271 (2019). https://doi.org/10.1016/j.expthermflusci.2019.03.003.

Donnelly, T. D., J. Hogan, A. Mugler, N. Schommer and M. Schubmehl, "An experimental study of micron-scale droplet aerosols produced via ultrasonic atomization," *Phys. Fluids*, **16**, 2843 (2004). https://doi.org/10.1063/1.1759271.

Guan, R., F. Zou, Z. Weng, P. Zhou, Y. Liao, Z. Su and L. Huang, "On a highly reproducible, broadband nanocomposite ultrasonic film sensor fabricated by ultrasonic atomization-assisted spray coating," *Adv. Eng. Mater.*, **22**, 2000462 (2020). https://doi.org/10.1002/adem.202000462.

Hou, T., Y. Chen, Z. Wang and C. Ma, "Experimental study of fouling process and antifouling effect in convective heat transfer under ultrasonic treatment," *Appl. Therm. Eng.*, **140**, 671–678 (2018). https://doi.org/10.1016/J.APPLTHERMALENG.2018.04.021.

Kwedi-Nsah, L.-M. and T. Kobayashi, "Ultrasonic degradation of diaminobenzidine in aqueous medium," *Ultrason. Sonochem.*, **52**, 69–76 (2019). https://doi.org/10.1016/j.ultsonch.2018.11.007.

Kanthale, P., M. Ashokkumar and F. Grieser, "Sonoluminescence, sonochemistry (H_2O_2 yield) and bubble dynamics: frequency and power effects," *Ultrason. Sonochem.*, **15**, 143–150

(2008). https://doi.org/10.1016/j.ultsonch.2007.03.003.

Khan, S., S. Chen, Y. Ma, M. ul Haq, Y. Li, M. Nisar, R. Khan, Y. Liu, J. Wang and G. Han, "Structural and hydrophilic properties of TiN films prepared by ultrasonic atomization assisted spray method under low temperature," *Surf. Coat. Technol.*, **393**, 125824 (2020). https://doi.org/10.1016/j.surfcoat.2020.125824.

Kirpalani, D.M. and F. Toll, "Revealing the physicochemical mechanism for ultrasonic separation of alcohol–water mixtures," *J. Chem. Phys.*, **117**, 3874–3877 (2002). https://doi.org/10.1063/1.1495849.

Kobara, H., M. Tamiya, A. Wakisaka, T. Fukazu and K. Matsuura, "Relationship between the size of mist droplets and ethanol condensation efficiency at ultrasonic atomization on ethanol–water mixtures," *AIChE J.*, **56**, 810–814 (2010). https://doi.org/10.1002/aic.12008.

Koda, S., T. Kimura, T. Kondo and H. Mitome, "A standard method to calibrate sonochemical efficiency of an individual reaction system," *Ultrason. Sonochem.*, **10**, 149–156 (2003). https://doi.org/10.1016/S1350-4177(03)00084-1.

Kudo, T., K. Sekiguchi, K. Sankoda, N. Namiki and S. Nii, "Effect of ultrasonic frequency on size distributions of nanosized mist generated by ultrasonic atomization," *Ultrason. Sonochem.*, **37**, 16–22 (2017). https://doi.org/10.1016/j.ultsonch.2016.12.019.

Legay, M., N. Gondrexon, S. Le Person, P. Boldo and A. Bontemps, "Enhancement of heat transfer by ultrasound: Review and recent advances," *Int. J. Chem. Eng.*, **2011**, 670108 (2011). https://doi.org/10.1155/2011/670108.

Liu, F., S. Chen and J. Lee, "Feasibility study of heat transfer enhancement by ultrasonic vibration under subcooled pool condition," *Heat Transfer Eng.*, **39**, 654–662 (2018). https://doi.org/10.1080/01457632.2017.1325672.

Meng, X., W. de Jong and T. Kudra, "A state-of-the-art review of pulse combustion: Principles, modeling, applications and R&D issues," *Renew. Sustain. Energy Rev.*, **55**, 73–114 (2016). https://doi.org/10.1016/j.rser.2015.10.110.

Mirzabe, A.H., A. Hajiahmad, A. Fadavi and S. Rafiee, "Design of nutrient gas-phase bioreactors: A critical comprehensive review," *Bioprocess Biosyst. Eng.*, **45**, 1239–1265 (2022). https://doi.org/10.1007/s00449-022-02728-6.

Naidu, H., O. Kahraman and H. Feng, "Novel application of ultrasonic atomization in the manufacturing of fine chemical, pharmaceuticals, and medical devices," *Ultrason. Sonochem.*, **86**, 105984 (2022). https://doi.org/10.1016/j.ultsonch.2022.105984.

Patterson, B. and D.L. Miller, "Acoustic fountain and atomization at liquid surfaces excited by diagnostic ultrasound," *Ultrasound Med. Biol.*, **45**, 2162–2173 (2019). https://doi.org/10.1016/j.ultrasmedbio.2019.04.007.

Rahimi, M., N. Azimi and F. Parvizian, "Using microparticles to enhance micromixing in a high frequency continuous flow sonoreactor," *Chem. Eng. Process*, **70**, 250–258 (2013). https://doi.org/10.1016/j.cep.2013.03.013.

Rajan, R. and A.B. Pandit, "Correlations to predict droplet size in ultrasonic atomization," *Ultrason.*, **39**, 235–255 (2001). https://doi.org/10.1016/S0041-624X(01)00054-3.

Ramisetty, K.A., A.B. Pandit and P.R. Gogate, "Investigations into ultrasound induced atomization," *Ultrason. Sonochem.*, **20**, 254–264 (2013). https://doi.org/10.1016/j.ultsonch.2012.05.001.

Tamidi, A.M., K.K. Lau and S.H. Khalit, "A review of recent development in numerical simulation of ultrasonic-assisted gas-liquid mass transfer process," *Comput. Chem. Eng.*, **155**, 107498 (2021). https://doi.org/10.1016/j.compchemeng.2021.107498.

Wood, R.J., J. Lee and M.J. Bussemaker, "A parametric review of sonochemistry: Control and augmentation of sonochemical activity in aqueous solutions," *Ultrason. Sonochem.*, **38**, 351–370 (2017). https://doi.org/10.1016/j.ultsonch.2017.03.030.

Yao, Y., Y. Pan and S. Liu, "Powe ultrasound and its application: A state-of-the-art review," *Ultrason. Sonochem.*, **62**, 104722 (2020). https://doi.org/10.1016/j.ultsonch.2019.104722.

Yasuda, K., T. Torii, K. Yasui, Y. Iida, T. Tuziuti, M. Nakamura and Y. Asakura, "Enhancement of sonochemical reaction of terephthalate ion by superposition of ultrasonic fields of various frequencies," *Ultrason. Sonochem.*, **14**, 699–704 (2007). https://doi.org/10.1016/j.ultsonch.2006.12.013.

Yasuda, K., Y. Bando, S. Yamaguchi, M. Nakamura, A. Oda and Y. Kawase, "Analysis of concentration characteristics in ultrasonic atomization by droplet diameter distribution," *Ultrason. Sonochem.*, **12**, 37–41 (2005). https://doi.org/10.1016/j.ultsonch.2004.05.008.

Zhang, Y. and S. Yuan, "Phase, pressure and velocity evolution and atomization characteristics

of multiple Faraday waves in ultrasonic atomization: Experiments and simulations," *Int. J. Multiph. Flow*, **156**, 1104223 (2022). https://doi.org/10.1016/j.ijmultiphaseflow.2022.104223.

Zhang, Y., S. Yuan and L. Wang, "Investigation of capillary wave, cavitation and droplet diameter distribution during ultrasonic atomization," *Exp. Therm. Fluid Sci.*, **120**, 110219 (2021). https://doi.org/10.1016/j.expthermflusci.2020.110219.

Zhu, Y., J. Luo, Y. Lu, B. Gao, D. Wang, G. Yang and C. Guo, "Ultrasonic-assisted emulsion synthesis of well-distributed spherical composite CL-20@PNA with enhanced high sensitivity," *Mater. Lett.*, **205**, 94–97 (2017). https://doi.org/10.1016/j.matlet.2017.06.064.

Chapter 2

Ultrasonic atomization: overview and applications

Ultrasonic atomization (UsA) techniques have been employed as—with an ultimate goal being—a flexible green alternative for energy-efficient processes including: gas–liquid mass transfer enhancement/intensification (Dong *et al.*, 2015; Tamidi *et al.*, 2021), wastewater treatment (Mahamuni and Adewuyi, 2010; Kunde and Sehgal, 2021), air purification (Tay *et al.*, 2016, 2017; Wei *et al.*, 2019; Marjanian *et al.*, 2021), drug delivery (Dalmoro *et al.*, 2013; Kaur *et al.*, 2021), as well as solvent–solute (or particles) separation (Nii and Oka, 2014; Kim *et al.*, 2015; Hinman *et al.*, 2019) and/or concentration (Kirpalani and Suzuki, 2011; Mai *et al.*, 2019).

Atomization of liquid into the air attained through submerged ultrasound irradiation will involve the formation of liquid fountain. The mechanism of mist generation is basically summarized as capillary waves caused by the instability of the fountain surface and cavitation caused by the collapse of the cavitation bubbles inside the fountain. Currently, there is a lack of explanation for the correlation between liquid flow phenomena induced by ultrasound irradiation in liquid media and liquid fountain formation, so it is essential to understand the principles of unique flow behavior under the influence of ultrasound waves.

2.1 Ultrasound propagation and induced effects

Ultrasonic irradiation in liquid media causes chemical and physical effects. The former is known as the sonochemical effect and refers to the pyrolysis of chemical species inside the cavitation bubble (hot spots) and free radical reaction (oxidation and reduction) under localized high temperature and pressure conditions. The latter is a sonophysical effect, including acoustic streaming, liquid fountain formation and atomization.

2.1.1 Heating effect

When the ultrasound wave propagates through the liquid medium, some of the ultrasound energy is converted to heat energy, producing a heating effect to the liquid medium (Tamidi *et al.*, 2021). Kirpalani and Suzuki (2011) studied the concentration mechanism of aqueous eth-

anol solutions at an ultrasound frequency of 2.4 MHz. At both 24 and 10°C, the temperature at the base of the ultrasonic fountain was higher than the feed temperature by approximately 14°C. With the same ultrasound frequency, Mai *et al.* (2019) observed an increase in the temperature of the ILs-water solution from 25 to 31°C in 5 hours during ultrasonic atomization. The increase of liquid temperature is expected whenever ultrasound irradiation technology is used. To maintain the liquid temperature at certain conditions, external cooling mechanisms such as air fans, cooling water jackets, cooling coils, or water baths are typically installed (Hamai *et al.*, 2009; Kojima *et al.*, 2010; Lee *et al.*, 2022).

2.1.2 Acoustic cavitation

When ultrasound at a sufficiently high intensity is irradiated in aqueous phase, a sound energy field is formed and the molecules in the sound field oscillate at their mean position. The sound pressure at each position changes sinusoidally, resulting in periodic repetitions of the compression period (positive sound pressure) and the rarefaction period (negative sound pressure). The molecules are drawn apart in the rarefaction period and cavities are formed at high sound pressure which is enough to break the interaction of molecules. These cavities acting as bubbles, hence termed as cavitation bubbles, grow by diffusion and coalescence unless they are dissolved. At a maximum size, which is mainly determined by applied ultrasound frequency, the bubbles violently collapse. This microscale process is termed the acoustic cavitation (the formation, growth, and collapse of bubbles) (Son, 2016).

Two types of cavitation phenomena are generally considered (Legay *et al.*, 2011; Wood *et al.*, 2017; Tamidi *et al.*, 2021); stable (or non-inertial) cavitation bubbles last over many cycles and may be considered weakly and symmetrically oscillating. Transient (or inertial) cavitation bubbles grow extensively over a few cycles until the energy from the ultrasound can no longer be absorbed, then the forces acting on the bubble dominate causing instability and violent collapse. This in turn can lead to fragmentation into smaller bubbles that may repeat the process or dissolve. Accordingly, the concept has been visualized as “dancing bubbles” as, upon fragmentation, a larger bubble ejects tiny bubbles and can be seen to dance by counteraction (Lohse and Hilgenfeldt, 1997; Hatanaka *et al.*, 2002; Wood *et al.*, 2017).

As the bubbles collapse, the extreme temperatures and pressures generated inside induce

two unique cavitation effects, namely sonochemical and sonophysical effects (Lee *et al.*, 2008; Son *et al.*, 2012; Giannakoudakis *et al.*, 2020; Asakura and Yasuda, 2021; Lee *et al.*, 2022). Physically, the effect occurs as a result of violent microscale oscillations resulting in the formation of micro-stream and high-velocity micro-jets. It has been widely used for surface cleaning (Mason, 2016; Yamashita and Ando, 2019), soil washing (Son *et al.*, 2011), and emulsification (Yasuda *et al.*, 2012). In most cases, ultrasound with a frequency between 20 and 40 kHz is the most effective frequency for sonophysical effects. Sonochemical effects include the pyrolysis of chemical species inside the cavitation bubble and free radical reaction (oxidation and reduction). The main application is the decomposition of harmful substances, degradation of aqueous pollutants; moreover, it can result in noticeable synergistic effects when it is combined with other advanced oxidation techniques (AOP) (Sekiguchi *et al.*, 2010, 2011; Rahimi *et al.*, 2015; Ono *et al.*, 2020).

In recent years, many researchers have investigated the effects of frequency ranging from 20 kHz to 2.4 MHz on the various chemical substances, as summarized in **Table 2.1**. Hung and Hoffmann (1999) tested six frequencies including 20, 205, 358, 500, 618 and 1,078 kHz for the sonochemical degradation of chlorinated hydrocarbons using three different sonoreactors and found that the highest degradation rate constant was obtained at 500 kHz. Vega *et al.* (2018) used ultrasound from 215 to 1134 kHz for the degradation of endocrine-disrupting compound, reported maximum degradation rate at 574 kHz. Liu *et al.* (2018) investigated the effect of ultrasonication on the removal of phycocyanin from the water at 120–800 kHz, and 200 kHz was found to be optimum. In addition, Koda *et al.* (2003) tested three methods including the Fricke reaction, the KI dosimetry and TPPS dosimetry from 20 kHz to 1.2 MHz, revealed that the sonochemical efficiency was highest at 200–500 kHz. Therefore, based on the literature reported, it would be reasonable to suggest that the optimal frequency ranges from 200 to 500 kHz for two kinds of sonochemical reactions including pyrolysis for volatile/hydrophobic compounds and radical reactions for less volatile/hydrophilic compounds (Son, 2016).

Table 2.1 Examples of sonochemical degradation of aromatic compounds and organic halo gen compounds

Category	Driving frequency	Chemical substances	Optimum frequency	References
Harmful materials	20, 205, 358, 500,1078 kHz	Chlorinated hydrocarbons	500 kHz	Hung and Haffmann (1999)
Carcinogens	205, 358, 618,1071 kHz	1,4-dioxane	358 kHz	Beckett and Hua (2001)
Aromatic compound	20, 34, 500 kHz	Phenol	500 kHz	Entezari *et al.* (2003)
Harmful materials	20, 200, 500, 800 kHz	4-chlorophenol	200 kHz	Jiang *et al.* (2006)
Harmful materials	35, 74, 170, 300, 1000 kHz	chlorobenzene, chloroform, carbon tetrachloride	300 kHz	Lim *et al.* (2011)
Endocrine disrupting compounds, Antiseptic agents	20, 215, 373, 574, 856, 1134 kHz	Benzophenone-3, Triclosan	574 kHz	Vega *et al.* (2018, 2019)
Carcinogens	43, 141, 500 kHz	3,30-Diaminobenzidine	500 kHz	Kweidi-Nsah and Kobayashi (2018)
Pigments	120, 200, 400, 800 kHz	Phycocyanin	200 kHz	Liu *et al.* (2018)
Aromatic compound	44, 300, 1000 kHz	Phenol	1000 kHz	Wood *et al.* (2020)

2.1.3 Acoustic streaming

Acoustic streaming is the major phenomenon that may arise from the propagation of ultrasonic waves into a liquid. Lighthill (1978) reported that acoustic streaming ensues from the dissipation of acoustic energy which permits the gradient in momentum, thereby the fluid flow. In other words, acoustic streaming also refers to the high velocity flow generated by ultrasonic waves that is initiated from the transducer surface, exerting and impinging force on the fluid and pushing it to circulate in the vessel (Sajjadi *et al.*, 2015; Tamidi *et al.*, 2021).

Depending on the scale of the fluids motion, acoustic streaming can be classified into three types (Zarembo, 1971): Eckart streaming; Schlichting streaming; and Rayleigh streaming. The first, also called quartz wind, is generated in a non-uniform free sound field, whose scale is much larger than the acoustic wavelength. Therefore, the fluid flow is generated by the attenuation of the acoustic waves into the bulk of the medium. The last two are intrinsically related. Schlichting streaming is described as the vortex motion generated in a viscous

boundary layer on the surface of an object placed in a sound field, whose scale is much smaller than the wavelength (Frampton *et al.*, 2004). Rayleigh streaming is the vortex generated outside the boundary layer in a standing wave field, whose scale is comparable to the acoustic wavelength (Hammarstrom *et al.*, 2012).

Researchers have recently been interested in the quantification of flow fields and the relationship between flow fields and sonochemical reactions. The common techniques used to measure sound velocity are laser Doppler anemometry (LDA) and particle image velocimetry (PIV). Chouvellon *et al.* (2000) measured the liquid velocity distribution using PIV and observed that the velocity increased as viscosity increased. Kojima *et al.* (2010) studied the pattern of liquid flow in a rectangular sonochemical reactor at 490 kHz using LDA technique. As the input power increased, the liquid flow changes from random to convective. The process of convection can be viewed as a stirrer that transfers liquid from the bottom to the top surface, thus improving sonochemical efficiency. On the other hand, it is important to understand the unique flow behavior under the influence of ultrasound waves. To this end, numerical approach should be effective owing to its incorporation of the relevant mechanisms explicitly formulated and realized in the numerical/CFD simulation; some experimental approach with advanced measurement techniques could also be helpful (Abolhasani *et al.*, 2012; Parvizian *et al.*, 2012).

2.1.4 Acoustic fountain

Ultrasonic fountains will be generated when the ultrasonic wave has sufficient intensity and streaming momentum to overcome the liquid threshold limit (Tamidi *et al.*, 2021). It is shaped like a cone (Laborde *et al.*, 2020; Xu *et al.*, 2013, 2016; Kim *et al.*, 2021); its diameter is essentially the same as the diameter of the transducer (Xu *et al.*, 2016); and its height "step-increased with an increase in the acoustic pressure," with a step increment of half the ultrasound wavelength (Xu *et al.*, 2016; Kim *et al.*, 2021).

A particular morphology, *i.e.*, a liquid fountain in the form of a corrugated jet, or a chain of beads of submillimeter diameter in contact is formed when properly adjusted/selected the input power density (Tomita, 2014; Simon *et al.*, 2015). Atomization occurs from the fountain surface when the ultrasound intensity is higher than the liquid-dependent threshold. Re-

cently, ultrasonic atomization has become a popular method for absorbing and eliminating hazardous gases due to the acoustic fountains and atomization's ability to increase the gas-liquid interface area during the absorption process. Yusof *et al.* (2019) claimed that the formation of acoustic streaming and fountain are responsible for increasing the physical and chemical absorption of CO_2. **Table 2.2** summarized the results of high-frequency ultrasound-assisted gas absorption.

Table 2.2 Gas absorption and removal by high-frequency ultrasound-assisted

Removal/ absorption	Driving frequency	Remarks	References
CO_2	1.7 MHz	High frequency ultrasonic of was used for the physical absorption of CO_2 in a water batch system under elevated pressure, the mass transfer process of absorption and desorption can be enhanced up to 80 and 20 times, respectively.	Tay *et al.* (2016)
K_2CO_3, CO_2	1.7 MHz	The ultrasonic-assisted absorption system with 20 wt% potassium carbonate (without promoter) has provides 1.75 times higher volumetric mass transfer coefficient than the Piperazine (PZ) promoted potassium carbonate using stirring method. The absorption rate has been increased up to 32 times as compared to the case without ultrasonic irradiation.	Tay *et al.* (2017)
NO_x, SO_2	1.7 MHz	Using the in-series double-oxidation subsystems with H_2O_2 concentration of 6 wt%, pH 5.0, and the reaction temperature of 130°C, the removal efficiencies of SO_2 and NO are respectively 100% and 89.3% at the short residence time of 1.8 s, and the removal efficiency of NO can be increased to 100% as the residence time is longer than 3.7 s.	Wei *et al.* (2019)
CO_2	1.7 MHz	The presence of high frequency ultrasonic irradiation has enhanced the absorption process 7 times higher as compared to the case of without ultrasonic irradiation.	Yusof *et al.* (2020)
CO_2	1.7 MHz	A comparative study using water absorbent indicated that applying ultrasonic atomization led to five times faster CO_2 absorption rate compared to the conventional stirring method and 20 times faster rate compared to the silent condition (no ultrasonic and no stirring).	Marjanian *et al.* (2021)
$PM_{1.0}$, $PM_{2.5}$, PM_{10}	1.7 MHz	Submicron water droplets of 800 nm in mean diameter were generated by ultrasonic module combined passive nonporous membrane, the removal efficiencies were 78, 60 and 32% for PM_{10}, $PM_{2.5}$ and $PM_{1.0}$, respectively.	Kim *et al.* (2021)

Tay *et al.* (2016) used a high ultrasound frequency of 1.7 MHz to assist CO_2 absorption in a water batch system. Significant absorption enhancement rates up to 80-fold has been achieved. Subsequently, different absorbents, including MEA and potassium carbonate, were tested and exhibited enhancement of mass transfer performance up to 60 and 32-fold, respectively, as compared to the case without ultrasonic irradiation (Tay *et al.*, 2017a, 2017b). For

the different solvents such as DEA, NaOH, Na_2CO_3 and H_2O, Marjanian *et al.* (2021) showed that the ultrasonic atomization system resulted in a 20-fold increase in CO_2 absorption compared to the conditions of no ultrasound and no agitation. In addition, the problem of airborne particulate matter (PM), which has been of great interest in recent years, Kim *et al.* (2021) reported that submicron water droplets of 800 nm in mean diameter were generated by ultrasonic humidifier combined passive nonporous membrane, the removal efficiencies were 78, 60 and 32% for PM_{10}, $PM_{2.5}$ and $PM_{1.0}$, respectively.

2.2 Mechanistic of ultrasonic atomization

Faraday (1831) firstly reported that the frequency of the surface waves is half of the excitation frequency. The ultrasonic atomization process has been studied extensively, and it is believed that capillary waves are generated on the free surface of a liquid sheet as a result of faraday excitation. Later, Rayleigh (1879) described the first mathematical model to explain the bubble collapse in incompressible liquids, in his attempts to explain the physical mechanisms involved in ultrasound propagation in liquids. Wood and Loomis (1927) produced for the first time an aerosol spray from a liquid film using ultrasounds. When the wavy patterns reach certain instability levels, the hydrodynamic structures form jets that can destabilize into droplets and this is the basic physical phenomena forming ultrasonic sprays through the capillary wave hypothesis (Panão, 2022). It should be noted, however, that the driving frequency range in this hypothesis is within the kHz range. When the range was increased to MHz, Söllner (1936) performed a series of experiments in liquids of varying viscosity under low pressure and elevated temperature conditions and concluded that atomization was caused by the violent collapse of bubbles. Then, Antonevich (1959) concluded, based on high-speed experimental observations of low-frequency planar ultrasound, that atomization was a combination of cavitation bubble collapse and capillary-wave instabilities, and proposed that the size of the emitted droplets depended on the mechanism of their release: capillary-wave instability tended to result in smaller and uniform droplets, while cavitation-bubble collapsing could lead to larger droplets of different sizes on the microscale.

2.2.1 Capillary-wave hypothesis

According to capillary wave theory, the ultrasonic excitation generates capillary waves at the liquid-gas interface, which become unstable leading to pinch-off of droplets from the wave peaks (Deep *et al.*, 2018). Lang (1962) predicted the mean diameter of droplets generated from the capillary wave crest for water, oil and molten wax, at driving frequencies of 10–800 kHz, and developed a relationship between the mean diameter of the ejected droplets (D_{50}) and the capillary wavelength (λ), given by

$$D_{50} = C_{\lambda}\left(\frac{8\pi\sigma}{\rho f^2}\right)^{\frac{1}{3}} \tag{2.1}$$

Where f is the driving frequency and C_{λ} a proportionality constant. Lang (1962) was experimentally determined $C_{\lambda} = 0.34$, where D_{50} is the median droplet size of the number (not volume) distribution (Deep *et al.*, 2018; Panão, 2022). For MHz-range ultrasound, Donnelly *et al.* (2004) conducted atomization experiments in the 1.52–2.42 MHz range and confirmed that $C_{\lambda} = 0.35 \pm 0.03$. Yasuda *et al.* (2005) used ultrasonic irradiation at 2.4 MHz and determined $C_{\lambda} = 0.96$. Recently, Kooij *et al.* (2019) reported experimental relationships for $C_{\lambda} = 0.17 - 0.65$, depending on the ultrasonic device. The relationship between characteristic droplet size and capillary wavelength does not well-established or restricted to a single value. This is because the droplet characteristic sizes considered by different authors may be different, eventually leading to these differences (Panão, 2022).

2.2.2 Cavitation (Boiling) hypothesis

Cavitation hypothesis states that as ultrasound wave from the transducer propagates through the liquid phase, during the rarefaction phase of the sound wave, the local pressure of the fluid drops below the vapor pressure leading to the formation of vapor bubbles. During the compression phase, these cavitation bubbles implode violently and emit hydraulic shocks which rupture the liquid-gas interface causing atomization (Deep *et al.*, 2018). In early studies of the mechanism of atomization under MHz ultrasound radiation, the theory has been sometimes rejected due to the high threshold power for cavitation in this frequency range. Recent reports provide supporting evidence that cavitation occurs at MHz frequencies.

Harada *et al.* (2009) observed the spatial distribution of sonoluminescence and light dur-

ing ultrasonic atomization of water by 2.4 MHz ultrasonic irradiation. The brightest part is immediately below the bulk surface of the liquid. It is clear that cavitation occurs when atomizing conditions exist. A high-speed camera was used by Barreras *et al.* (2002) to observe the atomization from mound water by irradiation at 1.6 MHz. There were reports of black spots near the surface of the water, which were attributed to cavitation bubbles.

In our earlier visualization experiments (Fujita and Tsuchiya, 2013), the formation of a chain-of-beads fountain was recorded with an ultrahigh-speed video camera [0.25 mega-frames/s with the corresponding resolution of 312×260 pixels (4.2 μm/pixel), 0.5-μs exposure; Shimadzu HPV-1] equipped with a tele-microscope and a xenon lamp focused with an optical lens on the same optical axis as the camera. **Fig. 2.1** shows a series of captured images when a high-frequency transducer with a *flat disk* oscillating at 2.4 MHz was used at a lower input power intensity (2.0 W/cm^2). A cavity—being not clear whether it is comprised of a single void/bubble or a tightly clustered cavitating bubbles—was observed near the central interior of a fountain bead. As this cavity moved across laterally towards the gas–liquid interface, *droplet bursting* eventually occurred. It was hypothesized in this particular case that droplet bursting would originate from cavitation bubbles. Cavitation is clearly evident in these findings, but it may not be the only mechanism that produces ultrasonic atomization.

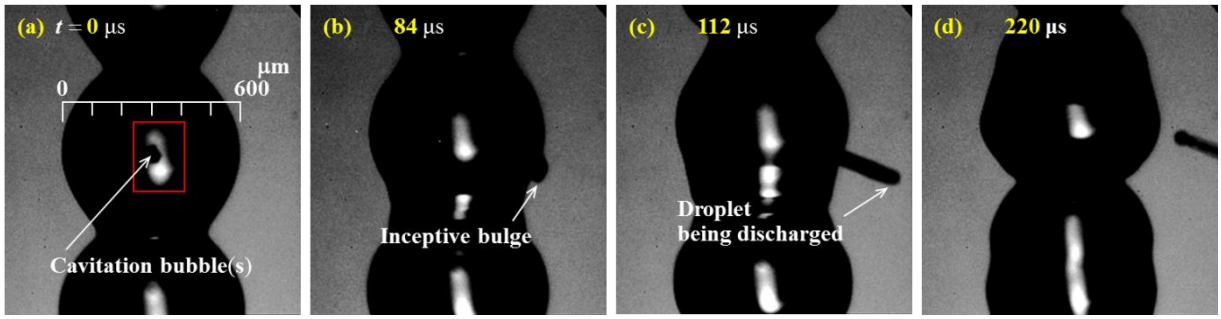

Figure 2.1 Selected portion of liquid fountain for 39-wt% (20-mol%) ethanol solution, emanating in the form of a chain of "spherical beads" as the ultrasound (2.4 MHz, 2.0 W/cm^2) is irradiated. Generation of a bursting droplet and deformation of the "host" bead from spherical towards diamond shape: the bursting droplet originates from cavitation bubble(s) moving from central region to lateral surface (gas–liquid interface) of the fountain. The whole process shown at (a) 0, (b) 84, (c) 112 till (d) 220 μs elapsed from an arbitrary time (after Fujita and Tsuchiya, 2013).

2.2.3 Conjunction hypothesis

Bouguslavskii and Eknadiosyants (1969) proposed a "conjunction theory", according to which the periodic hydraulic shock from the cavitation disturbance interacts with the finite amplitude capillary waves and excite them to form droplets. Currently, this is the most accepted theory of atomization (Rozenberg,1973; Barreras *et al.*, 2002; Simon *et al.*, 2012, 2015 Tomita, 2014; Zhang *et al.*, 2020).

Over the past decade or so, high-speed imaging techniques have improved significantly, allowing for more detailed UsA processes to be observed. Ramisetty *et al.* (2013) investigate the phenomena of ultrasonic atomization by capturing the actual process of the formation of droplets using photographic analysis. On the basis of the theory of Rajan and Pandit (2001), an empirical correlation was developed to predict droplet size based on the variation of droplet size with different operating parameters. The correlation is presented as

$$D_{50} = 0.00154\left(\frac{\pi\sigma}{\rho f^2}\right)^{0.33} + 0.00154\left(\frac{\pi\sigma}{\rho f^2}\right)^{0.13} N_{Oh}^{-0.111} N_{We}^{-0.154} N_{In}^{-0.033} \qquad (2.2)$$

Where f is the driving frequency, N_{Oh} is the ratio between the internal liquid viscosity to surface force and vibrational amplitude, N_{We} is the ratio between the aerodynamic forces and the surface tension forces, N_{In} is the ultrasonic intensity number. The first term in the Eq. (2.2) is the representation of the ultrasonic atomization based on the capillary wave phenomena, the second term is the representation of dependence of the liquid physicochemical properties on the ultrasonic atomization with capillary and cavitation phenomena (Ramisetty *et al.*, 2013).

For more detailed visual support, Tomita (2014) investigated, through high-speed (as high as 50,000-fps) photography, atomization of a liquid jet generated by interactions of 1-MHz focused ultrasound with a water surface. He identified the threshold conditions for surface elevation and jet breakup associated with drop separation and spray formation. His specific findings include that: a single drop separated from the tip of a jet without spraying; multiple—typically doublet of—beaded water masses were formed, moving upwards to produce a vigorous jet; and cavitation was detected near the center of the primary bead at the jet's leading part, accompanied by fine droplets (*i.e.*, sprayed mist) at the neck between the primary and secondary beads—claimed to occur due to the *collapse of capillary waves*.

2.3 Applications of ultrasonic atomization

Ultrasonic atomization (to be abbreviated in this study as UsA) is often regarded as a means of generating rather uniform distribution of a swarm of small droplets, or mist. In reality, the UsA-generated mist consists of droplets spanning wide ranges of their diameters, from micro- down to nanometers, as has been reported by, *e.g.*, Yano *et al.* (2006), Kobara *et al.* (2010), Sekiguchi *et al.* (2010), Nii and Oka (2014), Kudo *et al.* (2017), and Guo *et al.* (2021). A variety of its applications are evidenced in the fields including: selective separation or concentration of solute from organic solution (*e.g.*, Sato *et al.*, 2001), spray cooling (Arun *et al.*, 2020), film coating (Guan *et al.*, 2020; Khan *et al.*, 2020), preparation of micro- and/or nano-sized powder (*e.g.*, Cai *et al.*, 2019), air purification (Tay *et al.*, 2016, 2017; Wei *et al.*, 2019; Marjanian *et al.*, 2021), medical applications (*e.g.*, Simon *et al.*, 2012; Dalmoro *et al.*, 2013; Perra *et al.*, 2021), and applications utilizing sonochemical reactions/reactors associated with cavitation (*e.g.*, Lee *et al.*, 2008, 2011; Kojima *et al.*, 2010; Son *et al.*, 2011; Choi *et al.*, 2019).

2.3.1 Droplet size distribution

Regarding the UsA also as highly energy-efficient in producing small droplets—requiring no external heat input, researchers have paid much attention to the droplet size distribution (DSD) of generated mist, in particular, from an operational viewpoint. For instance, Zhang *et al.* (2021), using an ultrasonic nebulizer with a vibrating tip directed downwards for spreading tube-guided liquid, examined the effects on the DSD of the UsA input power, the carrier-gas flowrate, the liquid-phase temperature, liquid surface tension and viscosity, among other parameters to suggest possible combination(s) of the optimum operating parameters that control the DSD. Kudo *et al.* (2017) investigated specifically the effects of UsA driving frequency on the DSD to show that the diameter of nano-droplets in mist decreased with increasing ultrasonic frequency. Kooij *et al.* (2019) studied the DSD using three different types of atomizers/nebulizers: surface acoustic wave (SAW) nebulizer, ("Grove"-type) nebulizer chip and (submerged-type) mist maker, and concluded that the DSD was thoroughly determined by the extent and nonlinear structure as well as size distribution of "corrugated ligaments". In regard to the DSD and measurement methods for mist generated via UsA are summarized in **Table 2.3**.

Table 2.3 Droplet size distribution and analysis methods during ultrasonic atomization

Solution	Driving frequency	Method	Median droplet size	References
Ethanol-water	2.4 MHz	Laser light scattering (SPR7340)	4–7 μm	Yasuda *et al.* (2005)
Ethanol, water, DBS-Na+KCl	2.4 MHz	Laser diffraction method (AEROTRAC SPR7340)	Ethanol 5%: 6 μm Ethanol 10%: 3 μm Water: 5 μm DBS-Na+KCl: 2 μm	Nii *et al.* (2006)
Ethanol, water	2.4 MHz	Small-angle x-ray scattering (SAXS)	1 and 100 nm	Yano *et al.* (2007)
Ethanol-water	2.4 MHz	Light scattering (SMPS), Laser diode light scattering (HPC)	30 nm and 1 μm	Kobara *et al.* (2010)
Ethanol-water	2.4 MHz	Laser diffraction system (Sympatec LDI)	5–9 μm	Kirpalani and Suzuki (2011)
Pure water, Tap water	200, 430, 950, 1600, 2400 kHz	Particle spectrometer (WPS)	Pure water: 25.5–86.7 nm Tap water: 79.9–212 nm	Kudo *et al.* (2017)
Water	SAWN: 9.6 MHz Nebulizer chip: 105±5 kHz Mist marker: 1700±50 kHz	Laser diffraction method (Malvern Spraytec)	SAWN: 1.1 μm Nebulizer chip: 9.5 μm Mist marker: 5.6 μm	Kooij *et al.* (2019)
Water, glycerol, SDS	Horn type : 36 kHz	Malvern laser particle size meter	20–150 μm	Zhang *et al.* (2021)

Most studies reported that ultrasonic atomization produces droplets in the size of micrometers with a normal distribution (Yasuda *et al.*, 2005; Yano *et al.*, 2007; Naidu *et al.*, 2022). However, the analytical methods used in these studies were limited in their ability to detect droplets of sizes less than the order of micrometers, and the Laser diffraction system they used has a minimum detectable size of 0.1 μm. Yano *et al.* (2007) analyzed the droplet size obtained in the atomization of ethanol, water and their mixtures using small-angle x-ray scattering (SAXS). For ethanol, highly uniform liquid droplets with a diameter of 1 ± 0.2 nm are observed, which is 10^{-3} times less than predicted value by Lang (1962). On the other hand, the droplets size of water was in the order of micrometers. Kobara *et al.* (2010) determined the droplet size in water, 5 mol% and 50 mol% ethanol solutions. For water and 5 mol% ethanol solutions, two peaks were observed at around 30 nm and 1 μm. It was also reported that the size of the droplets decreased as the temperature increased and increased as the carrier gas flow rate increased. More importantly, it is highly plausible that generation of the two kinds of droplets occurs by different mechanisms; that is, the nanometer droplets are generated from the surface of the liquid fountain, while the micrometer droplets are generated from the bulk (Nii *et al.*, 2006; Yano *et al.*, 2007).

2.3.2 Ethanol separation/concentration

An important scientific impact recognized for the UsA stems from one of the above-mentioned applications: Matsuura *et al.* (1995) conducted, for the first time to our knowledge, a study on ethanol separation via the UsA as a concentrating scheme—which should require to preserve specific flavors (thus to be avoided being heated)—of Japanese Sake; subsequently, Sato *et al.* (2001) showed that the concentration of ethanol in the mist after being atomized by high-frequency ultrasound greatly exceeded that in the original ethanol aqueous solution. Besides concentrating the solution itself, Nii and Oka (2014) successfully separated nanoscale solid particles from a mixture of submicron particles in suspensions—thus having attained size-selective particle separation—via UsA and proposed that particles of specific size could be separated by controlling the recovery of atomized droplets under proper UsA conditions. Typical studies on the ethanol concentration via ultrasonic atomization are summarized in **Table 2.4**.

Table 2.4 Typical studies on the ethanol concentration via ultrasonic atomization

Solution	Driving frequency	Method	Method of obtaining the concentration in mist	Enrichment radio	References
0–100 mol% Ethanol-water	2.3 MHz	–	Mass balance	2–10	Sato *et al.* (2001)
26.5 vt% Ethanol-wate	2.4 MHz	–	Mass balance	1.7–3	Yasuda *et al.* (2003)
DBS-Na, PONPEs	2.4 MHz	salt addition	Analysis of condensed mist	1.5–5	Takaya *et al.* (2005)
0–100 mol% Ethanol-water	2.4 MHz	–	Mass balance	1–5	Nii *et al.* (2006)
0–4 mol/L Ethanol-water	2.4 MHz	salt addition	Mass balance	10–30	Hamai *et al.* (2009)
39 wt% Ethanol-wate	2.4 MHz	Two cooling units in a series	Analysis of condensed mist	1.7–2.2	Tanaka *et al.* (2011)
5–9 wt% Ethanol-wate	2.4 MHz	Ultrafine bubbles (UFB)	Analysis of condensed mist	5–6.5 (without UFB) 6.6–9.4 (with UFB)	Yasuda *et al.* (2020)
Alcohols	2.4 MHz	A novel three-stage mist collection method	Analysis of condensed mist	3.2–5	Naidu *et al.* (2021)

Sato *et al.* (2001) reported that pure ethanol can be obtained directly from a solution with 10 mol% ethanol–water solution at 10 °C via ultrasonic atomization. The enrichment ratio, *e.g.*, the ratio of the concentration of the solute in the mist to that in the bulk solution, is 10. Subsequently, Yasuda *et al.* (2003) and Nii *et al.* (2006) conducted numerous experiments still

unable to replicate the results. The enrichment ratios of 5 and 3, respectively, in the separation of ethanol−water solutions (10 mol %) in batch ultrasonic separators at 10°C. With the addition of K_2CO_3 or $(NH_4)_2SO_4$ to ethanol−water solutions in ultrasonic atomization, Hamai *et al.* (2009) obtained enrichment rates of 20 to 30. In addition, salts that exhibit weak interactions with water molecules such as Na_2CO_3 or NaCl, did not result in improvement in enrichment radio. The authors explained that ethanol exists in surface excess at the interface and is removed in the form of mist. In the presence of salt, the amount of water around the ethanol molecules decreases leading to an increase in the concentration of ethanol at the interface. In these studies, the mist was not collected and analyzed directly. Instead, the concentration and weight of the bulk solution before and after ultrasonic misting were measured, and the concentration in the mist was estimated using a mass balance (Sato *et al.*, 2001; Yasuda *et al.*, 2003; Nii *et al.*, 2006; Hamai *et al.*, 2009).

Tanaka *et al.* (2011) developed the process of collecting in two cooling stages the ethanol enriched mist—generated via an ultrasonic atomizer with continuous feed of ethanol−water solution—using two cooling units in a series. For a bulk solution with 39 wt% ethanol concentration, the concentration in the vapor phase at VLE at 0.1 MPa was 75 wt%. The concentration of condensate collected was 85 wt% in 2nd-stage and 65 wt% in 1st-stage. Yasuda *et al.* (2020) explored the combination of ultrafine bubbles (UFB, <1 μm) and ultrasonic nebulization to improve the ethanol enrichment performance of ultrasonic nebulization. For ethanol-water solutions at concentrations of 5−9 wt%, the enrichment ratios with and without UFB were 6.6−9.4 and 5−6.5, respectively. Especially, the enrichment effect by UFB was remarkable when the ethanol concentration in the solution and the flow rate of carrier gas were low. Naidu *et al.* (2021) used an ultrasonic device with a three-stages mist collection (MC) unit. Most of the vapor was collected in MC stage 1; the remaining vapor and larger mist droplets in micrometers could mostly be collected in MC stage 2; and fine droplets were collected in MC stage 3. The concentration of ethanol collected in each stage in the MC unit across the entire concentration range and followed the sequence stages 3 > 2 > 1. The results showed that the alcohols (1-butanol, ethanol, 1-propanol, and methanol) were enriched in the ultrasound-generated mist with enrichment ratios of 3.2−5.

In addition to ethanol, the researchers studied ultrasonic misting of various solutes such

as methanol, ethanol, 1-propanol, propylene glycol, glycerol, formamide, acetamide, acetic acid, propioloc acid, 2-butanone, and inorganic salts (lithium sulfate, sodium sulfate, potassium sulfate, rubidium sulfate, and cesium sulfate) in binary aqueous solutions. Alcohols and ketones were found to be enriched in the mist, whereas propylene glycol, glycerol, and amides were diluted (Yasuda *et al.*, 2005, 2014; Takaya *et al.*, 2005; Suzuki *et al.*, 2006; Mai *et al.*, 2019; Naidu *et al.*, 2021). In the case of carboxylic acids and salts, the concentration in the mist was the same as that in the bulk solution. They also reported that the hydrophilic and hydrophobic properties of solutes governed the separation characteristics in ultrasonic separation (Yasuda *et al.*, 2005, 2014; Mai *et al.*, 2019; Naidu *et al.*, 2021). Further, the atomized droplets work as a container to accommodate the target particle for separating particles of a specified size (Kim *et al.*, 2015; Hinma *et al.*, 2019). Due to the lack of understanding of the mechanism of UsA, however, it has not been systematically applied in an industrial scale yet.

2.3.3 Plausible mechanisms for ethanol separation

Despite the fact that experiments have demonstrated differences in the extent of ethanol enrichment, the mechanism of separation has been the focus of researchers. Three possible separation mechanisms have been outlined, as shown in **Fig. 2.2** (Naidu *et al.*, 2022).

Wakisaka and Matsuura (2006) explained that micro-heterogeneity in the form of ethanol and water-rich clusters in alcohol-water solutions is responsible for the enrichment of ethanol during ultrasonic atomization process. In the ethanol-water binary mixture, there are microscopically ethanol-rich clusters and water-rich clusters. Ethanol is concentrated in the smaller clusters, while water is concentrated in the larger clusters. The difference in the molecular composition in the clusters between the smaller and the larger clusters works as a key factor on the ethanol enrichment. The supportive references of this theoretical basis include Nishi *et al.* (1998), Egashira and Nishi (1998), and Dixit *et al.* (2002).

The second supported theory is the formation of surface excess of ethanol in aqueous solutions. There is a correlation between the surface and bulk structures of alcohol-water solutions. The presence of hydrophobic solutes in aqueous solutions increases the order of water surrounding the solute and locally enhances the hydrogen bonding network. This is referred to as hydrophobic hydration or iceberg formation. The strong hydrogen bonding network of wa-

ter causes a surface excess of ethanol, leading to the formation of a monolayer. Then, the ethanol exists in surface excess at the interface and is removed in the form of mist (Koga *et al.*, 2004; Yano *et al.*, 2005; Hamai *et al.*, 2009; Ballal and Chapman, 2013).

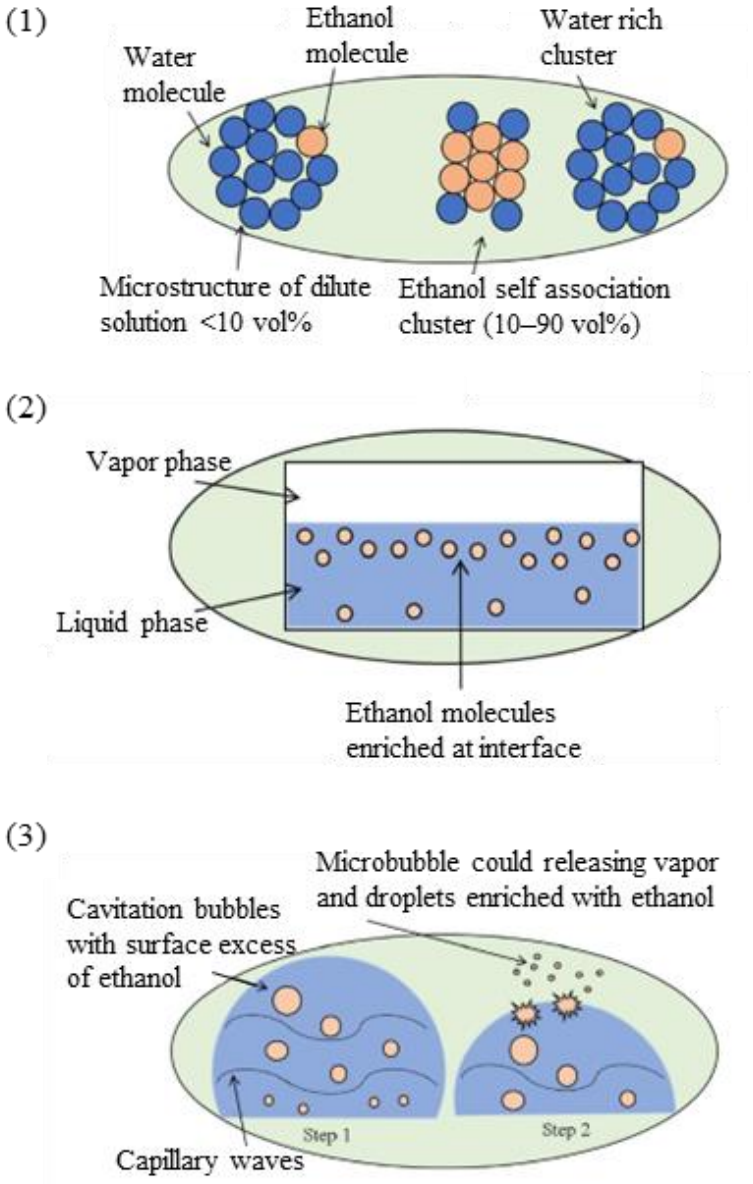

Figure 2.2 Mechanisms of ethanol enrichment in ultrasonic atomization proposed by various groups (from Naidu *et al.*, 2022).

The third mechanism combines the conjunction hypothesis from **Section 2.2** with an excess of ethanol on the surface. The first step in this process is the formation of cavitation bubbles with surface excess of ethanol in the bulk solution. These bubbles grow as they travel through the bulk solution. They move upward in the fountain jet and collapse periodically at

the surface into a clouds of microbubbles and releases vapors and droplets enriched with ethanol (Kirpalani and Toll, 2002). Suslick's group proposed the formation of nanodroplets inside the cavitation bubble, *i.e.*, the formation of concentrated nanodroplets of ethanol ejected from the fountain surface leads to enrichment by ultrasonic atomization (Flannigan and Suslick, 2007; Xu *et al.*, 2009).

2.4 Structure and dynamics of liquid fountain

Several applications of UsA have been described in the literature: the droplet size distribution (DSD) of emerging mist (*e.g.*, Kobara *et al.*, 2010; Sekiguchi *et al.*, 2010; Kudo *et al.*, 2017); and the selective separation/concentration of solute (or "targeted" suspension) into the mist with its extent and mechanisms (*e.g.*, Sato *et al.*, 2001; Nii and Oka, 2014) are involved in the formation of liquid fountain. Tsuchiya *et al.* (2011) have observed the structure and dynamics of the (general) liquid fountain visually. It has been identified that there are *four* representative transitions/demarcations in the acoustic fountain structure and dynamics: 1) the *onset* of a protrusion on otherwise flat free surface; 2) the *appearance* of undulation along the growing protuberance; 3) the *triggering* of emanating beads fountain out of this foundation-like region; and 4) the *induction* of droplets bursting and/or mist spreading.

For (general) liquid fountains that induction of droplets bursting and/or mist spreading, Kirpalani and Suzuki (2011) performed a visualization study of oscillating fountains formed during ultrasonic irradiation at 2.4 MHz. A milky appearance on the fountain surface during atomization indicates the presence of bubbles in the fountain. The height of the fountain increases with increasing ethanol concentration and gradually decreases after reaching a peak at 30 mol% ethanol concentration. Despite this, they do not explain how to define the height of a fountain. The liquid fountain should be supposed to grow and break up periodically.

Although the acoustic fountains play an important role in the mechanism of atomization occurrence as highlighted several times in the above description, the limitations of its high-speed imaging technology and the instability of the fountain surface have led to few reports on the dynamic of liquid fountains in general.

2.5 Research objectives and thesis structure

The aim of this doctoral thesis is to provide a dynamic elucidation through a sequence of images, captured through high-speed visualization, of periodically oscillating acoustic fountain, and an attempt to reveal factor(s) triggering mist emergence.

Chapter 1 describes the background of ultrasound-assisted technology and its applications. An overview of the chemical and physical effects that can be induced by ultrasonic irradiation in liquid media is provided in Chapter 2, as well as an explication of the principles of atomization generation and the main industrial applications of ultrasonic atomization in recent years. After giving useful introductory literature information, Chapter 3 provides the experimental details and data analysis methods of the system. Chapter 4 is focused on quantitatively elucidating the effects of the UsA driving frequency on the structure [including characteristic dimension(s)] and dynamics [*viz.*, characteristic frequency(ies)] of a chain-of-beads fountain realized under lower input power intensity. In chapter 5, the influence of ultrasonic irradiation (*i.e.*, transducer installation) angle on the liquid-fountain oscillations with mist generated intermittently was examined. Chapter 6 discusses the effects on the structure and dynamics of acoustic fountains by changing some acousto-related operating conditions, including ultrasound excitation frequency, acoustic strength or input power density, and the presence/absence of a "regulating" nozzle. A summary and an outlook are discussed in chapter 7.

References

Abolhasani, M., M. Rahimi, M. Dehbani and A. A. Alsairafi, "CFD modeling of heat transfer by 1.7 MHz ultrasound waves," *Numer. Heat Transf. Part A Appl.*, **62**, 822–841 (2012). http://doi.org/10.1080/10407782.2012.712432.

Aikawa, T. and N. Kudo, "Relation between thresholds of free radical generation and atomization under ultrasound exposure," *Jpn. J. Appl. Phys.*, **60**, SDDD13 (2021). http://doi.org/10.35848/1347-4065/abf600.

Antonevich, J. N., "Ultrasonic atomization of liquids," *IRE Trans. Ultrasonic Eng.*, **PGUE-7** 6–15 (1959).

Arun, B. S., V. Mariappan and V. Maisotsenko, "Experimental study on combined low temperature regeneration of liquid desiccant and evaporative cooling by ultrasonic atomization,"

Int. J. Refrig., **112**, 100–109 (2020). https://doi.org/10.1016/j.ijrefrig.2019.11.023.

Asakura. Y. and K. Yasuda, "Frequency and power dependence of the sonochemical reaction," *Ultrason. Sonochem.*, **81**, 105858 (2021). https://doi.org/10.1016/j.ultsonch.2021.105858.

Ballal, D. and W.D. Chapman, "Hydrophobic and hydrophilic interactions in aqueous mixtures of alcohols at a hydrophobic surface," *J. Chem. Phys.*, **139**, 114706 (2013). https://doi.org/10.1063/1.4821604.

Barreras, F., H. Amaveda and A. Lozano, "Transient high-frequency ultrasonic water atomization," *Exp. Fluids*, **33** 405–413 (2002). https://doi.org/10.1007/S00348-002-0456-1.

Beckett, M.A. and I. Hua, "Impact of ultrasonic frequency on aqueous sonoluminescence and sonochemistry," *J. Phys. Chem. A.*, **105,** 3796–3802 (2001). https://doi.org/10.1021/jp003226x.

Boguslavskii, Yu.Ya. and O.K. Eknadiosyants, "Physical mechanism of the acoustic atomization of a liquid," *Sov. Phys. Acoust.*, **15** 14–21 (1969).

Cai, Z., X.Wang, Z. Zhang, Y. Han, J. Luo, M. Huang, B. Zhang and Y. Hou, "Large-scale and fast synthesis of nano-hydroxyapatite powder by a microwave-hydrothermal method," *RSC Adv.*, **9**, 13623 (2019). https://doi.org/10.1039/c9ra00091g.

Choi, J., J. Khim, B. Neppolian and Y. Son, "Enhancement of sonochemical oxidation reactions using air sparging in a 36 kHz sonoreactor," *Ultrason. Sonochem.*, **51**, 412–418 (2019). https://doi.org/10.1016/j.ultsonch.2018.07.032.

Chouvellon, M., A. Largillier, T. Fournel, P. Boldo and Y. Gonthier, "Velocity study in an ultrasonic reactor," *Ultrason. Sonochem.*, **7**, 207–211 (2000). https://doi.org/10.1016/S1350-4177(00)00060-2.

Dalmoro, A., A.A. Barba and M. d'Amore, "Analysis of size correlations for microdroplets produced by ultrasonic atomization," *Sci. World J.*, **2013**, 482910 (2013). https://doi.org/10.1155/2013/482910.

Deep, P., C. Peng and S. Moghaddam, "Dynamics of ultrasonic atomization of droplets," *Exp. Therm. Fluid Sci.*, **92**, 243–247 (2018). https://doi.org/10.1016/j.expthermflusci.2017.11.021.

Dixit, S., J. Crain, W.C.K. Poon, J.L. Finney and A.K. Soper, "Molecular segregation ob-

served in a concentrated alcohol–water solution," *Nature*, **416**, 829–832 (2002). https://doi.org/10.1038/416829a.

Dong, Z., C. Yao, X. Zhang, J. Xu, G. Chen, Y. Zhao and Q. Yuan, "A high-power ultrasonic microreactor and its application in gas–liquid mass transfer intensification," *Lab Chip*, **15**, 1145–1152 (2015). https://doi.org/10.1039/c4lc01431f.

Donnelly, T.D., J. Hogan, A. Mugler, N. Schommer and M. Schubmehl, "An experimental study of micron-scale droplet aerosols produced via ultrasonic atomization," *Phys. Fluids*, **16**, 2843 (2004). https://doi.org/10.1063/1.1759271.

Egashira, K. and N. Nishi, "Low-frequency Raman spectroscopy of ethanol−water binary solution: Evidence for self-association of solute and solvent molecules," *J. Phys. Chem. B*, **102**, 4054–4057 (1998). https://doi.org/10.1021/jp9806359.

Entezari, M.H., C. Pétrier and P. Devidal, "Sonochemical degradation of phenol in water: a comparison of classical equipment with a new cylindrical reactor," *Ultrason. Sonochem.*, **10**, 103–108 (2003). http://doi.org/10.1016/S1350-4177(02)00136-0.

Faraday, M., "On a peculiar class of acoustical figures; and on certain forms assumed by groups of particles upon vibrating elastic surfaces," *Philos. Trans. R. Soc. Lond.*, **121**, 299–340 (1831). https://doi.org/10.1098/rspl.1830.0024.

Flannigan, D.J. and K.S. Suslick, "Emission from electronically excited metal atoms during single-bubble sonoluminescence," *Phys. Rev. Lett.*, **99**, 134301 (2007). https://doi.org/10.1103/PhysRevLett.99.134301.

Frampton, K.D., K. Minor and S. Martin, "Acoustic streaming in micro-scale cylindrical channels," *Appl. Acoust.*, **65**, 1121–1129 (2004). http://doi.org/10.1016/j.apacoust.2004.03.005.

Fujita, K. and K. Tsuchiya, "Cavitating bubble inside liquid fountain of beads associated with ultrasonic atomization," *Proc. 8th Int. Conf. Multiphase Flow (ICMF 2013)*, Paper 863/1–5 (2013).

Giannakoudakis, D., D. Lomot and J.C. Colmenares, "When sonochemistry meets heterogeneous photocatalysis: designing a sonophotoreactor towards sustainable selective oxidation," *Green Chem.*, **22**, 4896–4905 (2020). https://doi.org/10.1039/D0GC00329H.

Guan, R., F. Zou, Z.Weng, P. Zhou, Y. Liao, Z. Su and L. Huang, "On a highly reproducible,

broadband nanocomposite ultrasonic film sensor fabricated by ultrasonic atomization-assisted spray coating," *Adv. Eng. Mater.*, **22**, 2000462 (2020). https://doi.org/10.1002/adem.202000462.

Guo, Y., X. Yang, G. Li, J. Yang, L. Liu, L. Chen and B. Li, "Shear turbulence controllable synthesis of aggregated nano-particles using a swirling vortex flow reactor assisted by ultrasound irradiation," *Chem. Eng. J.*, **405**, 126914 (2021). https://doi.org/10.1016/j.cej.2020.126914.

Hamai, K., N. Takenaka, B. Nanzai, K. okitsu, H. Bandow and Y. Maeda, "Influence of adding salt on ultrasonic atomization in an ethanol–water solution," *Ultrason. Sonochem.*, **16**, 150–154 (2009). http://doi.org/10.1016/j.ultsonch.2008.07.002.

Hammarström, B., T. Laurell and J. Nilsson, "Seed particle-enabled acoustic trapping of bacteria and nanoparticles in continuous flow systems," *Lab Chip*, **12**, 4296–4304 (2012). http://doi.org/10.1039/C2LC40697G.

Harada, H., N. Iwada and K. Shiratori, "Observation of multibubble sonoluminescence from water saturated with various gases during ultrasonic atomization," *Jpn. J. Appl. Phys.*, **48**, 07GH01 (2009). https://doi.org/10.1143/JJAP.48.07GH01.

Hatanaka, S., H. Mitome, K. Yasui and S. Hayashi, "Single-bubble sonochemiluminescence in aqueous luminol solutions," *J. Am. Chem. Soc.*, **124**, 10250−10251 (2002). http://doi.org/10.1021/ja0258475.

Hinman, J. G., J. J. Hinman, B. E. Janicek, P. Y. Huang, K. S. Suslick and C. J. Murphy, "Ultrasonic nebulization for TEM sample preparation on single-layer graphene grids," *Nano Lett.*, **19**, 1938–1943 (2019). http://doi.org/10.1021/acs.nanolett.8b05117.

Hung, H-.M. and M. R. Hoffmann, "Kinetics and mechanism of the sonolytic degradation of chlorinated hydrocarbons: Frequency effects," *J. Phys. Chem. A*, **103**, 2734–2739 (1999). http://doi.org/10.1021/jp9845930.

Jiang, Y., C. Petrier and T. D. Waite, "Sonolysis of 4-chlorophenol in aqueous solution: Effects of substrate concentration, aqueous temperature and ultrasonic frequency," *Ultrason. Sonochem.*, **13**, 415–422 (2006). https://doi.org/10.1016/j.ultsonch.2005.07.003.

Kaur, J., R. R. Singh, E. Khan, A. Kumar and A. Joshi, "Piperine-loaded PLGA nanoparticles as cancer drug carriers," *ACS Appl. Nano Mater.*, **4**, 14197–14207 (2021).

https://doi.org/10.1021/acsanm.1c03664.

Khan, S., S. Chen, Y. Ma, M. ul Haq, Y. Li, M. Nisar, R. Khan, Y. Liu, J. Wang and G. Han, "Structural and hydrophilic properties of TiN films prepared by ultrasonic atomization assisted spray method under low temperature," *Surf. Coat. Technol.*, **393**, 125824 (2020). https://doi.org/10.1016/j.surfcoat.2020.125824.

Kim, D., J. Kim and S. J. Lee, "Effectual removal of indoor ultrafine PM using submicron water droplets," *J. Environ. Manage.*, **296**, 113116 (2021). http://doi.org/10.1016/j.jenvman.2021.113166.

Kim, G., S. Cheng, L. Hong, J.-T. Kim, K. C. Li and L. P. Chamorro, "On the acoustic fountain types and flow induced with focused ultrasound," *J. Fluid Mech.*, **909**, R2 (2021). http://doi.org/10.1017/jfm.2020.1012.

Kim, H., J. Lee and Y.-Y. Won, "A simple derivation of the critical condition for the ultrasonic atomization of polymer solutions," *Ultrason.*, **61**, 20–24 (2015). https://doi.org/10.1016/j.ultras.2015.04.007.

Kirpalani, D. M. and F. Toll, "Revealing the physicochemical mechanism for ultrasonic separation of alcohol–water mixtures," *J. Chem. Phys.*, **117**, 3874–3877 (2002). https://doi.org/10.1063/1.1495849.

Kirpalani, D. M. and K. Suzuki, "Ethanol enrichment from ethanol–water mixtures using high frequency ultrasonic atomization," *Ultrason. Sonochem.*, **18**, 1012–1017 (2011). http://doi.org/10.1016/j.ultsonch.2010.05.013.

Kobara, H., M. Tamiya, A. Wakisaka, T. Fukazu and K. Matsuura, "Relationship between the size of mist droplets and ethanol condensation efficiency at ultrasonic atomization on ethanol–water mixtures," *AIChE J.*, **56**, 810–814 (2010). https://doi.org/10.1002/aic.12008.

Koda, S., T. Kimura, T. Kondo and H. Mitome, "A standard method to calibrate sonochemical efficiency of an individual reaction system," *Ultrason. Sonochem.*, **10**, 149–156 (2003). http://doi.org/10.1016/S1350-4177(03)00084-1.

Koga, Y., K. Nishikawa and P. Westh, "Icebergs" or no "icebergs" in aqueous alcohols?: Composition-dependent mixing schemes," *J. Phys. Chem. A*, **108**, 3873–3877 (2004). https://doi.org/10.1021/jp0312722.

Kojima, Y., Y. Asakura, G. Sugiyama and S. Koda, "The effects of acoustic flow and mechanical flow on the sonochemical efficiency in a rectangular sonochemical reactor," *Ultrason. Sonochem.*, **17**, 978–984 (2010). https://doi.org/10.1016/j.ultsonch.2009.11.020.

Kooij, S., A. Astefanei, G.L. Corthals and D. Bonn, "Size distributions of droplets produced by ultrasonic nebulizers," *Sci. Rep.*, **9**, 6128 (2019). https://doi.org/10.1038/s41598-019-42599-8.

Kudo, T., K. Sekiguchi, K. Sankoda, N. Namiki and S. Nii, "Effect of ultrasonic frequency on size distributions of nanosized mist generated by ultrasonic atomization," *Ultrason. Sonochem.*, **37**, 16–22 (2017). https://doi.org/10.1016/j.ultsonch.2016.12.019.

Kunde, G.B. and B. Sehgal, "Application of sol-gel assisted ultrasound-induced atomization in the mesostructuring of nickel aluminate UF membranes," *Microporous Mesoporous Mater.*, **325**, 111299 (2021). https://doi.org/10.1016/j.micromeso.2021.111299.

Laborde, J.-L., A. Hita., J.-P. Caltagirone and A. Gerard, "Fluid dynamics phenomena induced by power ultrasounds," *Ultrasonic*, **38**, 297–300 (2000). http://doi.org/10.1016/S0041-624X(99)00124-9.

Lang, R.J., "Ultrasonic atomization of liquids," *J. Acoust. Soc. Am.*, **34**, 6–8 (1962). https://doi.org/10.1121/1.1909020.

Lee, D., I. Na and Y. Son, "Effect of liquid recirculation flow on sonochemical oxidation activity in a 28 kHz sonoreactor," *Chemosphere*, **286**, 131780 (2022). http://doi.org/10.1016/j.chemosphere.2021.131780.

Lee, J., K. Yasui, T. Tuziuti, T. Kozuka, A. Towata and Y. Iida, "Spatial distribution enhancement of sonoluminescence activity by altering sonication and solution conditions," *J. Phys. Chem. B*, **112**, 15333–15341 (2008). https://doi.org/10.1021/jp8060224.

Lee, J., M. Ashokkumar, K. Yasui, T. Tuziuti, T. Kozuka, A. Towata and Y. Iida, "Development and optimization of acoustic bubble structures at high frequencies," *Ultrason. Sonochem.*, **18**, 92–98 (2011). https://doi.org/10.1016/j.ultsonch.2010.03.004.

Legay, M., N. Gondrexon, S. Le Person, P. Boldo and A. Bontemps, "Enhancement of heat transfer by ultrasound: Review and recent advances," *Int. J. Chem. Eng.*, **2011**, 670108 (2011). https://doi.org/10.1155/2011/670108.

Lighthill, S.J., "Acoustic streaming," *J. Sound Vib.*, **61**, 391–418 (1978). https://doi.org/10.1016/0022-460X(78)90388-7.

Lim, M., Y. Son and J. Khim, "Frequency effects on the sonochemical degradation of chlorinated compounds," *Ultrason. Sonochem.*, **18**, 460–465 (2011). https://doi.org/10.1016/j.ultsonch.2010.07.021.

Liu, C., Z. Cao, S. He, Z. Sun and W. Chen, "The effects and mechanism of phycocyanin removal from water by high-frequency ultrasound treatment," *Ultrason. Sonochem.*, **41**, 303–309 (2018). https://doi.org/10.1016/j.ultsonch.2017.09.051.

Lohse, D. and S. Hilgenfeldt, "Inert gas accumulation in sonoluminescing bubbles," *J. Chem. Phys.*, **107**, 6989–6997 (1997). http://doi.org/10.1063/1.474939.

Mahamuni, N.N. and Y.G. Adewuyi, "Advanced oxidation processes (AOPs) involving ultrasound for waste water treatment: A review with emphasis on cost estimation," *Ultrason. Sonochem.*, **17**, 990–1003 (2010). https://doi.org/10.1016/j.ultsonch.2009.09.005.

Mai, N.L., Y.-M. Koo and S.H. Ha, "Separation characteristics of hydrophilic ionic liquids from ionic liquids-water solution by ultrasonic atomization," *Ultrason. Sonochem.*, **53**, 187–191 (2019). http://doi.org/10.1016/j.ultsonch.2019.01.004.

Marjanian, M.M., S. Shahhosseini and A. Ansari, "Investigation of the ultrasound assisted CO_2 absorption using different absorbents," *Process Saf. Environ. Prot.*, **149**, 277–288 (2021). https://doi.org/10.1016/j.psep.2020.10.054.

Mason, T.J., "Ultrasonic cleaning: an historical perspective," *Ultrason. Sonochem.*, **29**, 519–523 (2016). https://doi.org/10.1016/j.ultsonch.2015.05.004.

Matsuura, K., M. Kobayashi, M. Hirotsune, M. Sato, H. Sasaki and K. Shimizu, "New separation technique under normal temperature and pressure using an ultrasonic atomization," *Jpn Soc. Chem. Eng. Symp. Ser.*, **46**, 44–49 (1995).

Naidu, H., J. Liu, O. Kahraman and H. Feng, "Ultrasound-assisted nonthermal, nonequilibrium separation of organic molecules from their binary aqueous solutions: Effect of solute properties on separation," *ACS Sustainable Chem. Eng.*, **9**, 16506–16518 (2021). https://doi.org/10.1021/acssuschemeng.1c06793.

Naidu, H., O. Kahraman and H. Feng, "Novel application of ultrasonic atomization in the manufacturing of fine chemical, pharmaceuticals, and medical devices," *Ultrason.*

Sonochem., **86**, 105984 (2022). https://doi.org/10.1016/j.ultsonch.2022.105984.

Nii, S. and N. Oka, "Size-selective separation of submicron particles in suspensions with ultrasonic atomization," *Ultrason. Sonochem.*, **21**, 2032–2036 (2014). http://doi.org/10.1016/j.ultsonch.2014.03.033.

Nii, S., K. Matsuura, T. Fukazu, M. Toki and F. Kawaizumi, "A novel method to separate organic compounds through ultrasonic atomization," *Chem. Eng. Res. Des.*, **84**, 412–415 (2006). http://doi.org/10.1205/cherd05016.

Nishi, N., S. Takahashi, M. Matsumoto, A. Tanaka, K. Muraya, T. Takamuku and T. Yamaguchi, "Hydrogen-bonded cluster formation and hydrophobic solute association in aqueous solutions of ethanol," *J. Phys. Chem.*, **99**, 462–468 (1995). https://doi.org/10.1021/j100001a068.

Ono, Y., K. Sekiguchi, K. Sankoda, S. Nii and N. Namiki, "Improved ultrasonic degradation of hydrophilic and hydrophobic aldehydes in water by combined use of atomization and UV irradiation onto the mist surface," *Ultrason. Sonochem.*, **60**, 104766 (2020). http://doi.org/10.1016/j.ultsonch.2019.104766.

Orisaki, M. and T. Kajishima, "Numerical analysis of water surface rising caused by underwater ultrasonic wave," *Trans. JSME* (in Japanese), **88**, 21-00377 (2022). https://doi.org/10.1299/transjsme.21-00377.

Panão, M., "Ultrasonic atomization: new spray characterization approaches," *Fluids*, **7**, 29 (2022). https://doi.org/10.3390/fluids7010029.

Parvizian, F., M. Rahimi, M. Faryadi and A. A. Alsairafi, "Comparison between mixing in novel high frequency sonoreactor and stirred tank reactor," *Eng. Appl. Comput. Fluid mech.*, **6**, 295–306 (2012). http://doi.org/10.1080/19942060.2012.11015422.

Perra, E., E. Lampsijärvi, G. Barreto, M. Arif, T. Puranen, E. Hæggström, K. P. H. Pritzker and H. J. Nieminen, "Ultrasonic actuation of a fine-needle improves biopsy yield," *Sci. Rep.*, **11**, 8234 (2021). https://doi.org/10.1038/s41598-021-87303-x.

Rahimi, M., N. Moradi, M. Faryadi and S. Safari, "Removal of ammonia by high-frequency (1.7 MHz) combined with TiO_2 photocatalyst under UV radiation," *Desalination Water Treat.*, **57**, 15999–16007 (2015). https://doi.org/10.1080/19443994.2015.1077741.

Rajan, R. and A. B. Pandit, "Correlations to predict droplet size in ultrasonic atomization,"

Ultrason., **39**, 235–255 (2001). https://doi.org/10.1016/S0041-624X(01)00054-3.

Ramisetty, K.A., A.B. Pandit and P.R. Gogate, "Investigations into ultrasound induced atomization," *Ultrason. Sonochem.*, **20**, 254–264 (2013). https://doi.org/10.1016/j.ultsonch.2012.05.001.

Rayleigh, L. (J.W. Strutt), "On the capillary phenomena of jets," *Proc. R. Soc. Lond.*, **29**, 71–97 (1879). https://doi.org/10.1098/rspl.1879.0015.

Rozenberg, L.D. (Ed.), "Physical principles of ultrasonic technology," **2**, 4–88 Springer (1973).

Sajjadi, B., A.A. Abdul Raman and S. Ibrahim, "Influence of ultrasound power on acoustic streaming and micro-bubbles formations in a low frequency sonoreactor: mathematical and 3D computational simulation," *Ultrason. Sonochem.*, **24**, 193–203 (2015). http://doi.org/10.1016/j.ultsonch.2014.11.013.

Sato, M., K. Matsuura and T. Fujii, "Ethanol separation from ethanol–water solution by ultrasonic atomization and its proposed mechanism based on parametric decay instability of capillary wave," *J. Chem. Phys.*, **114**, 2382–2386 (2001). https://doi.org/10.1063/1.1336842.

Sekiguchi, K., C. Saksaki and K. Sakamoto, "Synergistic effects of high-frequency ultrasound on photocatalytic degradation of aldehydes and their intermediates using TiO_2 suspension in water," *Ultrason. Sonochem.*, **18**, 158–163 (2011). https://doi.org/10.1016/j.ultsonch.2010.04.008.

Sekiguchi, K., D. Noshiroya, M. Handa, K. Yamamoto, K. Sakamoto and N. Namiki, "Degradation of organic gases using ultrasonic mist generated from TiO_2 suspension," *Chemosphere*, **81**, 33–38 (2010). https://doi.org/10.1016/j.chemosphere.2010.07.009.

Simon, J.C., O.A. Sapozhnikov, V.A. Khokhlova, L.A. Crum and M.R. Bailey, "Ultrasonic atomization of liquids in drop-chain acoustic fountains," *J. Fluid Mech.*, **766**, 129–146 (2015). https://doi.org/10.1017/jfm.2015.11.

Simon, J.C., O.A. Sapozhnikov, V.A. Khokhlova, Y.-N. Wang, L.A. Crum and M.R. Bailey, "Ultrasonic atomization of tissue and its role in tissue fractionation by high intensity focused ultrasound," *Phys. Med. Biol.*, **57**, 8061–8078 (2012). https://doi.org/10.1088/0031-9155/57/23/8061.

Son, Y., *Advanced oxidation processes using ultrasound technology for water and wastewater treatment*, Handbook of Ultrasonics and Sonochemistry, Springer, Singapore (2016). https://doi.org/10.1007/978-981-287-278-4_53.

Son, Y., J. Cha, M. Lim, M. Ashokkumar and J. Khim, "Comparison of ultrasonic and conventional mechanical soil-washing processes for diesel-contaminated sand," *Ind. Eng. Chem. Res.*, **50**, 2400–2407 (2011). https://doi.org/10.1021/ie1016688.

Son, Y., M. Lim, J. Khim, J. Cha and M. Ashokkumar, "Acoustic emission spectra and sonochemical activity in a 36 kHz sonoreactor," *Ultrason. Sonochem.*, **19**, 16–21 (2012). https://doi.org/10.1016/j.ultsonch.2011.06.001.

Suzuki, A., H. Maruyama, H. Seki, Y. Matsukawa and N. Inoue, "Enrichment of amino acids by ultrasonic atomization," *Ind. Eng. Chem. Res.*, **45**, 830–833 (2006). https://doi.org/10.1021/ie0506771.

Söllner, K., "The mechanism of the formation of fogs by ultrasonic waves," *Trans. Faraday Soc.*, **32**, 1532–1536 (1936). https://doi.org/10.1039/TF9363201532.

Takaya, H., S. Nii, F. Kawaizumi and K. Takahashi, "Enrichment of surfactant from its aqueous solution using ultrasonic atomization," *Ultrason. Sonochem.*, **12**, 483–487 (2005). https://doi.org/10.1016/j.ultsonch.2004.06.012.

Tamidi, A.M., K.K. Lau and S.H. Khalit, "A review of recent development in numerical simulation of ultrasonic-assisted gas-liquid mass transfer process," *Comput. Chem. Eng.*, **155**, 107498 (2021). https://doi.org/10.1016/j.compchemeng.2021.107498.

Tanaka, Y., Y. Mori, K. Matsuura and K. Tsuchiya, "Performance evaluation of ultrasonic atomization process for ethanol separation and recovery," *J. Chem. Eng. Jpn.*, (2011). http://doi.org/10.1252/jcej.11we214.

Tay, W.H., K.K. Lau and A.M. Shariff, "High frequency ultrasonic-assisted CO_2 absorption in a high pressure water batch system," *Ultrason. Sonochem.*, **33**, 190–196 (2016). https://doi.org/10.1016/j.ultsonch.2016.04.004.

Tay, W.H., K.K. Lau and A.M. Shariff, "High frequency ultrasonic-assisted chemical absorption of CO_2 using monoethanolamine (MEA)," *Sep. Purif. Technol.*, **187**, 136–144 (2017). https://doi.org/10.1016/j.seppur.2017.03.068.

Tay, W.H., K.K. Lau and A.M. Shariff, "High performance promoter-free CO_2 absorption us-

ing potassium carbonate solution in an ultrasonic irradiation system," *J. CO_2 Util.*, **21**, 383–394 (2017). https://doi.org/10.1016/j.jcou.2017.08.003.

Tomita, Y., "Jet atomization and cavitation induced by interactions between focused ultrasound and a water surface," *Phys. Fluids*, **26**, 097105 (2014). https://doi.org/10.1063/1.4895902.

Tsuchiya, K., H. Hayashi, K. Fujiwara and K. Matsuura, "Visual analysis of ultrasonic atomization and its associated phenomena," *Earozoru Kenkyu* (*J. Aerosol Res.* in Japanese), **26**, 11–17 (2011). https://doi.org/10.11203/jar.26.11.

Vega, L. P. and G. A. Penuela, "High frequency sonochemical degradation of benzophenone-3 in water," *J. Environ. Eng.*, **144**, 04018058 (2018). https://doi.org/10.1061/(ASCE)EE.1943-7870.0001406.

Vega, L. P., J. Soltan and G. A. Penuela, "Sonochemical degradation of triclosan in water in a multifrequency reactor," *Environ. Sci. Pollut. Res.*, **26**, 4450–4461 (2019). https://doi.org/10.1007/s11356-018-1281-2.

Wakisaka, A. and K. Matsuura, "Microheterogeneity of ethanol–water binary mixtures observed at the cluster level," *J. Mol. Liq.*, **129**, 25–32 (2006). https://doi.org/10.1016/j.molliq.2006.08.010.

Wei, J., J. Gu, J. Guo, W. Li, C. Wang and J. Zhang, "Simultaneous removal of nitrogen oxides and sulfur dioxide using ultrasonically atomized hydrogen peroxide," *Environ. Sci. Pollut. Res.*, **26**, 22351–22361 (2019). https://doi.org/10.1007/s11356-019-05531-1.

Wood, R. J., C. Vévert, J. Lee and M. J. Bussemaker, "Flow effects on phenol degradation and sonoluminescence at different ultrasonic frequencies," *Ultrason. Sonochem.*, **63**, 104892 (2020). https://doi.org/10.1016/j.ultsonch.2019.104892.

Wood, R. J., J. Lee and M. J. Bussemaker, "A parametric review of sonochemistry: Control and augmentation of sonochemical activity in aqueous solutions," *Ultrason. Sonochem.*, **38**, 351–370 (2017). https://doi.org/10.1016/j.ultsonch.2017.03.030.

Wood, R. W. and A. L. Loomis, "The physical and biological effects of high-frequency sound-waves of great intensity," *Lond. Edinb. Dublin Philos. Mag. J. Sci.*, **4**, 417–436 (1927). https://doi.org/10.1080/14786440908564348.

Xu, H., N. C. Eddingsaaas and K. S. Suslick, "Spatial separation of cavitating bubble

populations: The nanodroplet injection model," *J. Am. Chem. Soc.*, **131**, 6060–6061 (2009). https://doi.org/10.1021/ja900457v.

Xu, Z., K. Yasuda and S. Koda, "Numerical simulation of liquid velocity distribution in a sonochemical reactor," *Ultrason. Sonochem.*, **20**, 452–459 (2013). https://doi.org/10.1016/j.ultsonch.2012.04.011.

Xu, Z., K. Yasuda and X. Liu, "Simulation of the formation and characteristics of ultrasonic fountain," *Ultrason. Sonochem.*, **32**, 241–246 (2016). http://doi.org/10.1016/j.ultsonch.2016.03.016.

Yamashita, T. and K. Ando, "Low-intensity ultrasound cavitation and streaming in oxygen-supersaturated water: Role of cavitation bubbles as physical cleaning agents," *Ultrason. Sonochem.*, **52**, 268–279 (2019). https://doi.org/10.1016/j.ultsonch.2018.11.025.

Yano, Y. F., J. Douguchi, A. Kumagai, T. Iijima, Y. Tomida, T. Miyamoto and K. Matsuura, "In situ X-ray diffraction measurements of the capillary fountain jet produced via ultrasonic atomization," *J. Chem. Phys.*, **125**, 174705 (2006). https://doi.org/10.1063/1.2363188.

Yano, Y. F., K. Matsuura, T. Fukazu, F. Abe, A. Wakisaka, H. Kobara, K. Kaneko, A. Kumagai, Y. Katsuya and M. Tanaka, "Small-angle x-ray scattering measurement of a mist of ethanol nanodroplets: An approach to understanding ultrasonic separation of ethanol-water mixtures," *J. Chem. Phys.*, **127**, 031101 (2007). https://doi.org/10.1063/1.2754676.

Yano, Y. F., "Correlation between surface and bulk structures of alcohol–water mixtures," *J. Colloid Interface Sci.*, **284**, 255–259 (2005). https://doi.org/10.1016/j.jcis.2004.09.059.

Yasuda, K., K. Mochida, Y. Asakura and S. Koda, "Separation characteristics of alcohol from aqueous solution by ultrasonic atomization," *Ultrason. Sonochem.*, **21**, 2026–2031 (2014). https://doi.org/10.1016/j.ultsonch.2014.02.011.

Yasuda, K., N. Tanaka, L. Rong, M. Nakamura, L. Li, A. Oda and Y. Kawase, "Effects of carrier gas conditions on concentration of alcohol aqueous solution by ultrasonic atomization," *Jpn. J. Appl. Phys.*, **42**, 2956–2957 (2003). https://doi.org/10.1143/JJAP.42.2956.

Yasuda, K., S. Nakayama and Y. Asakura, "Characteristics of nanoemulsion prepared by tandem acoustic emulsification at a high frequency," *Chem. Eng. J.*, **45**, 734–736 (2012). https://doi.org/10.1252/jcej.12we057.

Yasuda, K., Y. Bando, S. Yamaguchi, M. Nakamura, A. Oda and Y. Kawase, "Analysis of

concentration characteristics in ultrasonic atomization by droplet diameter distribution," *Ultrason. Sonochem.*, **12**, 37–41 (2005). https://doi.org/10.1016/j.ultsonch.2004.05.008.

Yasuda, K., Y. Nohara and Y. Asakura, "Effect of ultrafine bubbles on ethanol enrichment using ultrasonic atomization," *Jpn. J. Appl. Phys.*, **59**, SKKD09 (2020). https://doi.org/10.35848/1347-4065/ab83d9.

Yusof, S.M.M., A.M. Shariff, W.H. Tay, K.K. Lau and N.F.A. Mustafa, "Mass transfer intensification of CO_2 absorption in monoethanolamine using high frequency ultrasonic technology in continuous system," *Int. J. Greenh. Gas Control.*, **102**, 103157 (2020). https://doi.org/10.1016/j.ijggc.2020.103157.

Yusof, S.M.M., K.K. Lau, A.M. Shariff, W.H. Tay, N.F.A. Mustafa and S.S.M. Lock, "Novel continuous ultrasonic contactor system for CO_2 absorption: Parametric and optimization study," *J. Ind. Eng. Chem.*, **79**, 279–287 (2019). https://doi.org/10.1016/j.jiec.2019.06.054.

Zarembo, K., *High-intensity ultrasonic fields*, Plenum Press, New-York (1971).

Zhang, H., X. Zhang, X. Yi, F. He, F. Niu and P. Hao, "Dynamic behaviors of droplets impacting on ultrasonically vibrating surfaces," *Exp. Therm. Fluid Sci.*, **112**, 110019 (2020). https://doi.org/10.1016/j.expthermflusci.2019.110019.

Zhang, Y., S. Yuan and L. Wang, "Investigation of capillary wave, cavitation and droplet diameter distribution during ultrasonic atomization," *Exp. Therm. Fluid Sci.*, **120**, 110219 (2021). https://doi.org/10.1016/j.expthermflusci.2020.110219.

Chapter 3

Time-series data analysis

3.1 Fast Fourier transform

Since the current study aims at obtaining the frequency characteristics—hopefully extracting the dominant frequency(ies) if any—the Fourier-transform analysis will be adopted; in its fast, discrete form of algorithm, fast Fourier transform (FFT), a given time-domain signal $f(t)$ is to be decomposed into a frequency-domain spectrum $F(\omega)$. In the FFT, the corresponding (to the former) sum of discrete elements, $f_{j+1}(t)$ ($j = 0, 1, \dots, N-1$), sampled at equal intervals are processed through a fast, efficient algorithm (MathWorks MATLAB® 2019b) to obtain the corresponding (to the latter) spectrum:

$$F_{k+1}(\omega) = \sum_{j=0}^{N-1} \Psi^{jk} f_{j+1}(t) \tag{3.1}$$

where the term specifying the inner product on the right-hand side is given by the jk-th power of $\Psi = e^{-2\pi i/N}$ (Percival and Walden, 2000), and the left-hand side thus evaluated provides the power spectrum, $|F(\omega)|^2$, which signifies the spectrum intensity at each frequency.

3.2 Discrete wavelet transform

Besides the FFT, the DWT employed as a time–frequency analysis is to be directly applicable to discrete data, expressed as

$$DWf(j,k) = 2^{j/2} \sum_{m} f_m(t) \psi\left(2^j t - k\right) \tag{3.2}$$

Here the given time series as a discrete function, $f_m(t)$, is to be transformed by the discrete wavelet operator, $DW(j,k)$, at dyadic scaling (dilation), 2^{-j}, and shifting (translation), $2^{-j}k$, where a pair of parameters/integers (j,k) specify the ranges of "frequency level" and "local time span," respectively. Such method of sequentially decomposing and analyzing the signal $f(t)$ which consists of $N = 2^M$ data in stages of resolution is called multiresolution analysis (MRA).

Wavelets are a family of functions of invariant shape and zero mean that are localized in both the time and frequency domains. The wavelets family is derived from a single prototype

function, called the *mother wavelet*, by dilating and translating her (as above). Associated with each wavelet, being a band-pass filter, is a low-pass filter, or *scaling function*. The family of discrete dyadic wavelets, $\psi_{j,k}(t) \equiv 2^{j/2}\psi\left(2^j t - k\right)$, thus specified can form a complete orthonormal basis; a usual approach is to select from a library of proven orthonormal basis functions a proper candidate (in this study, Daubechies7 in MATLAB®2019b) so as to best represent the given signal. The wavelet transform—physically interpreted as the signal energy in the region of the time–frequency plane spanned by the selected basis function (Bakshi *et al.*, 1995) and called the *discrete wavelet coefficient*, $d_{j,k}$ [$\equiv DWf(j,k)$]—can be inversely transformed to reconstruct the function $f(t)$ as

$$f(t) \approx \sum_j \sum_k d_{j,k}\psi\left(2^j t - k\right) \equiv \sum_j g_{1-j}(t) \quad (1 \le j \le M) \tag{3.3}$$

That is, the function $f(t)$ is first approximated for the actual numerical scheme by Level/Scale 0 interpolation, $f_0(t)$ [$= g_0(t)$], which is decomposed into Level −1 *scaling* component, $f_{-1}(t)$, and the Level −1 *wavelet* component, $g_{-1}(t)$. Such a decomposition may be repeated until $j = M$ is reached. In principle, if the signal $f(t)$ consists of 2^M data points, it can be decomposed to Level −*M* (Chui, 1992; MathWorks®, 2021). In the present study of MRA, the wavelet decomposition was performed down to Level −9.

References

Bakshi, B.R., H. Zhong, P. Jiang and L.-S. Fan, "Analysis of flow in gas–liquid bubble columns using multi-resolution methods," *Chem. Eng. Res. Des.*, **73**, 608–614 (1995).

Chui, C.K., *An Introduction to Wavelets*, Academic Press, New York, NY (1992). https://www.elsevier.com/books/an-introduction-to-wavelets/chui/978-0-12-174584-4.

MathWorks®, "MATLAB® Wavelet Toolbox™, Discrete Multiresolution Analysis, Practical Introduction to Multiresolution Analysis," Help Center R2021a, Natick, MA (2021). https://jp.mathworks.com/help/wavelet/index.html?lang=en.

Percival, D.B. and A.T. Walden, *Wavelet Methods for Time Series Analysis*, Cambridge University Press, Cambridge, UK (2000). https://doi.org/10.1017/CBO9780511841040. https://www.cambridge.org/core/books/wavelet-methods-for-time-series-analysis/A2018601E6907DE4953EEF7A5D0359E5.

Chapter 4

Periodicity in ultrasonic atomization involving beads-fountain oscillations and mist generation: effects of driving frequency

4.1 Introduction

It has been claimed in the literature (see the specific references below) that selective separation of solute or suspended particles (or surfactants) from a solution can be attained through two possible mechanisms proposed: *capillary-wave* and *cavitation* hypotheses. The former has been supported by, *e.g.*, Qi *et al.* (2008), Collins *et al.* (2012), and Blamey *et al.* (2013); the latter by, *e.g.*, Neppiras and Noltingk (1951), Kojima *et al.* (2010), Ramisetty *et al.* (2013), and Inui *et al.* (2021). Cavitation bubbles, if present, could contribute to such selective separation from a multicomponent system like alcohol–water solutions—in symbiosis with capillary instabilities—associated with UsA (*e.g.*, Kirpalani and Toll, 2002); other supportive references of this *conjunction hypothesis* include Boguslavskii and Eknadiosyants (1969), Rozenberg (1973), Barreras *et al.* (2002), Simon *et al.* (2012, 2015), Tomita (2014), and Zhang *et al.* (2020).

In regard to the DSD of mist generated via UsA, Antonevich (1959) proposed that the size of the emitted droplets depended on the mechanism of their release: capillary-wave instability tended to result in smaller and uniform droplets, while cavitation-bubble collapsing could lead to larger droplets of different sizes on the microscale.

Some visual evidence has been reported in regard to the formation of μm-size droplets—pinched off under parametric decay instability of *capillary waves of microscale* (Sato *et al.*, 2001)—stemming from interfacial oscillations occurring along a perturbed protrusion or a conical fountain/column of solution (Barreras *et al.*, 2002; Tsuchiya *et al.*, 2011). There has been, however, little direct (visual) evidence that links the mist formation to the occurrence/prevalence of *cavitating bubbles within the liquid fountain* (Fujita and Tsuchiya, 2013; Tomita, 2014; Simon *et al.*, 2015). Firstly, the presence of cavitation bubbles under sonication—or "active" bubbles of size usually too small to be individually imaged—have been mostly inferred visu-

ally from a long-time exposure of the sono[chemical] luminescence, *i.e.*, the extent of sonochemical activity signifying the cavitation yield (Lee *et al.*, 2008, 2011; Son *et al.*, 2011). Secondly, a few are available among those cavitation–sonochemistry studies that provide explicit evidence for the simultaneous occurrence of both the cavitation formation and the UsA mist emergence within and out of the liquid fountain, respectively (*e.g.*, Kojima *et al.*, 2010).

Simon *et al.* (2015) conducted high-speed (5,000–30,000-fps) videography using focused transducers, with ultrasound waves of *moderate focal* acoustic intensities [mostly between a few and several hundreds of W/cm^2, or at least 180 W/cm^2—a minimum level for atomization to first appear (though inconsistently) at 20°C (Simon *et al.*, 2012)] in liquid encountering an air interface. For the given ranges of ultrasonic frequencies (2.165 mainly, 1.04 and as low as 0.155 MHz) and liquid sound speeds (1.14–1.90 km/s), they reported, in regard to what they call a drop-chain fountain, that atomization is attained when the acoustic intensity exceeds a liquid-dependent threshold; the drop *diameters* approximately *equal* the ultrasonic *wavelengths*; for (seven) different liquids, the atomization threshold was observed to increase with shear viscosity; upon heating water, the time to commence atomization decreases with increasing temperature; and atomized under overpressure, the static pressure has a negative impact on atomization.

Based on those findings, Simon *et al.* (2015) claimed that bubbles, generated by acoustic cavitation (or possibly boiling), should contribute significantly to atomization from the drop-chain fountain, and overviewed on *one version* of UsA mechanism as follows: For a *focused* ultrasound wave, the *radiation force* from the wave induces a protuberance on the liquid surface. As the protuberance prevails, coherent interactions between the waves *incident on and reflected from* the "pressure-release" interface would result in the generation of numerous cavitation bubbles inside the protuberance. Acoustic emissions out of these cavitation bubbles—as they oscillate and collapse—are in turn added separately or synergistically to the surface ripples caused by capillary-wave instabilities, facilitating the droplets pinch-off in atomization.

Deeper insights—spanning physicochemical as well as hydrodynamic aspects—into the involvement of cavitation in driving the UsA could be gained from the two competing mechanisms proposed for the liquid flow associated with the sonic-generated cavitation bubbles underneath a rather flat free surface—thus in the absence of the UsA liquid fountain: 1) acoustic

radiation pressure/force, as above, in a *traveling*-wave field and 2) acoustic *streaming* in a *standing*-wave field (Lee *et al.*, 2008, 2011; Son *et al.*, 2011).

Lee *et al.* (2011) in particular, examining three different driving frequencies, 168, 448 and 726 kHz, at a fixed input power of 20 W (1.1 W/cm^2), reported the following trends: at the lower frequency, a strong standing-wave filed prevailed homogeneously along the near central, vertical axis above the transducer, especially at early stages of wave propagation; at the intermediate frequency, the attenuation of acoustic pressure amplitude became appreciable with an increase in the driving frequency, leading to the development of a traveling-wave field near the transducer in competition against the standing wave still prevailing near the free surface; at the higher frequency, the attenuation of the acoustic energy became so significant—developing an energy gradient in the direction of the propagating acoustic wave—that the dominant mechanism shifted, with increasing driving frequency, from the radiation pressure caused by the traveling wave to the acoustic streaming.

Kojima *et al.* (2010) investigated, at a fixed driving frequency of 490 kHz for different input powers of 5–50 W ($\cong$ 0.25–2.5 W/cm^2), the patterns of liquid flow and the spatial distribution of acoustic pressure through a laser Doppler velocimetry (LDV) along with a laser-sheet imaging and through sonochemical luminescence, respectively. With increasing input power ($>$ 1.5 W/cm^2), they demonstrated that a liquid fountain formed with appreciable atomization and that sonochemical luminescence was observable not only in the bulk liquid near the liquid surface but also in the fountain while ultrasonic atomization taking place. It is important to note that all these studies above pointed out crucial roles of cavitation dynamics in association with the above two mechanisms, possibly in explaining some aspects of UsA as well.

While the UsA phenomenon as a whole or, in a series as above, is induced by a constant driving (or excitation) frequency—thus being *inherently periodic* in nature, its characterization in terms of frequency analysis has not been reported extensively (*e.g.*, Qi *et al.*, 2008; Tsuchiya *et al.*, 2011). The very first analysis on the periodicity in the dynamics of liquid drops goes back to the late 19th century; it is Rayleigh's (1879) theoretical treatment on small-amplitude oscillations of "free" drops in vacuum (or in the air) that, using spherical harmonic bases, derived—in *linear* approximation—the oscillation frequency of the normal modes; Lamb (1932) extended the analysis to a drop oscillating in an immiscible fluid. In recent years,

acoustic levitation has been extensively employed to investigate drops suspended by an acoustic radiation pressure arising from *nonlinear* effects of intense ultrasound [*e.g.*, Trinh *et al.*, 1982; Trinh and Wang, 1982; Shen *et al.*, 2010; Bouwhuis *et al.*, 2013 (for drops levitated by an airflow); Watanabe *et al.*, 2018].

Trinh *et al.* (1982), in the study of the axisymmetric (small-amplitude shape) oscillations of acoustically levitated liquid drops in an immiscible fluid, measured oscillation frequencies—resonance frequencies of the first few modes—to find them to be in general agreement with theoretical results from linear approximation for low-viscosity liquids (*i.e.*, with negligible viscous damping). Trinh and Wang (1982) further found a trend of increasing oscillation frequency of the axisymmetric mode with increasing extent of an *oblate* distortion, suggesting quantitatively a *soft nonlinearity* in the fundamental resonant-mode frequency as the oscillation amplitude is increased.

Shen *et al.* (2010) reported the actively-modulated parametric excitation of *sectorial* oscillations—a category of non-axisymmetric oscillations—of water drops through acoustic levitation at $\cong 22\,\mathrm{kHz}$. Their important findings include that: the stable sectorial oscillations were observed to span the oscillation modes from the 2nd up to the 7th mode; the initial oblate drop shape is essential to the given excitations; the oscillations, not directly driven by external forces, lead to the frequency that increases with the number of mode but decreases with the equatorial radius; their data—the dependence of the measured oscillation frequency, which will coincide with *half* the modulation frequency, on the drop size as well as the oscillation mode—could be well described using the Rayleigh equation (1879) modified by replacing the *sphere-equivalent* radius with the initial *equatorial* radius of an oblate drop exhibiting mainly horizontal sectorial oscillations.

The periodicity detectable in the liquid-fountain dynamics can be quantified based on the principle of frequency analysis, where time-series data/signals are decomposed into a series of waves with wavelengths and amplitudes individually specified. If the aim of analysis were just to identify the characteristic/dominant frequencies, the Fourier-transform analysis in terms of power spectrum density would be adequate. The Fourier transform—or its fast, discrete form of algorithm (fast Fourier transform: FFT)—and its inverse establish a one-to-one relationship between the time domain, function $f(t)$, and the frequency domain, spectrum $F(\omega)$.

It can be viewed as the decomposition of $f(t)$ into a sum of frequency components, the coefficients of which are given by the inner product of $f(t)$ and $\exp(-i\omega t)$. The spectrum $F(\omega)$ dictates the overall strength/intensity with which each frequency ω is contained in $f(t)$. The Fourier transform, however, does not show how the frequencies vary with time in $f(t)$.

If, on the other hand, the time-series data were to be analyzed to extract essential quantitative features *hidden* in the signals both in *time and frequency* domains and directly linked to the fountain dynamics associated with apparently *ad-hoc* (thus time-dependent) droplet-bursting events, it would be a time–frequency analysis (discrete wavelet transform: DWT) that plays a role (*e.g.*, Chui, 1992; Daubechies, 1992; Tsuchiya *et al.*, 2004; Liu and Wang, 2019). The wavelet-transform analysis, being able to extract more detailed information, especially time-dependent (such as shift in frequency with time) characteristics of the signals, could provide better physical interpretation of the UsA phenomenon, thus helpful in detecting possible correlations between the rather regularly oscillating fountain surface and the occasionally "triggered" droplets bursting.

Several aspects of the UsA in its fundamental nature have been described thus far: the DSD of emerging mist; the selective separation/concentration of solute (and the alike) into the mist with its extent and mechanism(s); the structure and dynamics of the (general) liquid fountain observed visually; more extensive visual elucidation of the beads-structured fountain associated with internal cavity and/or (external) droplets bursting; and the periodic nature or some dominant frequencies of the fountain-beads (or ideal cases of isolated-drops) oscillations. Among these, it is the present study's intent to focus on quantitatively elucidating the effects of the UsA driving frequency on the structure [including characteristic dimension(s)] and dynamics [*viz.*, characteristic frequency(ies)] of a chain-of-beads fountain realized under lower input power intensity.

To this end, high-speed, high-resolution visualization is utilized to identify the surface dynamics of individual fountain-beads and possible realization of the droplets bursting; both the frequency (FFT) and time–frequency (DWT) analyses are employed to evaluate their periodic characteristics; and some theoretical consideration is made to obtain simple—hopefully predictive—relationships towards providing the ranges of characteristic dimension and frequency as functions of the driving frequency.

4.2 Experimental

Figure 4.1 shows a schematic diagram of the experimental system for ultrasonic atomization. A high-frequency ultrasonic transducer (KAIJO QT-011: 1.0, 2.0 and 3.0 MHz) was set on the bottom of a square vessel; the dimensions of the vessel were 200×200×185 (height) mm. The input power applied to the transducer ranged 4–14 W. A Teflon® nozzle with a conical hollow structure (inner diameter of 2 mm at the top) was installed—to help stabilize the liquid-column formation and behavior—directly above the transducer's oscillating disk, a circular element of 20.0 mm in diameter (with an effective oscillating diameter of 16 mm) and 7.5 mm above the bottom. The input power density then ranged 2–7 W/cm^2, which will be exclusively used below as an operating parameter.

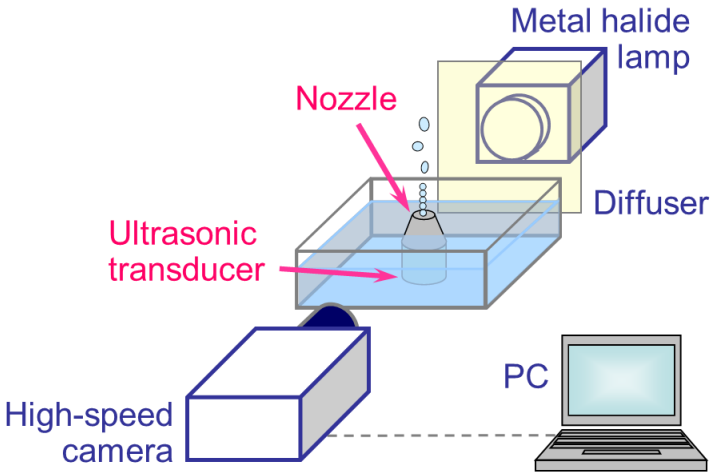

Figure 4.1 Schematic diagram of the experimental system for visual observation of liquid fountain.

The distance from the center of the oscillating disk to the free surface of the solution (effective liquid depth) was 20 mm. The liquid used was an aqueous ethanol solution with initial concentration of 50 wt% (28 mol%), temperature of which was set, before each run, to 25°C in a constant temperature bath. During the UsA over 10 seconds of operation at most, the bulk ethanol concentration is presumed not to vary, thus the liquid properties kept invariant.

4.2.1 High-speed visualization

High-speed imaging was made via a digital camera (Photron FASTCAM MINI AX100) attached with a macro-lens (Nikon Micro-Nikkor 105 mm f/2.8) to observe the dynamics of

liquid fountain and the associated phenomena, especially in detecting the ever-changing outline of the fountain surface and the onset position of droplet bursting. Each specific projection was captured—at a frame rate of 20,000 fps (with a resolution of at least 256×512 pixels) and an exposure time of 46.88 μs (inter-frame time of 3.12 μs)—using a metal halide lamp (Lighterace MID-25FC) as a light source. The imaging was started 5 s after the transducer was powered and a 0.5-s period of data were recorded. A sheet of light diffuser was installed between the liquid fountain and the lamp, thus reducing the non-uniformity of backlighting.

4.2.2 Image processing

Figure 4.2 shows a sequence of the procedures for image processing and data acquisition. An image analysis software (DITECT Dipp Macro) was used to binarize original images of the liquid column in the air; the threshold for the binarization was set at the brightness level of the "shadow" in the very vicinity of the gas–liquid interface. Filling in blank(s) then extracted the interface boundary/outline, confined by thinning it down to 1 pixel; the centerline of the liquid column was extracted as well. A video analysis software (KEYENCE Movie Editor) was used to determine the shape of an ellipse representing each bead in contact along the liquid column; the lowest two beads above the bottom of the liquid column were regarded stable and equivalent (or representative) spherical diameters of the two were measured in each image; this "vertical" apparent/effective chord length is determined to be the characteristic size of the fountain beads—an average over 60 pieces of the relevant images (30 frames of images with two beads each) obtained under each experimental condition.

4.3 Results and Discussion

The characteristics of liquid fountain and its associated mist observed under the present experimental conditions are described and discussed in both static/time-averaged and dynamic natures, with specific driving frequencies of 1.0, 2.0 and 3.0 MHz (as well as auxiliary ones of 0.43, 0.80, 1.6 and 2.4 MHz) over the range of input power density, 2–7 W/cm^2—applied to the UsA transducer.

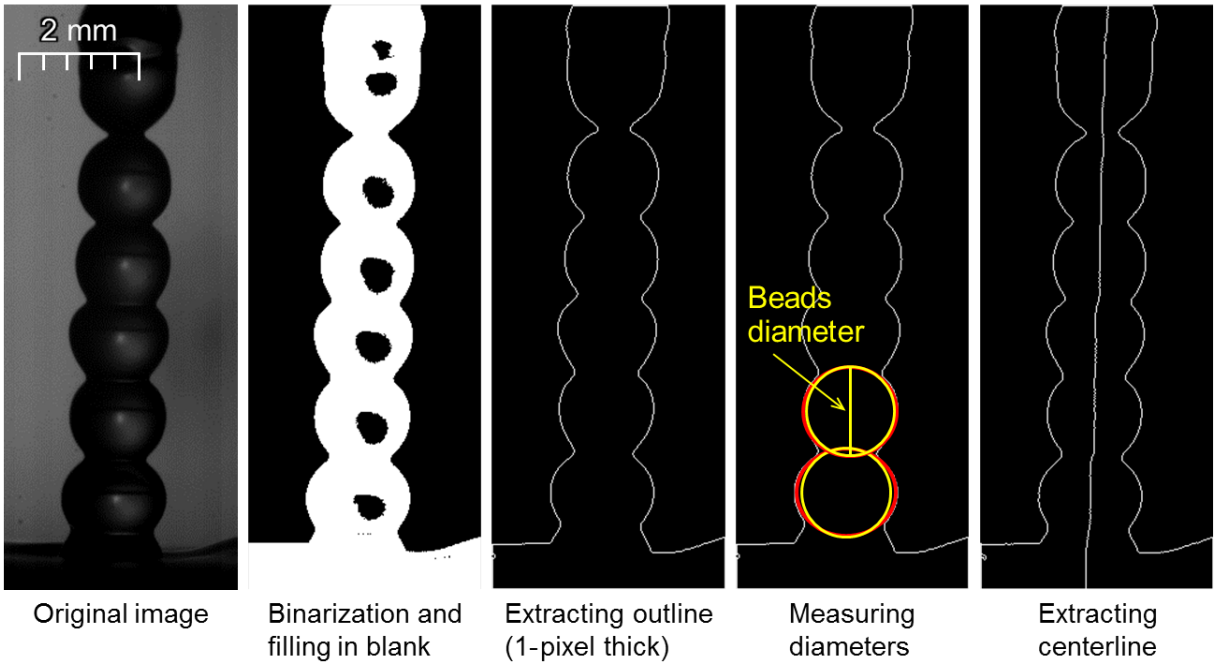

Figure 4.2 Sequence of image processing involving binarization for determining individual beads diameter.

As demonstrated in **Fig. 4.3** for the case of the highest driving frequency examined, 3.0 MHz, a chain-of-beads fountain (Fujita and Tsuchiya, 2013) is found to be attainable with limited stability in the formation of such a steady beads structure of liquid column—being confined to a range of 3–6 W/cm^2 (with the specific transducer used): below this range, a series of beads emanating from the so-called "Foundation Region" right above the nozzle (Tsuchiya *et al.*, 2011) are no longer stable; above the range, the beads structure will be disturbed to an extent that it may not be recognized. It is to be noted here that, while the lowest input power density of the said range, 3 W/cm^2, could lead to the beads fountain, it may not maintain the characteristic aligning stability along the vertical direction of ultrasonic wave propagation from the transducer. In the following, the characterization of the beads fountain as well as the associated mist is prescribed mainly in terms of the three representative driving frequencies in the confined range of applied power density (4, 5 or 6 W/cm^2 exclusively).

4.3.1 Phase-averaged size specificity of beads fountain

Figure 4.4 shows three series of images of the beads fountain obtained at different driving frequencies when the applied power density is 6 W/cm^2. With an increase in the driving

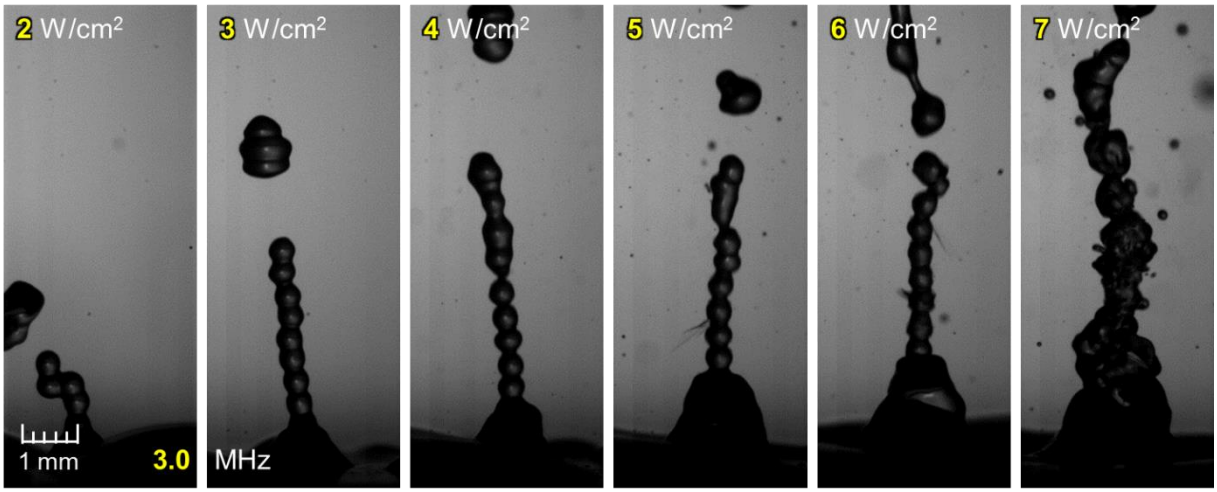

Figure 4.3 Images of liquid fountain obtained at different input power densities for driving frequency of 3.0 MHz.

frequency, the size of beads will decrease drastically. Some specific features of the beads fountain are noted when comparing them between the frequencies: When the frequency is 1.0 MHz, the fountain is mostly characterized by its surface oscillations occurring, for some of the beads, due to the excitation of either local protrusions or capillary waves on the otherwise smooth surface; still, the beads chain basically consists of spheres or ellipsoids.

At 2.0 and 3.0 MHz, in addition to such surface oscillations of the bead, which will be noticeably enhanced—in the form of bead shape itself, two features are clearly detected, *viz.*, the bursting of (rather large) droplets concurring with such shape fluctuations and the noted extent of the Foundation Region. The latter feature is particularly obvious at 3.0 MHz, which implies that the extensive formation of the Foundation Region may promote the droplets bursting. This speculation is supported by Simon *et al.* (2012), who reported that once the "mound" (the same as the Foundation Region) was formed, more significant atomization ensued. From a different perspective, the growth rate of the beads fountain (in relation to ultrasonic surface-wave propagation rate) was measured to be 102, 112 and 183 mm/s; the fountain growth rate at 3.0 MHz was much (by roughly three quarters) faster than those at 1.0 and 2.0 MHz. It is thus believed that there should be some significant differences in the bulk and surface dynamics along the liquid fountain caused by those in the UsA driving frequency, which need to be clarified in the future work.

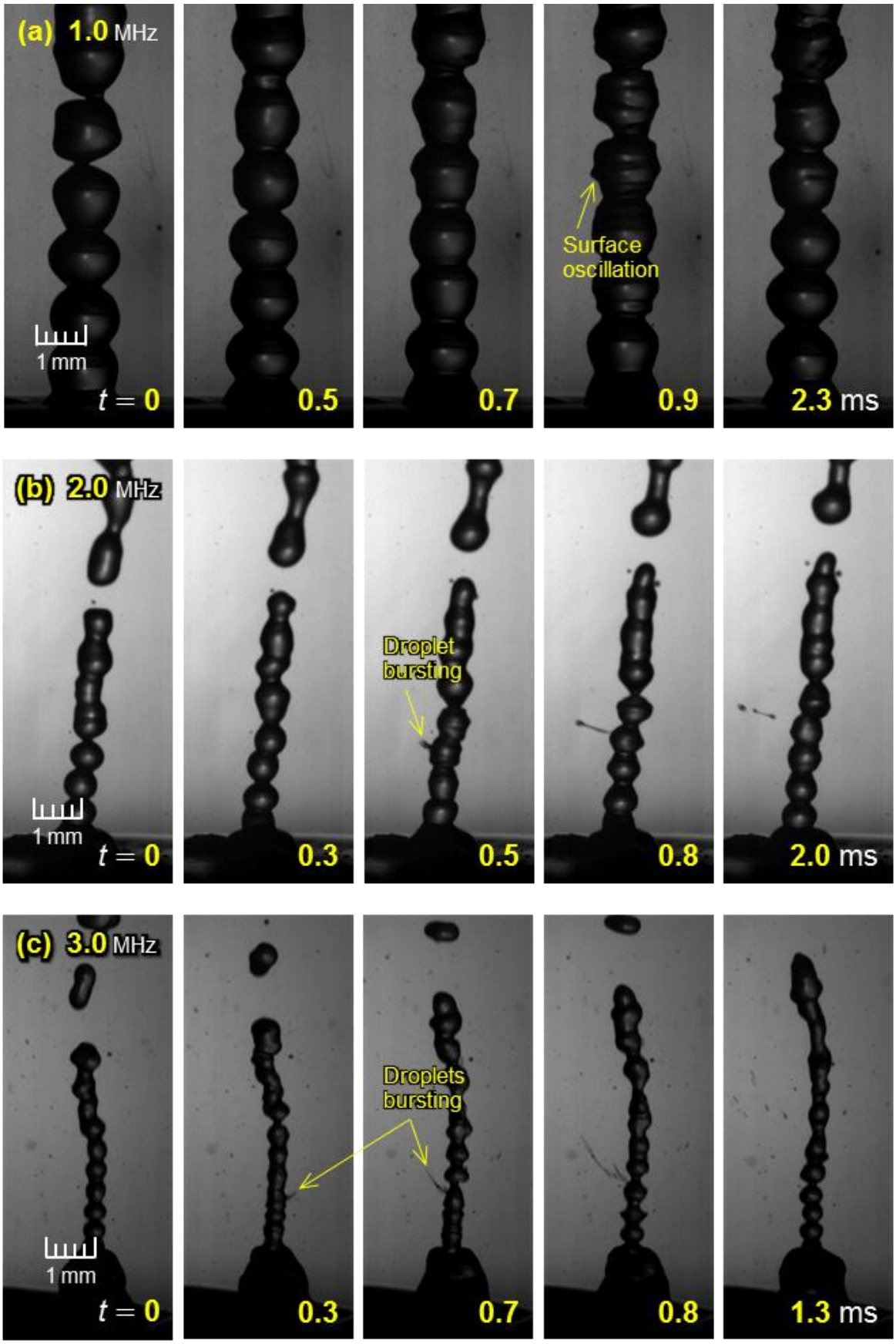

Figure 4.4 Time sequences of beads fountain at driving frequencies of (a) 1.0, (b) 2.0 and (c) 3.0 MHz for input power density of 6 W/cm^2.

As a general feature, the sizes of chain-beads constituting the liquid fountain are found to be nearly uniform (except for ones associated with the droplet bursting) at each given driving frequency (see Fig. 4.4), while the fountain tends to repeatedly reproduce longitudinal/transverse shape stretching (vertically cross-sectioned ellipticity) of each bead. Once the contour of each ellipse is determined (see Section 4.2.2), an apparent diameter of each bead in the *direction of the ultrasonic wave* is estimated as a characteristic length *associated with the wave propagation*. This length (*i.e.*, *vertical* chord length) should then be a proper/effective measure of *wave-inherent*—if indeed it applies so—bead diameter approximated by an imaginary circle completing the outline of "spherical" bead (see Fig. 4.2), which can also signify on average the liquid-column diameter.

Table 4.1 lists the measurement results for such "effective" diameter of chain-beads at each of the input power densities of 4, 5 and 6 W/cm^2; the diameters of 60 pieces of beads selected properly (see above) were measured under each condition, for the ultrasonic frequencies of 1.0, 2.0 and 3.0 MHz, to provide three representative average diameters of 1.44, 0.68 and 0.45 mm, respectively. In order to reduce possible human-associated errors in the measurement, three identical sets of measurements were conducted by three persons, which essentially provide consistent results for both the averages and standard deviations. It can be suggested that this characteristic—*wave-inherent*—diameter is rather independent of the applied power density and that—more importantly—it *indeed* will almost coincide with *half* the values of the wavelength of ultrasound being excited by the 1.0-, 2.0- and 3.0-MHz driving frequencies; the pertaining wavelengths are estimated to be 2.94, 1.47 and 0.98 mm, respectively, where the sound speed of 1,470 m/s in 50-wt% ethanol aqueous solution at 25°C (Mijaković *et al.*, 2011) is employed.

Table 4.1 Beads diameters for different input powers and ultrasonic frequencies

Input power (W/cm^2)	4	5	6
1.0 MHz	1452±139 μm	1436±106 μm	1432±109 μm
2.0	675±47	679±76	677±46
3.0	451±49	438±39	453±45

Thus obtained results are consistent with those reported by Simon *et al.* (2015). While they used a different type of (focused) ultrasonic transducer with frequencies of 1.04 and mostly 2.165 MHz and applied input power densities about 30 times or greater than the range examined in this study, the resulting fountain was of almost the same range of diameters as the present estimates. In their focused-transducer configuration using water as the liquid phase, a doublet of beads—unlike our chain-of-beads fountain—were formed whose values of diameter were reported to be 1.50 and 0.62 mm, respectively, at the above driving frequencies. It could then be assured that the beads-fountain diameter is to be independent of the type of high-frequency transducer as well as the applied power density but will depend on the driving frequency along with the sound speed of the ultrasonic wave.

In addition to the three frequencies examined (and discussed so far) in the present study, *i.e.*, 1.0, 2.0 and 3.0 MHz, auxiliary tests are made applying lower (< 1 MHz) ultrasonic frequencies of 430 and 800 kHz as well as intermediate ones, 1.6 and 2.4 MHz; note that the former three are generated using the same types of transducer elements from KAIJO described in Section 4.2, while the last one comes from the transducer (Honda Electronics HM-2412) used in our previous studies (Fujita and Tsuchiya, 2013; Satomi *et al.*, 2019).

Figure 4.5 shows the average diameter of the fountain beads obtained under each specific condition tested, plotted as a function of the driving frequency. All the data points, including the auxiliary ones—but excluding the data at the lowest two frequencies, for the average diameters or the characteristic bead diameters (d_{bead}) of 0.85 and 0.60 mm, respectively, at 1.6 and 2.4 MHz as well as the values given in Table 4.1 tend to follow the physical principle, *viz.*,

$$2d_{bead} \cong \lambda_{wave} = v_{wave}/f_{wave} \tag{4.1}$$

where λ_{wave} is the wavelength, v_{wave} the speed, and f_{wave} the frequency of the ultrasound excited by the driving frequency. Here it should be noted that the frequency of the ultrasonic wave f_{wave} realized to prevail—once sufficient instabilities are set in to induce the observed liquid-column fluctuations—will be *half the ultrasonic excitation frequency* f_{ex} (Lang, 1962; Qi *et al.*, 2008; Tsuchiya *et al.*, 2011; Kooij *et al.*, 2019), which is assumed to be identical to the driving frequency:

$$f_{wave} = f_{ex}/2 \tag{4.2}$$

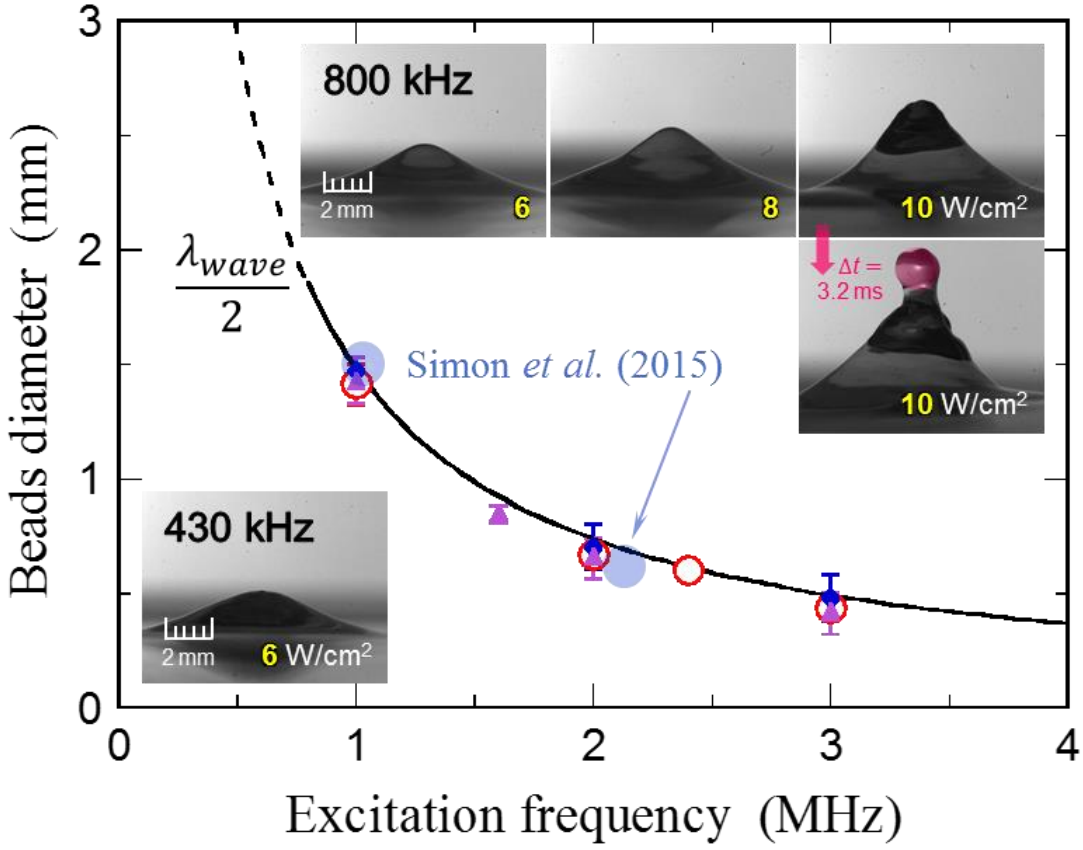

Figure 4.5 Decreasing trend in beads diameter with increasing UsA-driving, or ultrasound-excitation, frequency, predicted by that in ultrasound wavelength (experimental data represented by three different symbols to signify three identical sets of measurements, conducted by three persons, which essentially provide consistent results for both the averages and standard deviations, thus with possible human-associated errors minimized in the measurement).

It would be of a significant physical implication then to infer that the *contour* of a chain of beads in contact could be represented by a (not space-fixed but) "time-traced" traveling wave axially reflected on both sides, resembling a "virtual" *standing wave* form of nonlinear sinusoidal nature, as can be seen in Fig. 4.4 in the steady formation region (*i.e.*, the lower part of each image), with its wavelength approximated by the above estimate.

As the driving/excitation frequency f_{ex} is decreased, the characteristic bead diameter d_{bead} increases in line with the hyperbolic variation, depicted by the solid curve in Fig. 4.5, in the ultrasound wavelength λ_{wave} (for a given liquid, thus fixed v_{wave}). This trend represented by Eq. (4.1) with Eq. (4.2) cannot be judged, however, to be realized for the lower f_{ex} of 800 as well as 430 kHz, as no appreciable liquid-fountain formation was observed—above the stabilizing nozzle—under the present experimental conditions (see the inset of Fig. 4.5 without

the nozzle equipped). It is only noted here that the lower 0.43-MHz auxiliary case resulted in merely a gently-sloping swell or mound on otherwise horizontal liquid surface even with increasing input power, while the higher 0.80-MHz case exhibited a sharper protrusion with occasional precursory beads-like protuberance on top of it.

In the latter case, the height of protrusion increased with the input power; at the highest tested in this study (10 W/cm^2), the precursory structure—projected as a circle—was evaluated to have an average diameter of 1.88 mm for 30 different occasions (cf. the pink-shaded in the figure inset). Such two cases of unrealized UsA would stem partly from possible failure in attaining the threshold level for the *high directivity*—or more probably, partly from the two mechanisms described in Section 4.1—acoustic *radiation pressure* and/or acoustic *streaming*—of soundwave induced by applying ultrasound of *high frequency*.

Furthermore, even if the beads fountain could have been formed, the characteristic bead diameter d_{bead} may exceed (or at least comparable to) the capillary length (l_c):

$$l_c = \sqrt{\sigma/\rho_l g} \tag{4.3}$$

where σ and ρ_l are the surface tension and density of the liquid, respectively, and g the gravitational acceleration. When this condition ($d_{bead} > l_c$) meets (see the dashed part in Fig. 4.5), the gravitational wave would dominate over the surface-tension/capillary wave. For the present 50-wt% ethanol aqueous solution at 25°C, $l_c = 1.80$ mm with the density and surface tension of 902 kg/m^3 and 28.8 mN/m used (Khattab *et al.*, 2012). The characteristic bead diameter, on the other hand, would be estimated—if exists—to be $d_{bead} \cong \lambda_{wave}/2 = \left(\frac{1}{2}\right) 1{,}470/(800\times10^3/2) = 1.84$ mm, thus $d_{bead} > l_c$, for f_{ex} of 800 kHz. It could then be claimed that realizing UsA or the beads fountain requires a minimum driving frequency of at least 0.8 MHz.

4.3.2 Time-dependent characteristics of beads fountain

When the input power density and/or driving frequency are below given thresholds (but within the present confined ranges), the beads fountain forms, as indicated in the previous section, with almost no atomization detected—but with moderate surface oscillations. As either the input power density or the driving frequency, or both, are raised, droplets bursting and/or mist spreading would arise from the beads fountain. As shown in **Fig. 4.6**(a) at moder-

ate 2.0 MHz, a stable beads fountain is formed—cyclically—at an arbitrarily defined clock time $t = 0$, ~5 s after the onset of ultrasonic irradiation. Subsequently, (b) bursting of a rather large droplet is detected across the surface of a fountain bead, along with the shape and surface state of the bead being altered. These multitude of phenomena are then followed by (c) thrusted spread of clouds of tiny droplets, or mist. While the mist may not be observed (limited by the camera resolution) every time it is generated, it tends to follow the droplets bursting. Such a series of time-sequent result obtained at the highest input power density of the range, 6 W/cm^2, indicates that the droplet bursting could trigger the mist emergence. This speculation is partly supported by Simon *et al.* (2015), who captured droplet bursting before atomization as well.

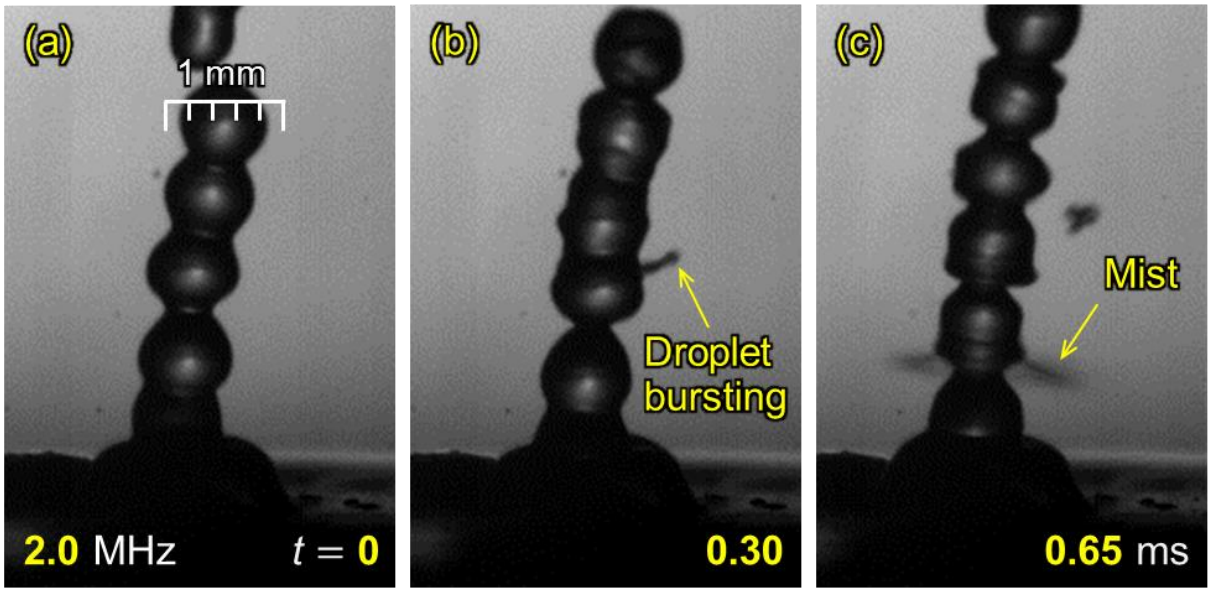

Figure 4.6 High-speed imaging of beads fountain with bursting droplet(s) and mist, captured at 2.0 MHz and 6 W/cm^2: (a) stable chain-of-beads fountain, (b) droplet bursting from a fountain bead, and (c) succeeding mist spreading and bead deformation.

The extent of surface oscillations along the beads fountain—or the deformation of each bead itself—signifies the above-stated disturbances observed in the absence and presence of the mist spreading as well as the droplets bursting; such extent is to be quantified for each driving frequency. To extract the extent or the amplitude of bead-surface disturbances or wavy dynamics exclusively, the lateral oscillations (or the left–right swing) of the beads fountain as a whole need to be removed. As depicted in **Fig. 4.7**(a), both the contour of the fountain sur-

face and the fountain centerline are extracted based on the image processing described in Section 4.2.2. The horizontal distance from thus-determined central axis to the surface outline—the *net* amplitude of oscillations—is measured at three different vertical locations (Positions 1, 2 and 3) each fixed; these three positions are selected—above the Foundation Region—to be approximately multiples of the average bead diameter.

Figure 4.7(b) shows the time variations, for 1.0, 2.0 and 3.0 MHz at 6 W/cm^2, of each lateral location thus specified at a given axial position, while Fig. 4.7(c) and (d) provides the outcome of FFT analysis (see Chapter 3) of beads-fountain oscillations for Positions 1 and 3, respectively. At 1.0 MHz, a "semicircular waveform" is "reproduced" in time series on Position 1, whose outline in time reflects the spatial sequence—in the vertical direction—of the fountain-beads shape. The waveform of nearly the same amplitude is obtained on Position 3 as well; the fountain is relatively stable and of almost no droplets bursting. At 2.0 or 3.0 MHz, a waveform with still stable outline is obtained on Position 1, but non-uniformity of the amplitude becomes appreciable on Positions 2 and 3.

Based on the FFT analysis [Fig. 4.7(c) and (d)], the beads-fountain oscillations are found to be characterized on Position 1 by essentially a unique dominant frequency for each of the driving frequencies, as provided in **Table 4.2**, indicating that the waveform obtained on Position 1 should be the surface wave of the beads fountain itself. As given, the dominant frequency in the surface fluctuations of the beads fountain does increase drastically with an increase in the driving frequency. On Position 3, multitude of peaks are detected at 2.0 and 3.0 MHz. It is to be noted that the droplets bursting will occur mostly out of Position 3 (the uppermost position examined) along the chain, which in turn contributes to disturbing the periodicity of beads-surface motion. Over this frequency band, factors strongly related to the droplets bursting are inevitably concealed.

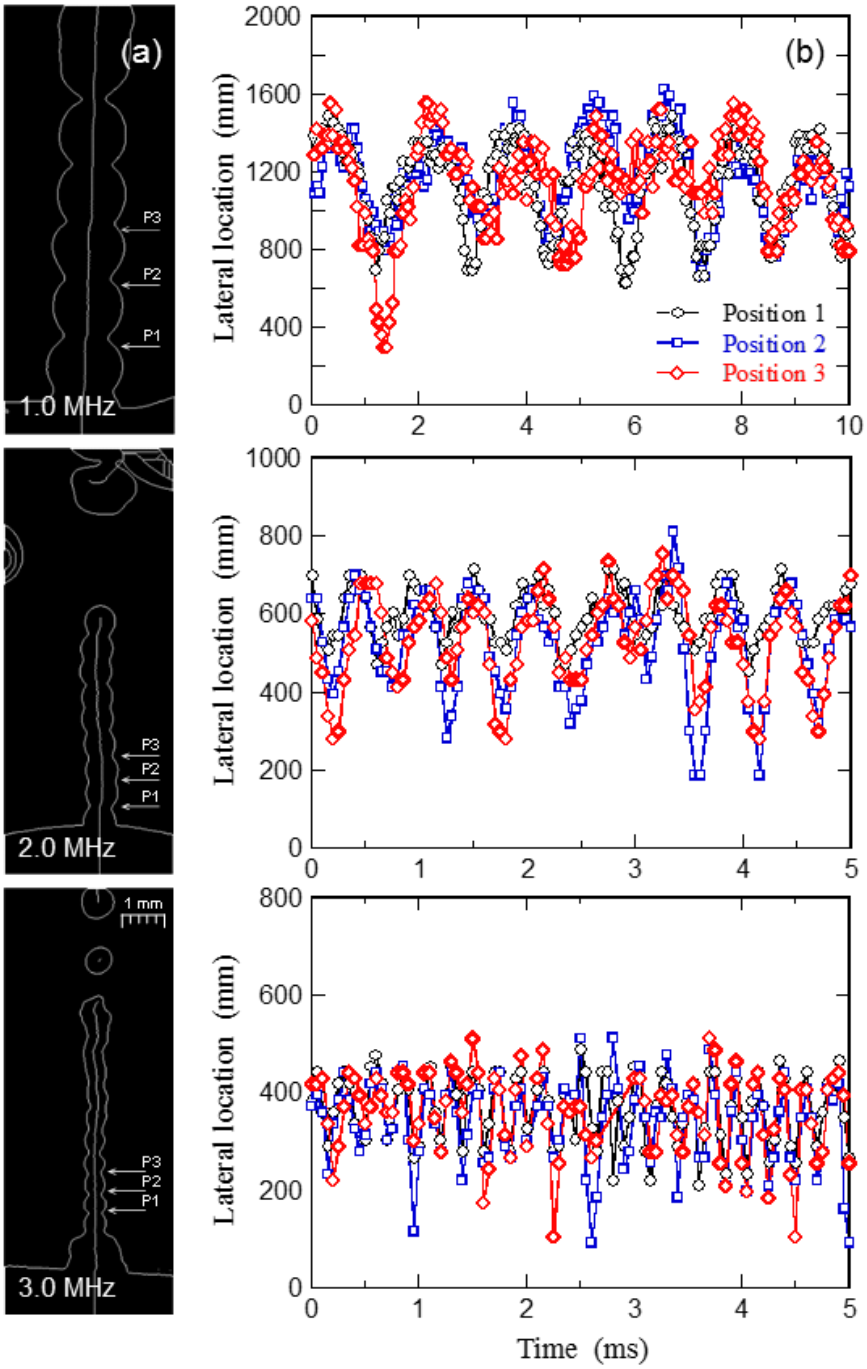

Figure 4.7 (a) Net lateral locations—the distances from centerline to surface outline—to be evaluated at three different, fixed vertical locations, or positions denoted as P1, P2 and P3, for driving frequencies of 1.0, 2.0 and 3.0 MHz: values of (P1, P2, P3) = (1.45, 2.9, 4.35), (0.7, 1.4, 2.1) and (0.45, 0.9, 1.35) mm, respectively, above Foundation Region; (b) Time variations in each lateral location thus specified at given axial positions (6 W/cm^2); Outcome of FFT analysis of beads-fountain oscillations at (c) Position 1 and (d) Position 3.

Figure 4.7(c),(d)

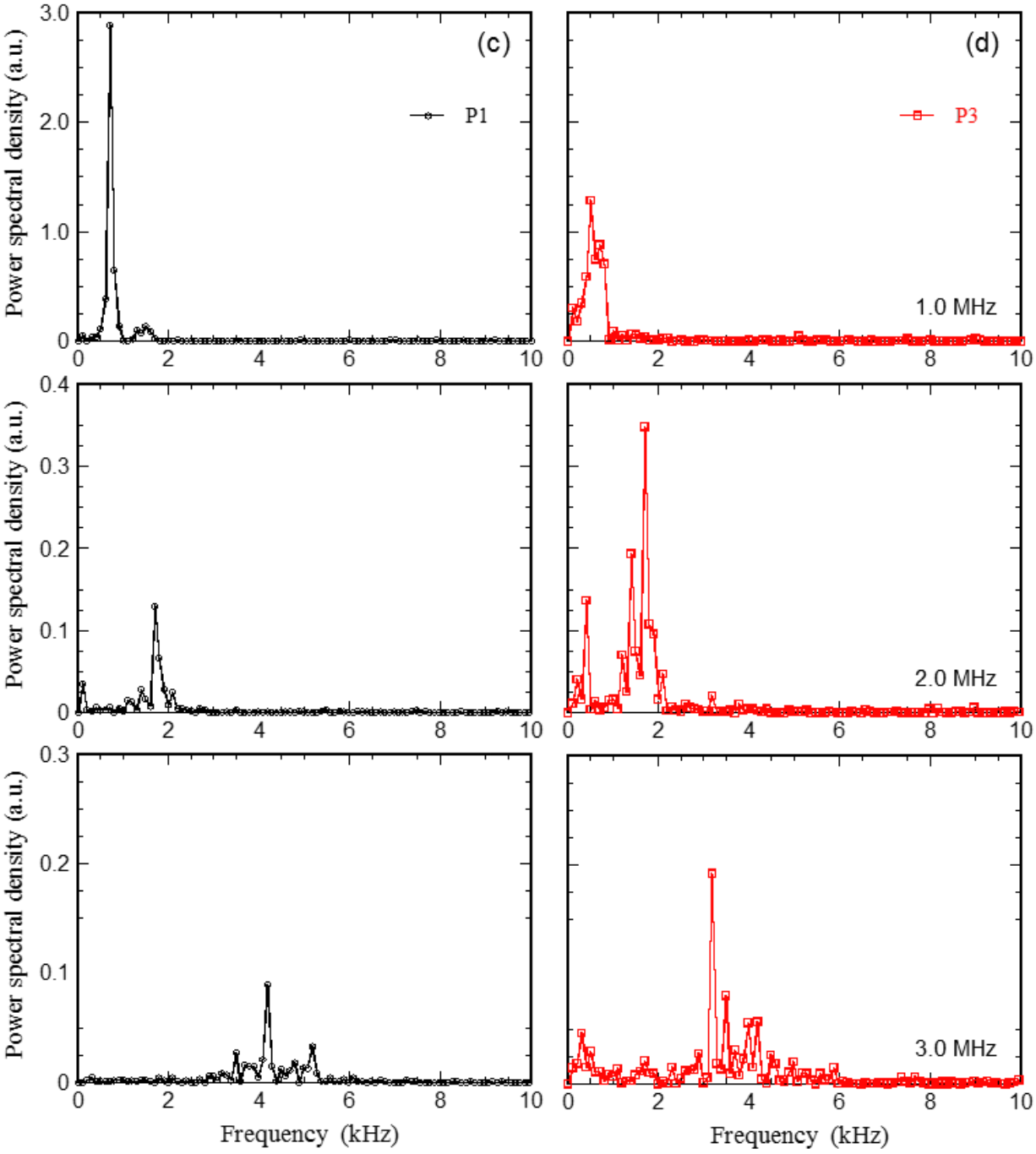

Table 4.2 Comparison of experimental data with predicted values for dominant frequency

f_{ex} (MHz)	Exp (FFT) Main freq. (kHz)	Exp (DWT) Main freq. (kHz)	Exp (DWT) Bursting freq. (kHz)	Pred [Eq. (7)] f_2 (kHz)	f_4 (kHz)	f_6 (kHz)
1.0	0.70	—	—	0.13	0.38	0.70
2.0	1.70	1.26—2.52	0.32—1.26	0.36	1.08	1.98
3.0	4.20	2.52—5.05	0.63—2.52	0.66	1.99	3.63

4.3.3 Simple model-evaluated periodicity of beads fountain

In Section 4.3.1, the UsA fountain under the present confined ranges of operation is described to consist of stable, nearly spherical beads, which could be (and have been) regarded as individual liquid drops. Studies on the free oscillations of liquid drops were pioneered by Rayleigh (1879), followed by Kelvin (1890). In an idealized situation of a self-resonating spherical liquid drop, which originates from (as a constituent of) a liquid jet being destabilized and performs shape oscillations, Rayleigh (1879) derived theoretically—without damping—the resonant angular frequencies ω_n of the drop to be

$$\omega_n^2 = (2\pi f_n)^2 = n(n-1)(n+2)\frac{\sigma}{\rho_l r_e^3} \tag{4.4}$$

where r_e is the equivalent (spherical) radius of the bead/drop. With this size of drop as well as the liquid properties σ and ρ_l specified, the resonance frequencies f_n can be estimated by assigning n, the mode of shape oscillations—the order corresponding to the representative shape of an oscillating drop, whose (vertical in our case) cross section is of, *e.g.*, ellipse: $n = 2$, triangle: $n = 3$, diamond: $n = 4$, pentagon: $n = 5$, and hexagon: $n = 6$ (Shen *et al.*, 2010; Bouwhuis *et al.*, 2013; Watanabe *et al.*, 2018).

As inferred from the previous sections, the surface motion of the beads fountain observed in this study is of a resonant nature—*i.e.*, occurring at or (if not completely undamped) near the natural frequency of the beads system—dominated by ultrasound-excited surface waves; the above formula can then be applied to this "beads" system. If applied, the formula would be expressed in terms of an apparent dimensionless number, the resonance Strouhal numbers (Sr_n) based on the resonance frequencies f_n and the drop diameter, which can be replaced by the individual bead diameter ($2r_e \cong d_{bead}$) in this study, as

$$\pi\, Sr_n = \sqrt{n(n-1)(n+2)} \equiv F(n) \tag{4.5}$$

with the Strouhal number defined by

$$Sr_n = \frac{f_n\, d_{bead}}{\sqrt{2\sigma/\rho_l d_{bead}}} = \frac{f_n\, l_c}{\sqrt{2\sigma/\rho_l l_c}}\left(\frac{d_{bead}}{l_c}\right)^{\frac{3}{2}} \tag{4.6}$$

It is noted in this equation that the denominator signifies the propagation velocity of a capillary waveform (Fan and Tsuchiya, 1990) or the so-called capillary–inertial velocity (Liu *et al.*, 2014), and in this regard the capillary length l_c defined by Eq. (4.3) is explicitly introduced into the expression, along with the reduced bead diameter. Note also that this dimensionless

frequency takes $Sr_n = 0.90$, 2.70 and 4.93 for the mode $n = 2$, 4 and 6, respectively.

Typical patterns of beads deformation observed in the present experiments (at 6 W/cm^2) are illustrated in **Fig. 4.8**, which signify the time-course shape change of beads fountain prior to atomization being triggered ($t < 0.2$ ms) with *possible* oscillation modes indicated in the figure. Initially, the beads tend to oscillate as if an ellipsoid of prolate-and-oblate oscillation mode ($n = 2$), as shown in Fig. 4.8(a) and (b); then the beads appear to shift to a diamond-shape mode ($n = 4$), with the radius of curvature on both sides of the beads getting smaller [Fig. 4.8(c)], followed by the number of bead's "horns" (to be called here) changing from two to four, transitioning to a hexagonal mode ($n = 6$) [Fig. 4.8(d)]; and eventually, a star shape would give rise to droplets bursting and/or mist spreading [Fig. 4.8(e)]. The occurrence of oscillation mode $n = 6$ of the beads was confirmed several times before/after the droplets bursting or mist spreading, which is noted to be observed out of a bead (at a time) along the fountain rather than one at its top (cf. Tomita, 2014; Simon *et al.*, 2015).

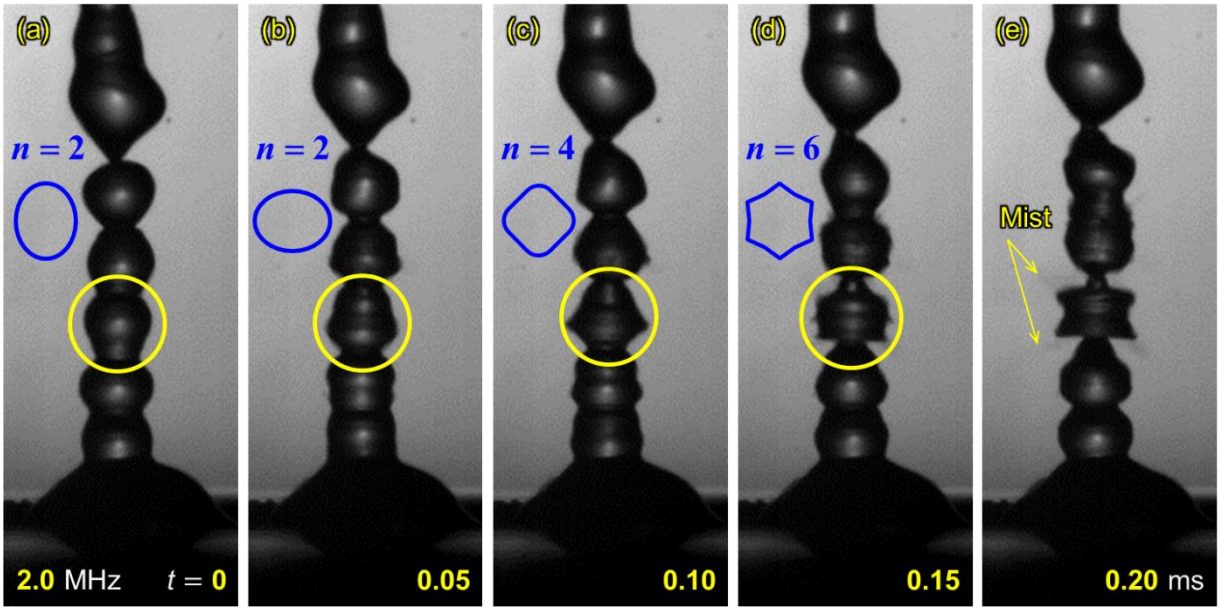

Figure 4.8 Typical patterns of beads deformation, signifying time-course shape change of beads fountain before atomization being triggered ($t < 0.2$ ms) with presumed oscillation modes indicated (2.0 MHz, 6 W/cm^2).

While the mode $n = 6$ of each constituting bead has been frequently detected before or after the droplets bursting, the observed beads are basically ellipsoidal, accompanying mostly $n = 2, 4$ and 6 modes of oscillations. In comparison to isolated, individual drop oscillations

(Shen *et al.*, 2010), our results show that oscillations tend to be in even modes, due probably to the liquid fountain comprising a chain of beads axially connected.

The results for estimated values of the resonance frequencies f_n, obtained based on the above idealized model and experimentally via the FFT analysis, are compared in **Fig. 4.9**. The former—using the Rayleigh (1879) equation, Eq. (4.4), with each of the above three modes of oscillations—leads to three sets of f_n for the UsA driving frequencies of 1.0, 2.0, and 3.0 MHz given in Table 4.2. In the figure, these series of model prediction are depicted ("cross-plotted") by the three curves, using the direct relationship between f_n and f_{ex} given in the inset. Correspondingly shown is the latter—determined for a rather stable part of the beads fountain on Position 1 (see Section 4.3.2)—provided in Table 4.2 as well.

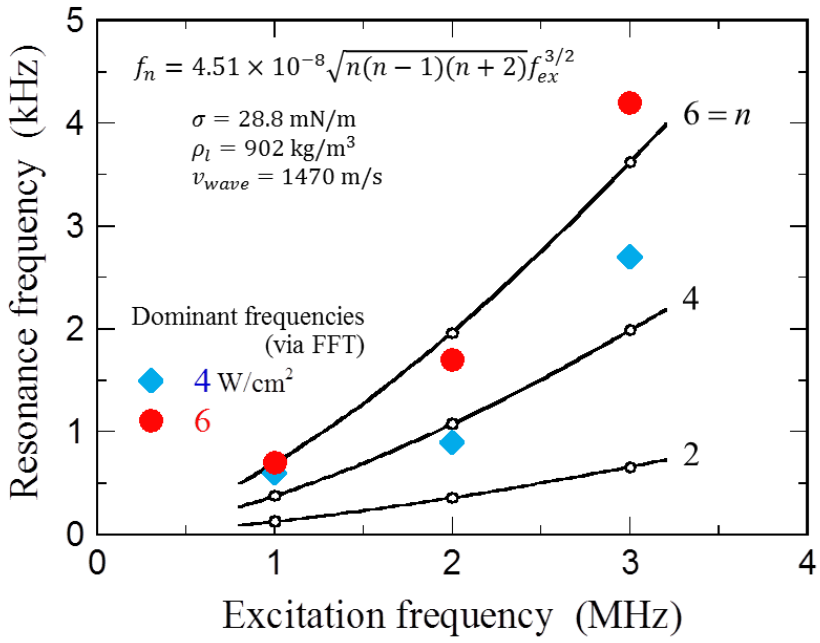

Figure 4.9 Possible predictive capability of proposed model equation given in the inset towards representing dominant frequencies evaluated experimentally via FFT.

A general agreement between the two series of estimates is encouraging despite the simplicity [of the theory of Rayleigh (1879) for linearly perturbed shape oscillations of an isolated spherical drop] vs. the inherent complexity (of the experimental time series as well as FFT signals of nonlinear nature). More specifically, it is tempting to speculate that the experimentally found dominant frequencies for the three driving frequencies could be reproduced by Eq. (4.4): for 4 W/cm^2, with $n = 4$—the beads fountain going through a series of diamond-like

mode of the beads deformation; for 6 W/cm^2, with $n = 6$—going through a series of hexagonal mode. These sets of numerical coincidence have been visually confirmed in that the droplets bursting and mist spreading—in association with higher-order deformation of the beads fountain—are observed at higher input power density but rarely at the lower.

4.3.4 Time–frequency characteristics of beads fountain associated with droplets bursting

Above a given vertical position over the Foundation Region, the beads fountain will exhibit not only its surface movement/oscillations but also its associated dynamics such as droplets bursting. As demonstrated in the previous sections, such additional dynamics noticeable (in Fig. 4.4 or 4.7 for example) on Position 3 at 2.0-MHz or higher driving frequency(ies) may not be clearly identifiable through separate *time-series* and *frequency-only* analyses. The multitude of frequency bands detected there need to be analyzed more rigorously; to this end, the discrete wavelet transform, DWT—a *time–frequency* analysis—is utilized, which can preserve the time-pertaining information in the frequency analysis (see Chapter 3.2).

The time-series data [provided in Fig. 4.7(b)] for 2.0 MHz on Position 3 (shown over a 5-ms period), representing the original waveform of the beads-surface motion at 6 W/cm^2 [Fig. 4.7(a)], is decomposed into wavelets of different frequency bands. **Figure 4.10** shows the results including (a) the DWT map, spanning 10 levels of frequency band obtained using 2^9 (9-bit) data points for the 9 levels of decomposition (shown in the figure over a 25.6-ms period, corresponding to 256 data points out of the original). Note that the original, zeroth-level, data prior to the first decomposition are not shown, while the last (ninth), lowest-frequency, level represents the 10th scaling component—the remnant of the 9th decomposition—called the approximation coefficient or trend term (MathWorks®, 2021). The color variation depicted on the map represents the amplitude/intensity variation in each "smoothed" signal (scaling component).

Specifically, Level –3 (for convenience, "–" will be omitted below) spanning the frequency band of 1.26–2.52 kHz signifies—with appreciably high intensity of periodic fluctuations—the dominant frequency detected primarily for the beads surface motion itself. It is to be noted here that the resonance frequency of $f_6 = 1.98$ kHz, estimated from Rayleigh's for-

mula (1879), Eq. (4.4), for the hexagonal deformation mode ($n = 6$, see Table 4.2), can be said to be a reasonable match.

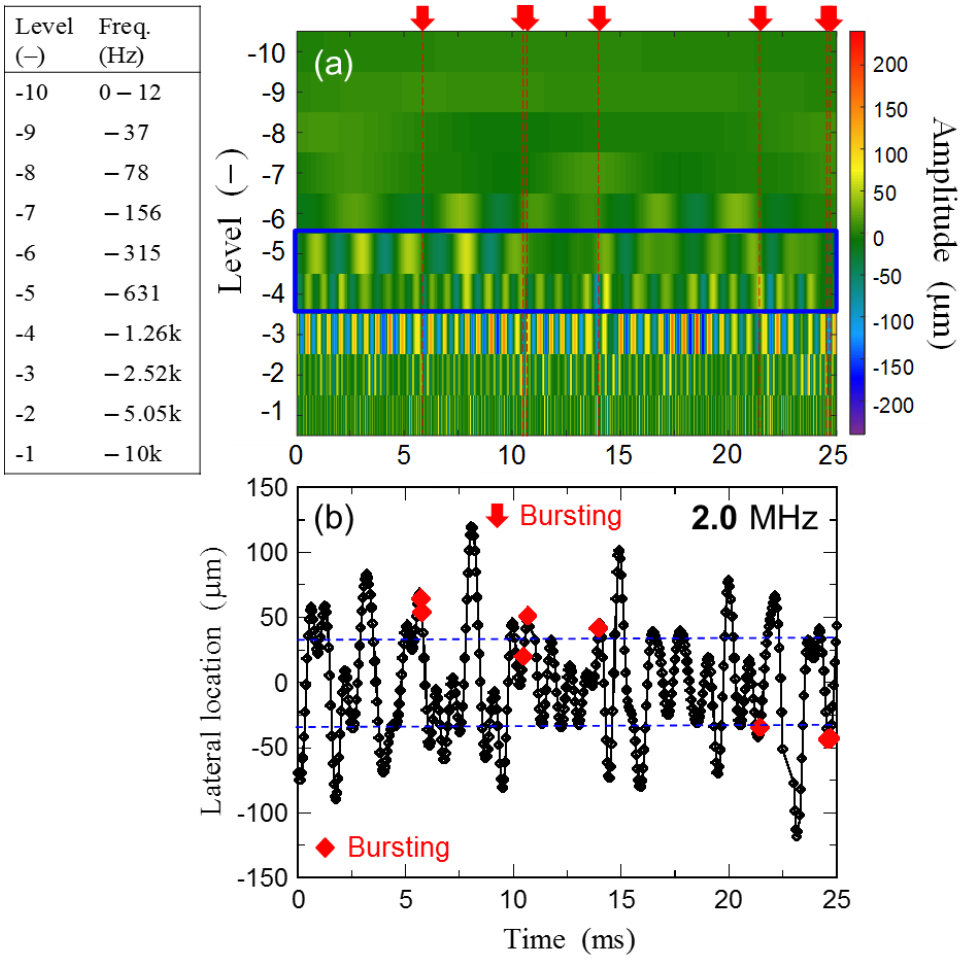

Figure 4.10 (a) DWT map for beads-fountain oscillations at Position 3 (2.0 MHz, 6 W/cm^2) with color variation depicted on the map representing amplitude variation in each "smoothed" signal. Each level represents different frequency band as indicated on the left. Each red arrow and dashed line represent the moment for each droplet bursting. (b) Reconstructed time-series data spanning Levels –4 and –5 for waveform given by fountain surface oscillations at Position 3. Blue dashed lines mark average amplitude of ±34 μm.

At higher frequency levels (Level 1 in particular) the fluctuations are presumed to be of noisy nature. At lower frequency levels (Level 4, 5 or as low as 6)—although the average intensity is not as high as that at Level 3, but still noticeable—time-course fluctuations will prevail with reasonable periodicity. To gain a further insight, an attempt has been made to overlap some of the visual information (extracted from the original high-speed images) onto this DWT map; each red arrow along with the dashed line represents the moment at which indi-

vidual droplet bursting is detected. As could be noticed in Fig. 4.10(a), the droplets bursting is judged to be associated with some of the fluctuating signals at Level 4 or 5, demonstrating one of the advantages of the DWT analysis, *viz.*, detecting the occurrence of event(s) in time which may not be periodic (quasiperiodic at most).

Figure 4.10(b) shows the smoothed signal extracted at Levels 4 and 5 only, spanning the oscillation frequency band 0.32–1.26 kHz. Each event of droplet bursting is marked red. It is found that the bursting tends to occur at or near the peak of rather periodic fluctuations, which should correspond to the resonance frequencies of $f_2 = 0.36$ and/or $f_4 = 1.08$ kHz, predicted in the same manner as above, for the two lower modes (see Table 4.2). The droplets bursting, however, appears to be a rather rare event. As a minimum requirement/criterion for the instability to set in towards the bursting, an average amplitude of the *net* lateral fluctuations (see Section 4.3.2) spanning ±34 μm in this case (the dashed blue lines in the figure) may play a role. Beyond this range, the number of peaks detected is greatly reduced from the total number, as shown in Fig. 4.10(b), due to the prevalence of a large fraction of smaller-amplitude fluctuations. The number of droplets bursting detected would then account for roughly 30% of the "larger" peaks at most in the beads-fountain oscillations.

The corresponding wavelet decomposition for higher driving-frequency (3.0-MHz) case is given in **Fig. 4.11**. The following comparisons against the case given in Fig. 4.10 can be made: 1) the dominant frequency ranges in 2.52–5.05 kHz (Level 2)—signified with a reasonable agreement to Rayleigh's prediction (1879) of $f_6 = 3.63$ kHz [Fig. 4.11(a)]; 2) the wavelets extracted from Levels 3 and 4, spanning the frequency band 0.63–2.52 kHz, would be associated with the droplets bursting [marked red in Fig. 4.11(a) and (b)], occurring—not necessarily—at or near the peaks signified with the resonance frequencies of $f_2 = 0.66$ and/or $f_4 = 1.99$ kHz predicted; and 3) the droplets bursting, being still a rare event (though with larger absolute number than the lower driving-frequency case), with the bursting number accounting for roughly 20% of the "larger" peaks in the beads-fountain oscillations.

While the present findings in regard to the droplets bursting (and the associated mist spreading) are qualitative at this stage, it can be stated at least that the bursting appears to be not a completely random phenomenon but should concur with the fountain periodicity with a limited extent of probability. Furthermore, the beads-fountain oscillations should be a neces-

sary step for triggering the droplets bursting (one-way coupling) at lower driving frequency, on one hand. The bursting in turn may influence the amplitude and frequency of the fountain oscillations (two-way coupling) at higher driving frequency, on the other hand, leading to the complex dynamics observe in this study. One such complex aspect lies in an experimental finding (not indicated in the discussion so far) that the moment and the local location of triggering the droplets bursting (and possibly the succeeding mist spreading) may not necessarily concur with those of "extremes" of the beads-surface oscillations, represented in Figs 4.10 and 4.11 as "peaks" in the time-series data. Further clarification is definitely needed.

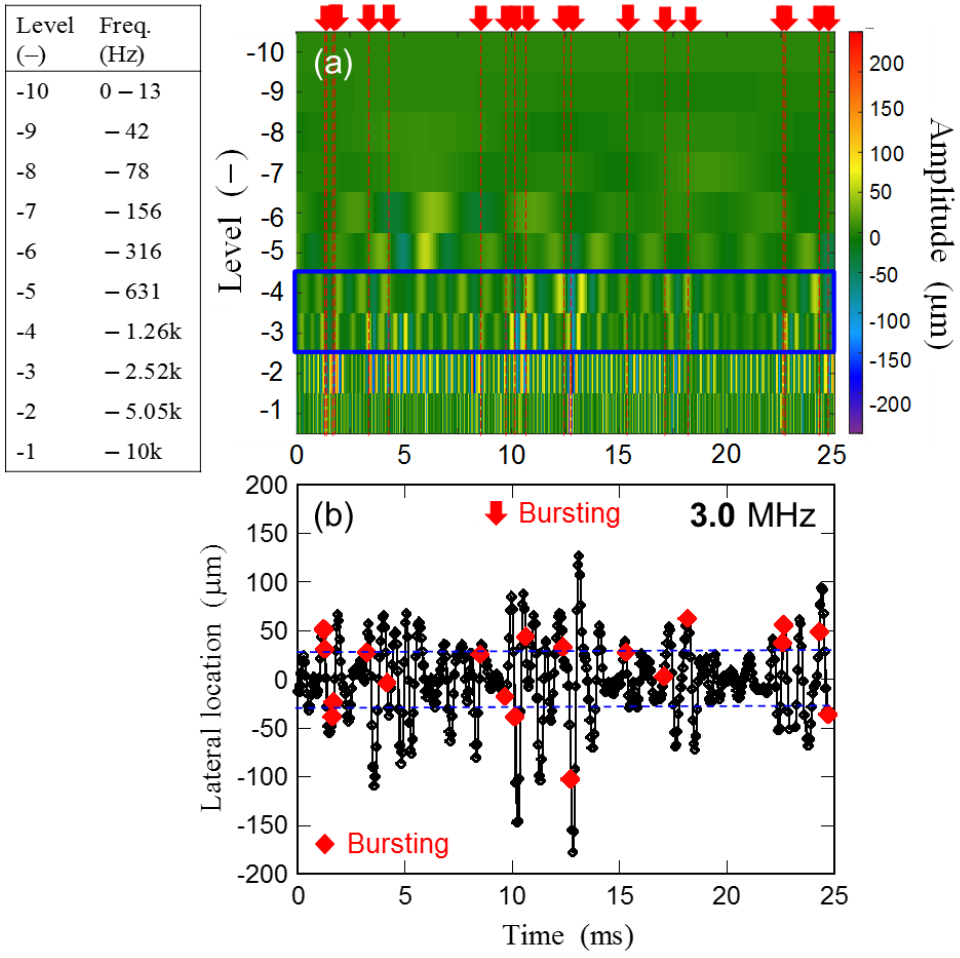

Figure 4.11 (a) DWT map for beads-fountain oscillations at Position 3 (3.0 MHz, 6 W/cm^2). See Fig. 4.10 for details. (b) Reconstructed time-series data spanning Levels –3 and –4 for waveform given by fountain surface oscillations at Position 3. Blue dashed lines mark average amplitude of ±29 μm.

4.4 Concluding Remarks

Upon ultrasonic irradiation under confined operating conditions—driving frequencies of 1–3 MHz and input power densities of 3–6 W/cm^2, the UsA fountain takes the form of *a chain of* "*beads*" in contact, recurring steadily; associated with this cyclic aspect of UsA, droplets bursting and/or mist spreading would arise from the beads fountain, with limited periodicity and probability, as the driving frequency and/or the input power are increased.

The recurring beads themselves are characterized by the UsA *wave-inherent*, "effective" dimension. This *effective beads diameter* is found to almost coincide with *half* the UsA wavelength, which can be specified by *half* the UsA excitation/driving frequency. This predictive scheme is realized via physical principle that the wavelength decreases in inverse proportion to the increasing frequency for a given liquid (thus for a fixed ultrasound speed). The scheme appears to hold as long as the beads diameter will not exceed the capillary length—*i.e.*, provided the fountain-surface wave is of capillary nature—which could be assured for the driving frequency greater than at least 0.8 MHz.

The cyclic properties of the UsA beads fountain, visually exhibited via high-speed imaging, are characterized by the dominant frequency obtained (FFT-evaluated) experimentally. This *primary* periodicity is found to be well predicted based on the simple theoretical model proposed by Rayleigh (1879) with a proper assignment of the mode of cyclic deformation of the fountain beads themselves.

The *secondary* dynamic characteristics associated with the primary beads-fountain periodicity—droplets bursting and/or mist spreading—involve some limited probability and triggering. While the present time–frequency analysis, via DWT, failed to reach their quantitative elucidation due to their complexity, some requirement(s) are identified in terms of higher probability for the droplets bursting to be triggered.

References

Antonevich, J. N., "Ultrasonic atomization of liquids," *IRE Trans. Ultrasonic Eng.*, **PGUE-7** 6–15 (1959).

Barreras, F., H. Amaveda and A. Lozano, "Transient high-frequency ultrasonic water atomization," *Exp. Fluids*, **33** 405–413 (2002). https://doi.org/10.1007/S00348-002-

0456-1.

Blamey, J., L.Y. Yeo and J.R. Friend, "Microscale capillary wave turbulence excited by high frequency vibration," *Langmuir*, **29**, 3835–3845 (2013). https://doi.org/10.1021/la304608a.

Boguslavskii, Yu.Ya. and O.K. Eknadiosyants, "Physical mechanism of the acoustic atomization of a liquid," *Sov. Phys. Acoust.*, **15** 14–21 (1969).

Bouwhuis, W., K.G. Winkels, I.R. Peters, P. Brunet, D. van der Meer and J.H. Snoeijer, "Oscillating and star-shaped drops levitated by an airflow," *Phys. Rev. E*, **88**, 023017 (2013). https://doi.org/10.1103/PhysRevE.88.023017.

Chui, C.K., *An Introduction to Wavelets*, Academic Press, New York, NY (1992). https://www.elsevier.com/books/an-introduction-to-wavelets/chui/978-0-12-174584-4.

Collins, D.J., O. Manor, A. Winkler, H. Schmidt, J.R. Friend and L.Y. Yeo, "Atomization off thin water films generated by high-frequency substrate wave vibrations," *Phys. Rev. E*, **86**, 056312 (2012). https://doi.org/10.1103/PhysRevE.86.056312.

Dalmoro, A., A.A. Barba and M. d'Amore, "Analysis of size correlations for microdroplets produced by ultrasonic atomization," *Sci. World J.*, **2013**, 482910 (2013). https://doi.org/10.1155/2013/482910.

Daubechies, I., *Ten Lectures on Wavelets*, Society for Industrial and Applied Mathematics (SIAM) Press, Philadelphia, PA (1992). https://doi.org/10.1137/1.9781611970104. https://epubs.siam.org/doi/book/10.1137/1.9781611970104.

Fan, L.-S. and K. Tsuchiya, *Bubble Wake Dynamics in Liquids and Liquid–Solid Suspensions*, Butterworth–Heinemann, Stoneham, MA (1990). https://www.sciencedirect.com/book/9780409902860/bubble-wake-dynamics-in-liquids-and-liquid-solid-suspensions.

Fujita, K. and K. Tsuchiya, "Cavitating bubble inside liquid fountain of beads associated with ultrasonic atomization," *Proc. 8th Int. Conf. Multiphase Flow (ICMF 2013)*, Paper 863/1–5 (2013).

Inui, A., A. Honda, S. Yamanaka, T. Ikeno and K. Yamamoto, "Effect of ultrasonic frequency and surfactant addition on microcapsule destruction," *Ultrason. Sonochem.*, **70**, 105308 (2021). https://doi.org/10.1016/j.ultsonch.2020.105308.

Kelvin, L. (W. Thomson), "Oscillations of a liquid sphere," *Math. Phys. Papers*, **3**, 384–386 (1890).

Khattab, I.S., F. Bandarkar, M.A.A. Fakhree and A. Jouyban, "Density, viscosity, and surface tension of water–ethanol mixtures from 293 to 323K," *Korean J. Chem. Eng.*, **29**, 812–817 (2012). https://doi.org/10.1007/s11814-011-0239-6.

Kirpalani, D.M. and F. Toll, "Revealing the physicochemical mechanism for ultrasonic separation of alcohol–water mixtures," *J. Chem. Phys.*, **117**, 3874–3877 (2002). https://doi.org/10.1063/1.1495849.

Kojima, Y., Y. Asakura, G. Sugiyama and S. Koda, "The effects of acoustic flow and mechanical flow on the sonochemical efficiency in a rectangular sonochemical reactor," *Ultrason. Sonochem.*, **17**, 978–984 (2010). https://doi.org/10.1016/j.ultsonch.2009.11.020.

Kooij, S., A. Astefanei, G.L. Corthals and D. Bonn, "Size distributions of droplets produced by ultrasonic nebulizers," *Sci. Rep.*, **9**, 6128 (2019). https://doi.org/10.1038/s41598-019-42599-8.

Lamb, H., *Hydrodynamics* (6th ed.), Cambridge University Press, Cambridge, England (1932).

Lang, R.J., "Ultrasonic atomization of liquids," *J. Acoust. Soc. Am.*, **34**, 6–8 (1962). https://doi.org/10.1121/1.1909020.

Lee, J., K. Yasui, T. Tuziuti, T. Kozuka, A. Towata and Y. Iida, "Spatial distribution enhancement of sonoluminescence activity by altering sonication and solution conditions," *J. Phys. Chem. B*, **112**, 15333–15341 (2008). https://doi.org/10.1021/jp8060224.

Lee, J., M. Ashokkumar, K. Yasui, T. Tuziuti, T. Kozuka, A. Towata and Y. Iida, "Development and optimization of acoustic bubble structures at high frequencies," *Ultrason. Sonochem.*, **18**, 92–98 (2011). https://doi.org/10.1016/j.ultsonch.2010.03.004.

Liu, F., G. Ghigliotti, J.J. Feng and C.-H. Chen, "Numerical simulations of self-propelled jumping upon drop coalescence on non-wetting surfaces," *J. Fluid Mech.*, **752**, 39–65 (2014). https://doi.org/10.1017/jfm.2014.320.

Liu, H. and K. Wang, "A study of characteristic extraction for transformer oscillation wave based on DWT analysis," *J. Phys. Conf. Ser.*, **1311**, 012014 (2019). https://doi.org/10.1088/1742-6596/1311/1/012014.

MathWorks®, "MATLAB® Wavelet Toolbox™, Discrete Multiresolution Analysis, Practical

Introduction to Multiresolution Analysis," Help Center R2021a, Natick, MA (2021). https://jp.mathworks.com/help/wavelet/index.html?lang=en.

Mijaković, M., B. Kežić, L. Zoranić, F. Sokolić, A. Asenbaum, C. Pruner, E. Wilhelm and A. Perera, "Ethanol–water mixtures; ultrasonics, Brillouin scattering and molecular dynamics," *J. Mol. Liq.*, **164**, 66–73 (2011). https://doi.org/10.1016/j.molliq.2011.06.009.

Neppiras, E.A. and B.E. Noltingk, "Cavitation produced by ultrasonics: theoretical conditions for the onset of cavitation," *Proc. Phys. Soc. B*, **64**, 1032–1038 (1951). https://doi.org/10.1088/0370-1301/64/12/302.

Qi, A., L.Y. Yeo and J.R. Friend, "Interfacial destabilization and atomization driven by surface acoustic waves," *Phys. Fluids*, **20**, 074103 (2008). https://doi.org/10.1063/1.2953537.

Ramisetty, K.A., A.B. Pandit and P.R. Gogate, "Investigations into ultrasound induced atomization," *Ultrason. Sonochem.*, **20**, 254–264 (2013). https://doi.org/10.1016/j.ultsonch.2012.05.001.

Rayleigh, L. (J.W. Strutt), "On the capillary phenomena of jets," *Proc. R. Soc. Lond.*, **29**, 71–97 (1879). https://doi.org/10.1098/rspl.1879.0015.

Rozenberg, L.D. (Ed.), "Physical principles of ultrasonic technology," **2**, 4–88 Springer (1973).

Sato, M., K. Matsuura and T. Fujii, "Ethanol separation from ethanol–water solution by ultrasonic atomization and its proposed mechanism based on parametric decay instability of capillary wave," *J. Chem. Phys.*, **114**, 2382–2386 (2001). https://doi.org/10.1063/1.1336842.

Satomi, K., Y. Mori and K. Tsuchiya, "Ultrasonic atomization—its structure and dynamics associated with liquid fountain of corrugated beads," *Proc. 10th Int. Conf. Multiphase Flow (ICMF 2019)*, Paper 178489 (2019).

Shen, C.L., W.J. Xie and B. Wei, "Parametrically excited sectorial oscillation of liquid drops floating in ultrasound," *Phys. Rev. E*, **81**, 046305 (2010). https://doi.org/10.1103/PhysRevE.81.046305.

Simon, J.C., O.A. Sapozhnikov, V.A. Khokhlova, L.A. Crum and M.R. Bailey, "Ultrasonic atomization of liquids in drop-chain acoustic fountains," *J. Fluid Mech.*, **766**, 129–146 (2015). https://doi.org/10.1017/jfm.2015.11.

Simon, J.C., O.A. Sapozhnikov, V.A. Khokhlova, Y.-N. Wang, L.A. Crum and M.R. Bailey, "Ultrasonic atomization of tissue and its role in tissue fractionation by high intensity focused ultrasound," *Phys. Med. Biol.*, **57**, 8061–8078 (2012). https://doi.org/10.1088/0031-9155/57/23/8061.

Son, Y., M. Lim, M. Ashokkumar and J. Khim, "Geometric optimization of sonoreactors for the enhancement of sonochemical activity," *J. Phys. Chem. C*, **115**, 4096–4103 (2011). https://doi.org/10.1021/jp110319y.

Tomita, Y., "Jet atomization and cavitation induced by interactions between focused ultrasound and a water surface," *Phys. Fluids*, **26**, 097105 (2014). https://doi.org/10.1063/1.4895902.

Trinh, E. and T.G. Wang, "Large-amplitude free and driven drop-shape oscillations: experimental observations," *J. Fluid Mech.*, **122**, 315–338 (1982). https://doi.org/10.1017/S0022112082002237.

Trinh, E., A. Zwern and T.G. Wang, "An experimental study of small-amplitude drop oscillations in immiscible liquid systems," *J. Fluid Mech.*, **115**, 453–474 (1982). https://doi.org/10.1017/S0022112082000858.

Tsuchiya, K., H. Hayashi, K. Fujiwara and K. Matsuura, "Visual analysis of ultrasonic atomization and its associated phenomena," *Earozoru Kenkyu* (*J. Aerosol Res.* in Japanese), **26**, 11–17 (2011). https://doi.org/10.11203/jar.26.11.

Tsuchiya, K., S. Ide, Y. Mori and T. Saito, "Time–frequency analysis of local fluctuations induced by bubble flow," *Proc. 10th APCChE Cong.*, Paper 4E-05 (2004). https://www.jstage.jst.go.jp/article/apcche/2004/0/2004_0_198/_pdf.

Watanabe, A., K. Hasegawa and Y. Abe, "Contactless fluid manipulation in air: droplet coalescence and active mixing by acoustic levitation," *Sci. Rep.*, **8**, 10221 (2018). https://doi.org/10.1038/s41598-018-28451-5.

Zhang, H., X. Zhang, X. Yi, F. He, F. Niu and P. Hao, "Dynamic behaviors of droplets impacting on ultrasonically vibrating surfaces," *Exp. Therm. Fluid Sci.*, **112**, 110019 (2020). https://doi.org/10.1016/j.expthermflusci.2019.110019.

Chapter 5

Frequency specificity of liquid-fountain swinging with mist generation: Effects of ultrasonic irradiation angle

5.1 Introduction

Ultrasonic atomization (UsA) techniques have been employed as—with an ultimate goal being—a flexible green alternative for energy-efficient processes including: gas–liquid mass transfer enhancement/intensification (Dong *et al.*, 2015; Tamidi *et al.*, 2021), wastewater treatment (Mahamuni and Adewuyi, 2010; Kunde and Sehgal, 2021), air purification (Tay *et al.*, 2016, 2017; Wei *et al.*, 2019; Marjanian *et al.*, 2021), drug delivery (Dalmoro *et al.*, 2013; Kaur *et al.*, 2021), as well as solvent–solute (or particles) separation (Nii and Oka, 2014; Kim *et al.*, 2015; Hinman *et al.*, 2019) and/or concentration (Kirpalani and Suzuki, 2011; Mai *et al.*, 2019).

Among those applications, a typical technique of installing the ultrasonic transducer is to set it, in the form of an oscillating disk, within a liquid and to irradiate ultrasonic wave almost vertically upward—but with a *slight tilt* (Matsuura *et al.*, 1995; Sato *et al.*, 2001). In such a configuration, as the bulk liquid is irradiated at a high driving frequency (≈800 kHz or higher), a fountain of liquid will emerge from its free surface and micro- to nano-sized droplets could be generated—as mist—from the fountain.

If the installation angle/direction is exactly vertical, *viz.*, the transducer's *flat* disk parallel to (or its angle being 0° vs.) the horizontal free surface, the acoustic fountain will be disturbed rather profoundly—either directly by relatively large drops of liquid separated from the fountain tip and then falling or indirectly by the associated undulation of the surrounding free surface (*e.g.*, Tsuchiya *et al.*, 2011)—which ideally should be avoided. The mist of droplets, on the other hand, have been investigated as mass-transfer or aerosol carriers by many researchers—in particular, regarding the effects of a variety of operating parameters on the droplet size distribution (DSD), such as the driving frequency, oscillating-disk diameter, input power, liquid depth, liquid surface tension and viscosity, and the liquid-phase temperature (*e.g.*, Kobara *et al.*, 2010; Nii and Oka, 2014; Kudo *et al.*, 2017; Kooij *et al.*, 2019; Panão, 2022).

Whether tilted or not, the acoustic liquid fountain was proposed—based on a visualization study—to have a general configuration characterized by dynamics of the *four-region structure* consisting of A) Foundation, B) Bumpy-Surface, C) Finely-Structured Surface and D) Lumped-Crest Regions (Tsuchiya *et al.*, 2011). While such qualitative information needs to be clarified based on mechanistic support, it is quite a difficult task to reproduce or at least verify the fountain's dynamic structure over a diversity of the above-said operational parameters to be taken into account.

In regard to the mechanistic description of the fountain structure, the information available in the literature (*e.g.*, Xu *et al.*, 2016; Kim *et al.*, 2021; Aikawa and Kudo, 2021; Orisaki and Kajishima, 2022) is mostly limited to a mere precursory structure or mound-like fountain. Xu *et al.* (2016) conducted numerical simulation to realize the shape of the acoustic fountain with different ultrasonic parameters, through rigorous formulation of the theoretical bases including the inhomogeneous Helmholtz equation for the acoustic pressure distribution and the equations of momentum transport with the continuity for the liquid flow field to predict the dynamic behavior of the liquid free surface. A notable finding is that the steady-attained height of acoustic fountain "step-increased with an increase in the acoustic pressure," with a step increment of half the ultrasound wavelength. In addition, they found that "the ultrasonic field between the transducer flat disk and the fountain surface was an anti-resonant pressure field"; with this they claimed that the radiation pressure is a minimum, leading to the fountain surface tending to be stable. Regarding the geometry/structure of the fountain, however, it was limited to a mere precursory structure or mound-like fountain, while the bottom radius of the fountain was noted to be roughly the same as the transducer-disk radius.

Likewise for a mere protuberant state of water fountain, Kim *et al.* (2021) investigated experimentally the mechanism controlling its stability. For better spatiotemporal control, such fountains were induced by *focused* ultrasound at two distinct frequencies of ultrasound, 0.55 and 1.1 MHz; particle image velocimetry (PIV) was used to determine "the induced flow field around the ultrasonic *focal spot*." By varying the pressure level of the transducers, they observed three different regimes, *viz.* weak, intermediate (stable) and highly forced (explosive) fountains. Two notable findings, in particular, lie in "the fountain height undergoing a stepwise change between the regimes in response to the increase in acoustic pressure," as reported

by Xu *et al.* (2016), and the acoustic radiation force being the dominant driving force for the fountain formation. These findings led them to propose "a simple model to estimate the shape of a stable fountain, which accounts for the acoustic pressure as well as gravity, surface tension and axial momentum" and successfully predicts the geometry of the weak and stable fountains.

When it comes to the structure and dynamics of acoustic fountains to be examined in this study, a typical fountain is no longer a mere protrusion, nor stable, and associated with mist spreading (out of the Finely-Structured Surface Region) as well as large drops and/or liquid ligaments formed as a result of tip breakup (the Lumped-Crest Region). Kawase *et al.* (2006) and Yasuda (2011) used a 2.4-MHz ultrasonic transducer with installation angle of 5° at input powers of 20 and 18 W, respectively, to investigate the effects of carrier gas specifically and various operating conditions including the liquid properties on attaining efficient collection of UsA-concentrated alcohols. They provided a preferred flow mode of the carrier as well as some optimum conditions but no specific information regarding the fountain characteristics other than those of the mist as well as drops.

In this study we apply high-speed imaging/image processing to observe/analyze detailed dynamics of the acoustic fountain by changing the angle of ultrasonic irradiation. The study involves mainly two objectives: to find an optimum irradiation angle, if indeed exists, from the viewpoint of operability/stability of and effective mist generation out of the UsA fountain; and to quantify its periodicity both in *axial* "growth–breakup" cycle and *lateral* "swinging." The expected outcome of novelty would lie in attempting to reveal factor(s) triggering mist emergence via experimental frequency analysis (fast Fourier transform) and theoretical prediction (pendulum model).

5.2 Experimental

The experimental setup used for visualizing the UsA process is shown in **Fig. 5.1**. An ultrasonic transducer (Honda Electronics HM-2412: 2.4 MHz) was placed on the bottom of a square vessel with its dimensions, 200×200×185(height) mm. The transducer element (oscillating disk) itself was 20.0 mm in diameter, having an effective oscillating diameter of 16 mm. The installation or setting angle, θ_T, of the ultrasonic transducer was tested over the range

0°–10° with a 1° increment. The input power applied to the transducer was changed over 7–13 W (input power density examined then ranged 3.5–6.5—or three specific values of 3.5, 5.0 and 6.5—W/cm^2, which is exclusively used in this study as an operating parameter).

The distance from the center of the oscillator to the free surface of the liquid (effective liquid depth) was kept 20 mm, or 27.5 mm above the vessel bottom. The liquid used was ion-exchanged water (Merck Millipore Elix® Essential UV 3), temperature of which was adjusted, before each run, to 25°C in a constant temperature bath. During the UsA over 10 seconds of operation at most, the liquid properties are presumed to be kept invariant.

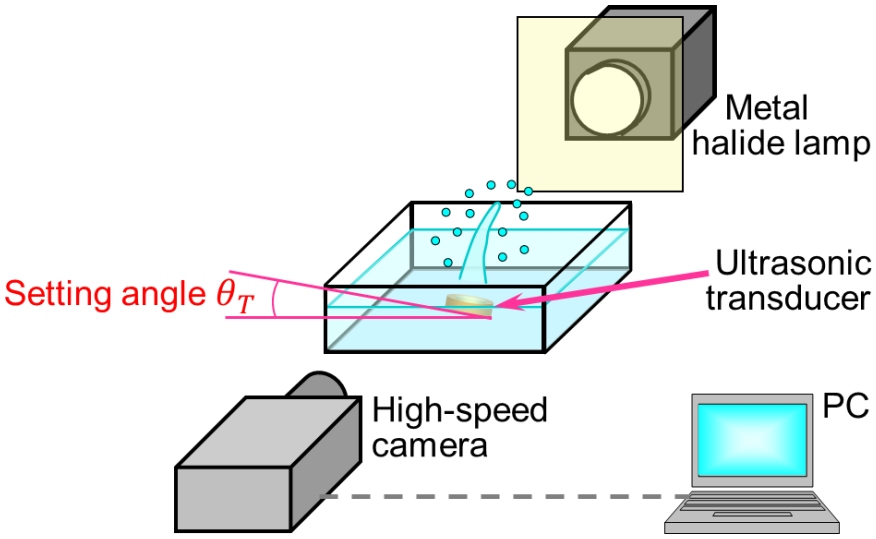

Figure 5.1 Schematic diagram of the experimental system for visual observation of ultrasonic atomization process for inclined liquid fountain.

5.2.1 High-speed visualization

The visualization was carried out using a high-speed camera (REDLAKE MotionPro X4: frame rate(s) up to 5,000 fps, with a resolution of at least 512×512 pixels, and an exposure time as short as 197 μs) under backlighting using a metal halide lamp (Lighterrace MID-25FC). The imaging was started 5 s after the transducer was turned on, and a 1-s period of data was recorded. A sheet of light diffuser was installed between the liquid fountain and the lamp, thus reducing the non-uniformity of backlighting.

5.2.2 Image analysis

Figure 5.2 depicts—through a typical sequence of images—how two important "instanta-

neous" aspects of the liquid-fountain dynamics are determined visually: 1) the *axial* variations of its tip, confined by breakup and attained heights of the liquid fountain, and 2) its *lateral* fluctuations characterized by the fountain swinging. Note that the very initial period of 0.6 ms or so covers the non-periodic startup growth phase, which should be excluded from the cyclic growth-and-breakup phase (see the 2nd to 5th frames covering one cycle). An image analysis software (DITECT Dipp Motion) was used to track the breakup and attained liquid heights; the vertical distance spanned over the period between the moment of fountain breakup and the succeeding one signifies the growth rate of the fountain, while the number of breakup events per unit time defines the breakup frequency.

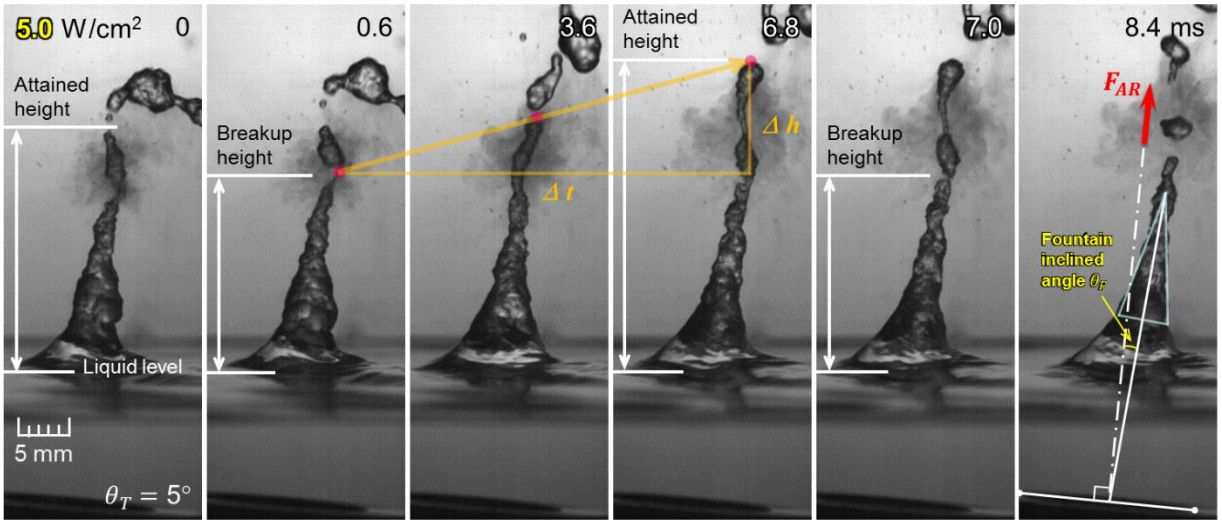

Figure 5.2 Time course of liquid-fountain dynamics signifying its axial variations, based on which the fountain's breakup and attained heights are defined; its lateral fluctuations specified by θ_F ($+\theta_T$).

With the aid of a video analysis software (KEYENCE Movie Editor) the instantaneous state of swinging liquid fountain was specified in terms of its angle of inclination, θ_F, as depicted in Fig. 5.2 (see the far right): first, the line perpendicular to the transducer disk (tilted by θ_T) is drawn, which is assigned to represent the "virtual axis" of the fountain emanating—acoustically radiating—from the center of the transducer; second, two tangential lines are drawn along the profile of the fountain surface to approximate the fountain outline as an equilateral triangle; the angle between the center line of the triangle and the virtual axis specifies the "net" inclined angle of fountain.

5.3 Results and Discussion

The effects of the angle (θ_T) of the ultrasonic irradiation, or transducer installation/setting, are presented below on dynamic (oscillating and/or intermittent) characteristics of the liquid fountain for given input power densities; either axial or lateral direction is to be prescribed to each characteristic under discussion.

It is noted here that the input power density may reflect the so-called *acoustic strength*, which could be a measure of acoustic *radiation pressure*/force—depicted schematically in Fig. 5.2 (designated as F_{AR}, a sort of "tension" force trying to maintain the fountain straight along a given direction, presumably the transducer axis)—in a *traveling*-wave field or acoustic *streaming* in a *standing*-wave field (Lee *et al.*, 2008, 2011; Son *et al.*, 2011). These two competing factors would contribute to the liquid surface being pushed upwards, leading to the eventual formation of liquid fountain (*e.g.*, Orisaki and Kajishima, 2022). It is also speculated that the more extensive these contributions are, the faster the fountain growth may be, and the greater the amount of resulting atomization would be.

5.3.1 Structure of liquid fountain with mist

The images obtained of liquid fountain and/or some associated mist visible for different transducer setting angles $\theta_T = 0°$, 2°, 4°, 5°, 6° and 7° at the applied power density of 5.0 W/cm^2 are shown in **Fig. 5.3**. When the ultrasonic transducer is placed horizontally (0°), the fountain will be formed vertically along the direction of the transducer axis; individual small (visible) droplets along with the mist are observed to be scattered irregularly/intermittently from the surface around the so-called Finely-Structured Surface Region (FSSR, Tsuchiya *et al.*, 2011; Fujita and Tsuchiya, 2013) mostly below the liquid fountain tip, or the Lumped-Crest Region (LCR). As the fountain ruptures vertically, the (large) separated tip drop—the remnant of the lumped crest—will not only disrupt the oscillation state of the fountain, often ending up merging with the remaining fountain, but also cause such disturbed fluctuations of the fountain surface to affect the direction of a higher part—including the FSSR as well as LCR—of the fountain in turn.

With an increase in θ_T, the liquid fountain will be inclined correspondingly and may be bent in between—prior to reaching its tip—under the influence of gravity, while the axial in-

terference from the separated drop(s) will be gradually reduced. In the range of θ_T increasing from 0° to 5°, the mist visually identifiable decreases gradually, but noticeably above 6°; none identifiable/detected beyond 7°. The upper limit of θ_T in operating the UsA transducer properly is thus confined from the viewpoint of generating the mist.

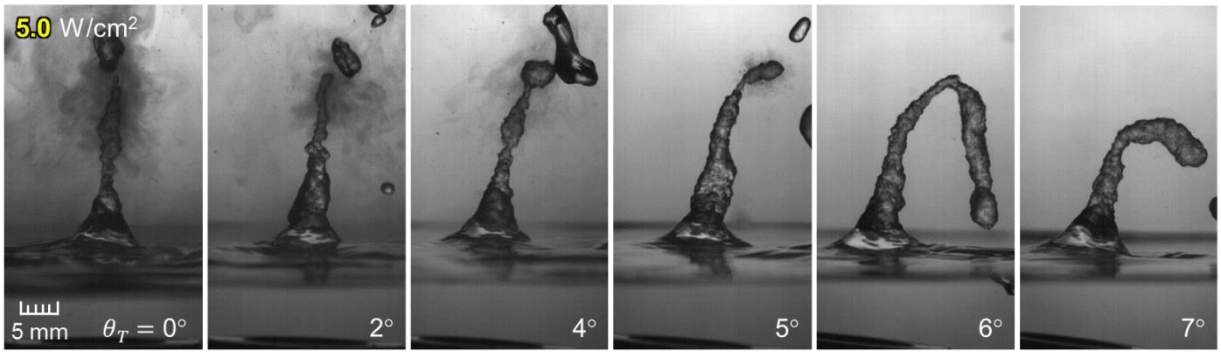

Figure 5.3 Images of liquid fountain obtained for different transducer setting angles at input power density of 5.0 W/cm^2.

5.3.2 Axial growth and breakup dynamics of liquid fountain

The liquid fountain will repeat its dynamic phases between growth and breakup processes on a ms-time scale. Based on the image-analysis procedure described in Section 5.2.1, the breakup/attained heights, breakup frequency, and growth rate of the fountain were determined for different input power densities. Three sets of data are provided under each condition to show the degree of reproducibility for each parameter.

Figure 5.4(a) shows the variations in the liquid-fountain breakup and attained heights for 3.5, 5.0 and 6.5 W/cm^2 with increasing transducer setting angle θ_T. Both the fountain heights increase with input power density. Over the range of θ_T examined, both the heights are regarded to be essentially invariant with the angle θ_T. As shown in Fig. 5.4(b) and (c), respectively, the breakup frequency and the growth rate of the fountain take maximum values at 2°; the former being clearly exhibited (by sharp peaks) but the latter being indicated by the moderate hills. Figure 5.4(c) in particular signifies the presence of a transition range (from 4° to 6°) that demarcates the high growth-rate range (0°–4°) and the low-to-negligible range (6° or higher).

It is to be noted here that the appreciable reduction in the breakup frequency near $\theta_T = 0°$ ($\leq 1°$) could stem from the disruption of the oscillation “rhythm” of the fountain due to verti-

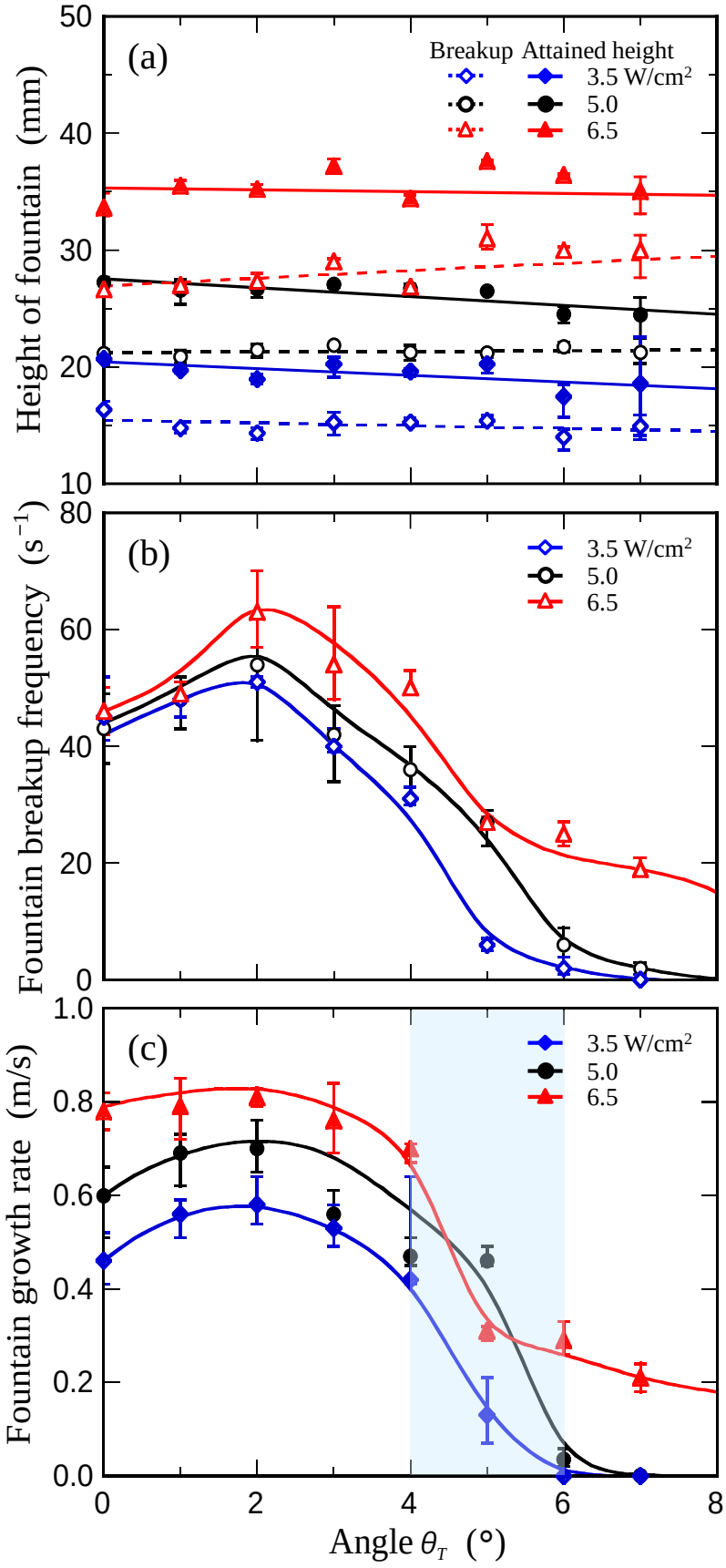

Figure 5.4 Effects of transducer setting angle on (a) breakup and attained heights, (b) breakup frequency and (c) growth rate of liquid fountain for input power densities of 3.5, 5.0 and 6.5 W/cm^2.

cally interacting drops mentioned above; slightly tilted transducer setting angle (0°–3°) appears to have little impact on the fountain growth rate. Based on the image analysis, atomization is observed to occur both before and after the fountain breakup rather cyclically. It is suffice to say here that the transducer installation angle should be set 2° in terms of effective mist generation and fluid dynamic stability of the liquid fountain.

5.3.3 Time-dependent characteristics of fountain swinging

The amplitude and frequency of fountain oscillations for two representative transducer setting angles, θ_T of 2° and 5°, were analyzed together with the amount of mist "determined" from the visual appearance on the relevant images like the ones shown in Fig. 5.3.

Figure 5.5(a) shows, for the above two values of θ_T at 5.0 W/cm^2, time variations of the (net) fountain inclined angle θ_F along with the associated mist spreading detected. The position of red triangles in the figure specifies the moment (and the angle) of mist generation; the size of each triangle signifies the amount of atomization—judged to be either small or large, limited by the visual information only (see the inset images). While the fountain oscillations in θ_F are occasionally disrupted by tip-separated drops for $\theta_T = 2°$, the quasi-periodicity in the θ_F variation over time is still evident. Regarding the atomization, it is mostly triggered in cycle as the fountain inclined angle is shifted from positive to negative in the 0°±5° range; particularly noticeable is multiple, sequential occurrence of misting (regarded as a single event) when the amplitude of oscillations in θ_F is larger. For the larger $\theta_T = 5°$, the fountain is no longer directly disturbed by the separated falling drops. In comparison to the smaller θ_T, the amplitude of θ_F oscillations, the angular range of triggering atomization, and more importantly/drastically the degree of occurrence as well as the amount of atomization will all decrease. In addition, during one swing cycle, essentially one-time mist generation can only be detected.

The periodic (or at least quasi-cyclic) natures in the lateral and axial dynamics described above can here be contrasted more specifically in terms of their apparent frequencies. As shown in Fig. 5.5(b), selected portions of the fountain-swinging and growth–breakup time-series data would exhibit each own frequency(ies). The latter fluctuates more quickly than the former, with the frequency ratio of roughly 5 or greater—signifying the multiple (5–8 times) occurrence of axial growth and breakup in one lateral oscillation period. This frequency "gap"

indicates that the fountain height could be regarded as effectively constant, averaged over one cycle of the fountain swinging. It should be noted here that even though the amplitude of oscillations in θ_F is appreciable during the swinging, the Foundation Region (FR) always formed in line with the direction of ultrasonic irradiation (see the inset t_3). Of particular importance, the heights of the FR and Bumpy-Surface Region (BSR) are essentially time-invariant (below the dashed line), and the occurrence of mist generation is mostly confined to the time-varying (but cyclic) FSSR. In this sense, the fountain swinging could be regarded as a motion of a dual-body—double-compound—pendulum with the FR as the pivoting region (Tsuchiya and Fan, 1988; Fan and Tsuchiya, 1990; to be discussed more extensively in Section 5.3.4).

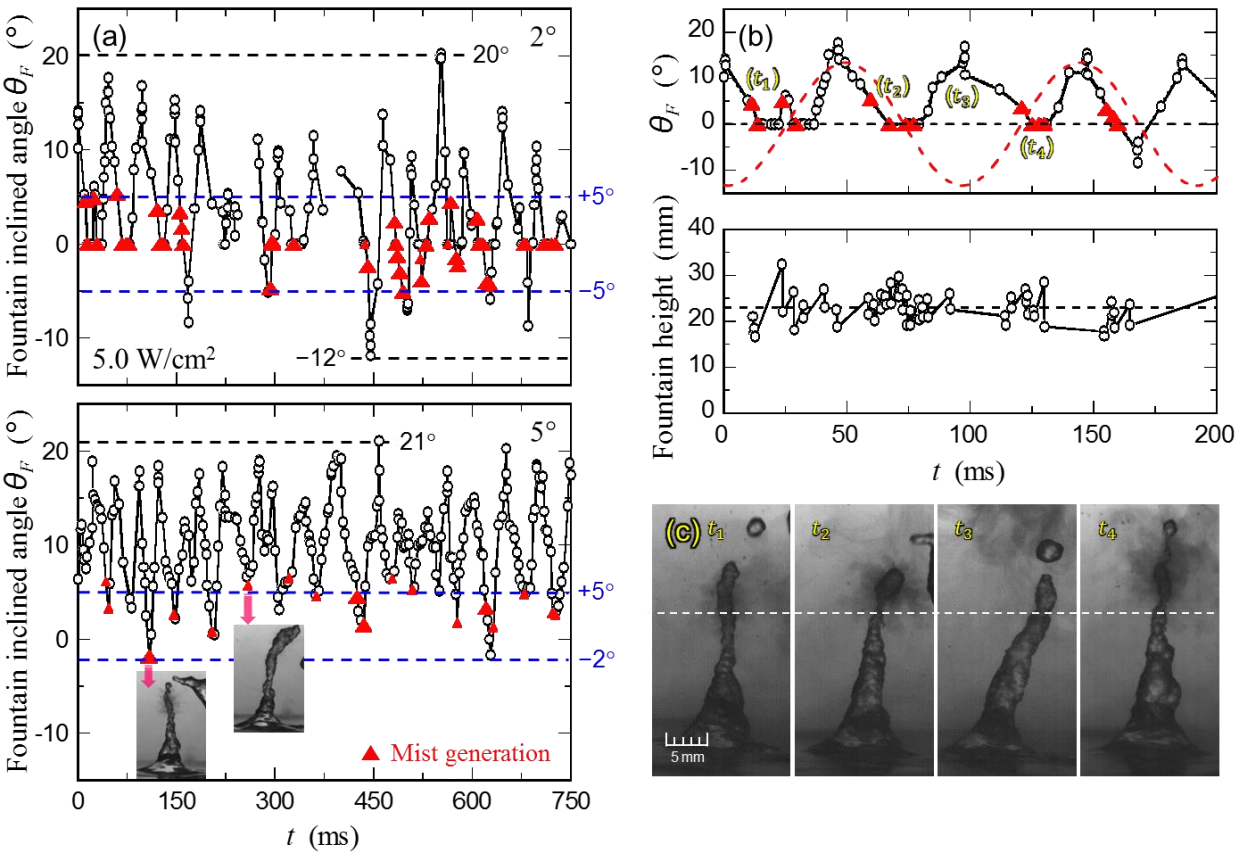

Figure 5.5 Time variations (a) in fountain inclined angle, associated with mist generation, for transducer setting angles θ_T of 2° and 5° at 5.0 W/cm^2, and (b) in fountain inclined angle and height for $\theta_T = 2°$ over selected time interval with (c) some images of fountain for representative phases of oscillations.

Figure 5.6(a) and (b) shows the effects of the input power on the swinging characteristics at $\theta_T = 2°$ and the corresponding FFT-analysis results, respectively. It is important to keep in mind that, on each time-series data given in Fig. 5.6(a), virtual/auxiliary data points (marked by small dots) are added, obtained via Lagrange interpolation; these points are necessary to perform FFT which requires equal intervals in the time coordinate. Some quasi-periodicity in the variations of the fountain inclined angle over time is apparent for all the input power densities. With increasing input power density, the amplitude of oscillations in θ_F tends to decrease, while the degree of occurrence and amount of atomization do increase. Based on the FFT analysis, it is found—while quasi-periodic—that the swinging fountain has a dominant frequency of 21, 21 and 24 Hz for 3.5, 5.0 and 6.5 W/cm^2, respectively. The same FFT analysis at $\theta_T = 5°$ for 5.0 W/cm^2 provides a dominant frequency of 18 Hz (not shown in the figure).

5.3.4 Model-evaluated periodicity of fountain swinging

As described in Sections 5.3.2 and 5.3.3, the acoustic liquid fountain will exhibit respectively quasi-periodic oscillations with recurring growth-and-breakup in the axial direction and swinging in the lateral direction—the latter in particular, if the ultrasound is irradiated on the tilt—under the influence of gravity. The latter dynamics could then be regarded as a motion of a *planar* compound pendulum. In such phenomenological, intuitive modeling, a sequence of assumptions are needed for its mathematical formulation and predictive realization of the experimental findings described so far. The first set of assumptions based on the visual information (see Figs 5.2 and 5.3) are listed as follows:

1) The fountain, while altering its local shape dynamically, consists on average of two parts during the growth-and-breakup period, simplified in geometry by a "cone" and cigar-shape or more simply a "cylinder." The former involves the FR and BSR, the latter the FSSR which accompanies mist spreading (Fig. 5.2);
2) This dual-part body as a single entity will be forced to maintain its axis straight along the tilted direction of θ_T—more stably if smaller than 4° (Figs 5.2 and 5.3, the fountain's equilibrium position *presumed*);
3) When the tilting is increased beyond $\theta_T = 4$ or 5°, this single entity will experience its bending at the "connecting" region between the cone and the cylinder (Fig. 5.3);

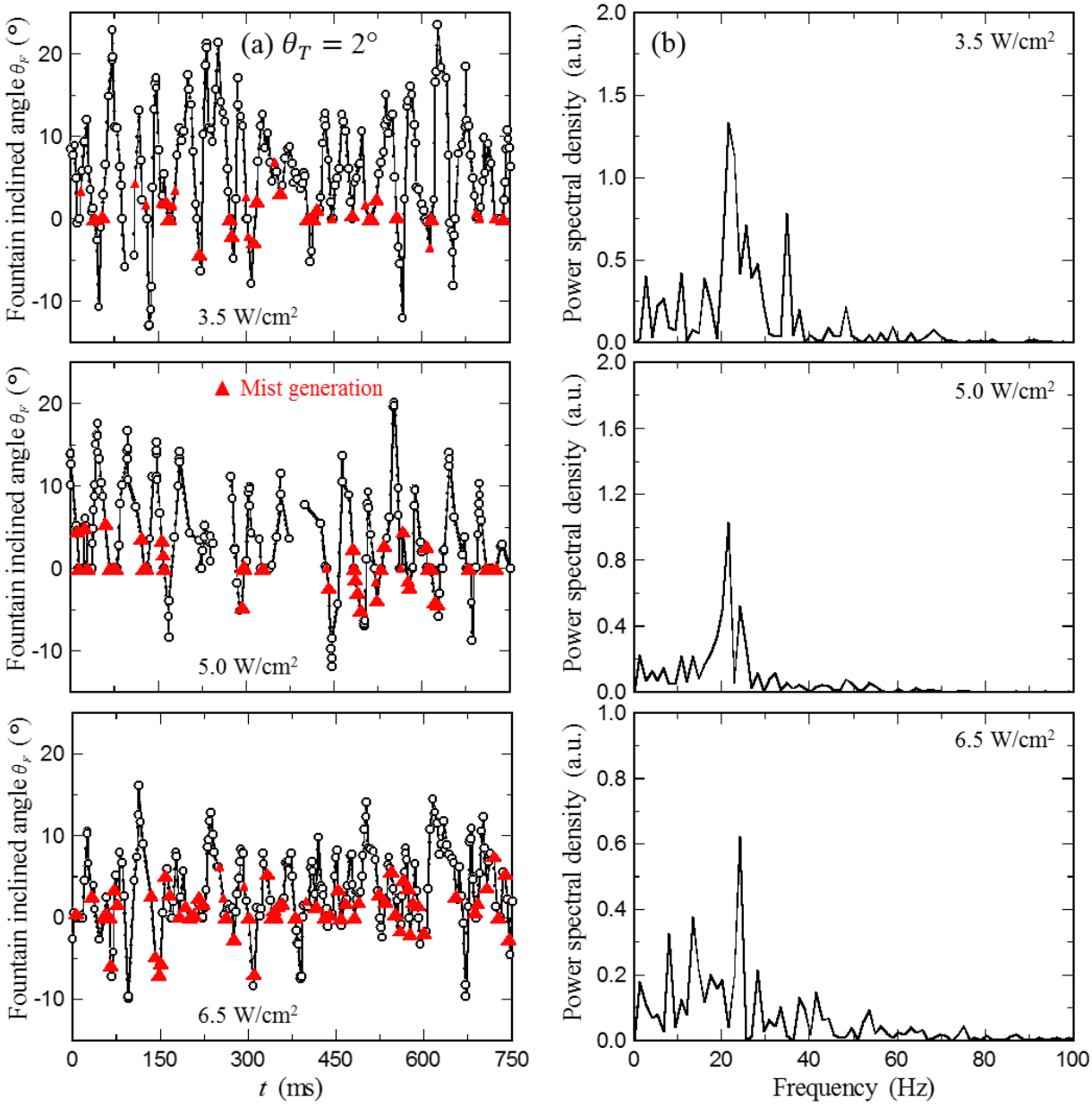

Figure 5.6 (a) Time variations in fountain inclined angle, associated with mist generation, for transducer setting angle of 2° at input power densities of 3.5, 5.0 and 6.5 W/cm^2; (b) Corresponding outcomes of FFT analysis for fluctuating inclined angle.

4) Under probably the most complex situation, the fountain will behave as a two-body entity which exhibits two "separate" swinging motions with two pivotal regions—one near the base of the FR and the other around the connecting region—resembling the so-called "double compound" pendulum (Huat *et al.*, 2004).

The second set of assumptions based on the time-series information (see Figs 5.5 and 5.6) can be proposed as follows:

5) The waveform of fountain-swinging, exhibited in Fig. 5.5(b), particularly demonstrates the periodicity of the fountain's lateral dynamics with a peculiar nature of *asymmetricity* on the positive side of the angle θ_F. This experimental trend of *skewness* signifies its frequency would be *twice* as high as an assumed symmetric (*i.e.*, regular sinusoidal—given by the red, dashed smooth) waveform (cf. Alexander, 2003; van Bijlert *et al.*, 2021);
6) The axial growth–breakup time-series data, on the other hand, with frequencies as high as 5–8 times that of the lateral will lead to the assumed representation of time-invariant fountain height throughout the oscillations.

The third set of assumptions/simplifications would be needed for further idealization to mathematically express the prescribed pendulum system with realistic complexity reflecting the limited parametric information available, which could be added as follows:

7) The "tension-like" force(s) required to sustain the pendulum straight in the direction of its axis on the equilibrium position—specified by a prescribed angle—should be the acoustic strength, or acoustic radiation pressure/force(s) (denoted by F_{AR}), which could be balanced by the gravitational contribution ($m_F g$) where m_F is the apparent mass of the pendulum (*i.e.*, fountain) as a whole;
8) The fountain, modeled by a dual-compound pendulum, is assigned to have the lower body of cone-shape of mass m_1 (Body 1, spanning the FR and BSR) and the upper body of cylindrical-shape of mass m_2 (Body 2, spanning the FSSR);
9) Te two bodies thus simplified geometrically will rotate about their specific pivotal locations—Bodies 1 and 2 around Pivots 1 and 2, respectively—where Pivot 2 serves as the joint connecting the two bodies.

All these assumptions are depicted in **Figs 5.7** and **5.8** for more comprehensive definitions as well as specifications towards the intended mathematical formulation. In the following, essentially each assumption [out of ASM (1)−(9) with additional ones for further simplification] will be materialized into a series of model expressions/equations proposed—with the final expression for the model-evaluated frequency to be compared with the FFT-evaluated dominant frequency.

Visualized structure and dynamics "converted" into quantitative expressions (Figs 5.2, 5.3 and 5.7): The swinging fountain as a dual-part entity consists of one part rotating around the base center of the fountain FR (Pivot 1, P_1) with $\theta_F = \theta_{F1}$ (covering FR + BSR) and the other around the connecting region or point (Pivot 2, P_2) with $\theta_F = \theta_{F2}$ (FSSR), occasionally bent at Pivot 2 satisfying the relation $|\theta_{F1}| \leq |\theta_{F2}|$. The fountain will thus exhibit—as a double-compound pendulum—two separate (but mutually dependent/interactive) swinging motions characterized by the angular accelerations, $\frac{d^2\theta_{F1}}{dt^2}$ and $\frac{d^2\theta_{F2}}{dt^2}$, around Pivots 1 and 2, respectively [inferred from ASM (1), (3) and (4)].

Time-series characteristics "converted" into quantitative relationships (Figs 5.5, 5.6 and 5.7): The axial fluctuations of the fountain, being regarded as time-invariant, would lead to its total length (tilted into the apparent height) which is a sum of individual parts, *i.e.*, $L_F = L_1 + L_2 \neq f(t)$, while the lateral fluctuations are to be given by slower oscillations of asymmetric in nature, specified as

$$f_{\text{fount}} = 2f_{\text{pend}} \equiv 2f_F \tag{5.1}$$

[inferred from ASM (6) and (5), respectively].

Further simplifications "idealized" into model equations (Fig. 5.8): The UsA fountain exerted by the "acoustic radiation" force(s), F_{AR}, *tries* by itself to maintain its "axial" direction "equilibrated" with the gravity component, *i.e.*,

$$F_{AR} = m_F g \cos\theta_T \tag{5.2}$$

[inferred from ASM (2) and (7)]. As provided in the forces diagram (Fig. 5.8) of the conceptual double-compound pendulum (Fig. 5.7), this *axially equilibrated tension* force F_{AR} plays an important role in contributing as the *restoring* force, the extent of which could be expressed as

$$F_{ARi} \equiv (1 - \beta_i)F_{AR} \quad (i = 1, 2) \tag{5.3}$$

for Bodies 1 and 2, respectively. Since these two contributions share the same direction as the fixed θ_T-directed tension F_{AR}, their instantaneous deviations—by θ_{F1} and θ_{F2}—from θ_T will cause the restoring effect as depicted in Fig. 5.8. While such deviations should result in energy dissipation—assumed to be represented by some assigned factors β_i's—where $\beta_1 \leq \beta_2$ due to the above stated condition $|\theta_{F1}| \leq |\theta_{F2}|$, it would be boldly presumed in this study that both the factors be much smaller than unity—having the *small-angle assumption* (to be stated below)—leading all together to $F_{AR1} \cong F_{AR2} \cong F_{AR}$.

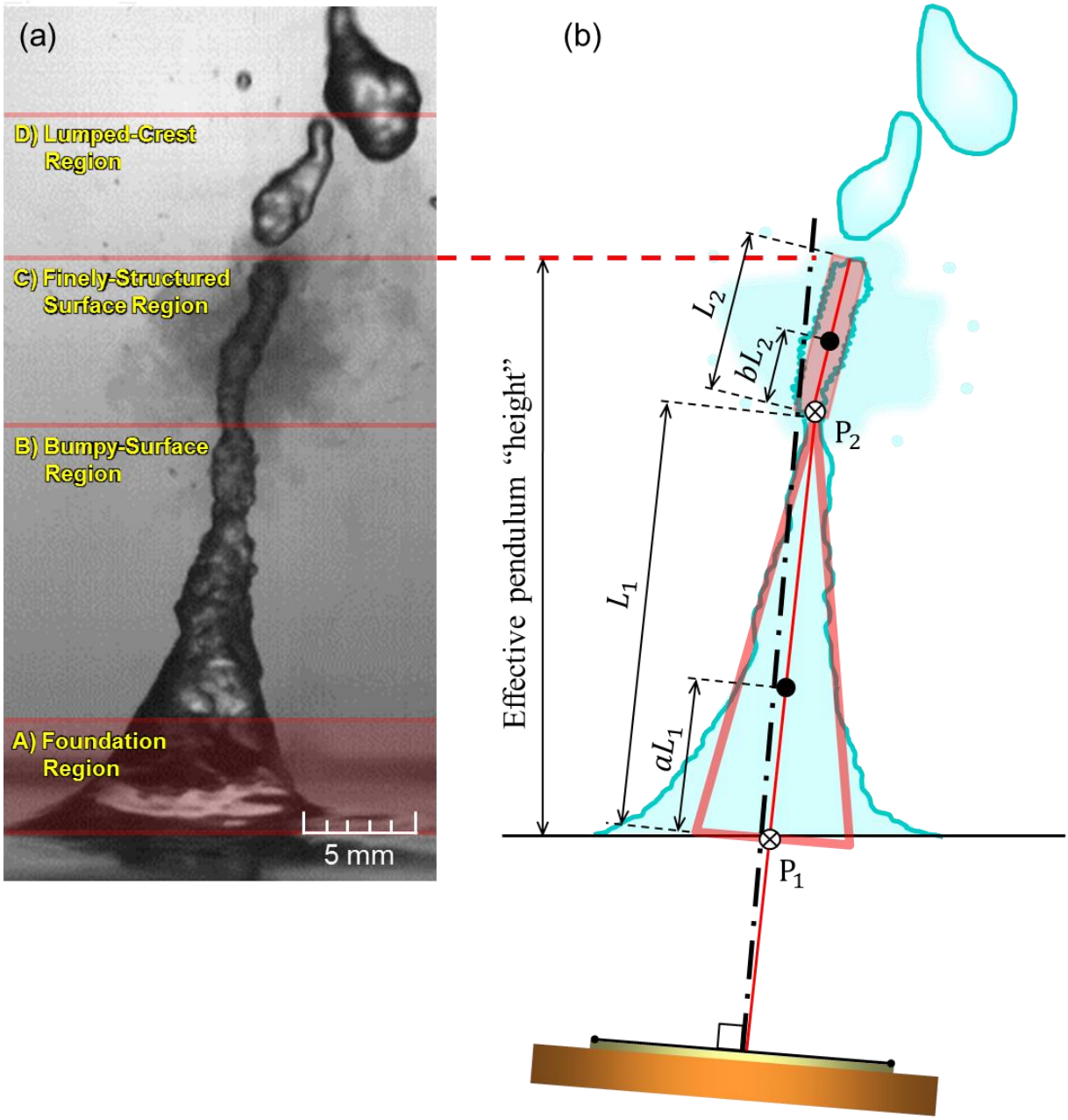

Figure 5.7 (a) General configuration of acoustic liquid fountain, proposed by Tsuchiya *et al.* (2011), based on dynamics of *four-region structure* realized on typical fountain image; (b) Schematic representation of comprehensive definitions as well as specifications towards swinging fountain model.

Based on the above series of simplifying arguments and the parameters specified in Figs 5.7 and 5.8, the balance in moments, or the angular equation of motion for θ_{F1}, about Pivot P_1, can be expressed as

$$I_{F1}\frac{d^2\theta_{F1}}{dt^2} = -F_{AR}L_1\sin\theta_{F1} + m_1gaL_1\sin(\theta_{F1}+\theta_T)$$
$$-fL_1\cos(\theta_{F1}+\theta_T) + m_2g\ L_1\sin(\theta_{F1}+\theta_T) \qquad (5.4)$$

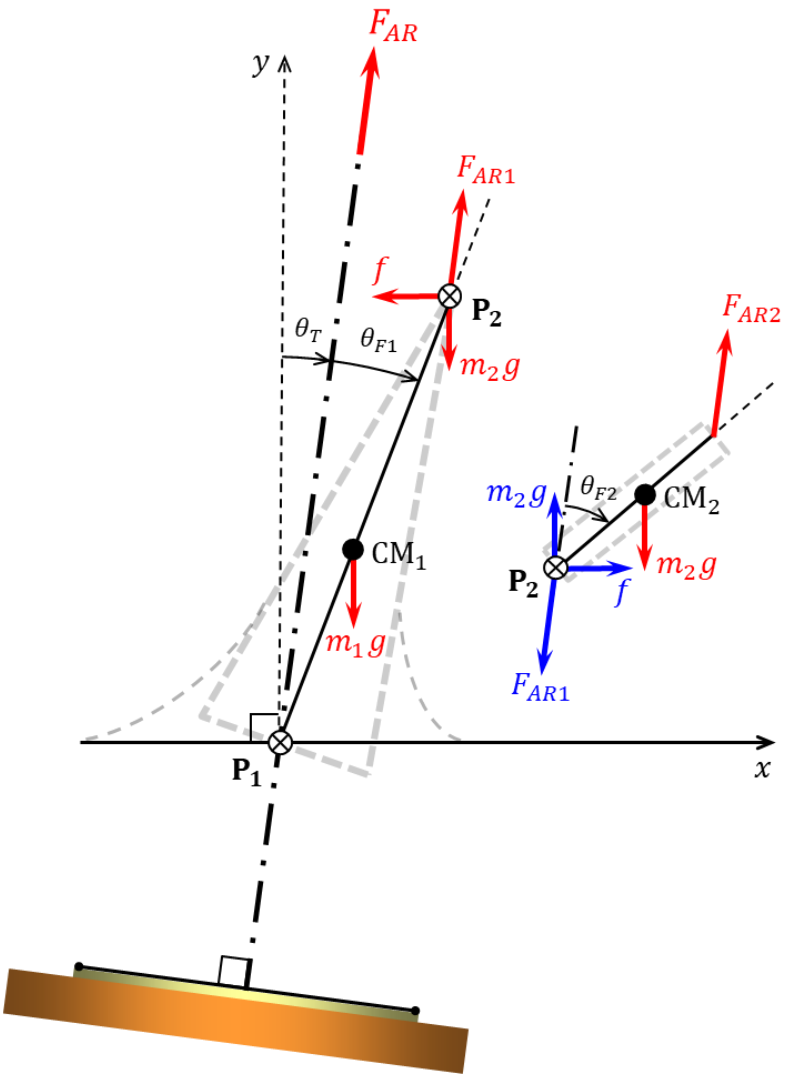

Figure 5.8 Forces diagram of conceptual double-compound pendulum inferred from modeled dual-part/body fountain depicted in Fig. 5.7.

Likewise, the balance in moments, *i.e.*, the angular equation of motion for θ_{F2}, about (not Pivot P_2 but) the center of mass CM_2 yields

$$I_2 \frac{d^2\theta_{F2}}{dt^2} = -F_{AR}(1-b)L_2 \sin\theta_{F2} + m_2 g b L_2 \sin(\theta_{F2}+\theta_T)$$
$$-F_{AR} \quad b\ L_2 \sin\theta_{F2} - f b L_2 \cos(\theta_{F2}+\theta_T) \qquad (5.5)$$

Here the mass moments of inertia for the respective bodies (Bodies 1 and 2) around their respective centers of mass (CM_1 and CM_2)—I_1 and I_2—will be specified by assigning their respective body geometries/shapes [ASM (1) and (8)]. The corresponding mass moments of inertia around Pivots P_1 and P_2 will be given respectively by

$$I_{F1} = I_1 + m_1(aL_1)^2 \text{ and } I_{F2} = I_2 + m_2(bL_2)^2$$

The set of equations above, Eqs (5.4) and (5.5), are to be rearranged—through the hori-

zontal action–reaction pair of forces having the same magnitude f on one hand—under the *small-angle approximation* of oscillations, *i.e.*, $\sin\phi \cong \phi$ and $\cos\phi \cong 1$ with ϕ being θ_{F1}, θ_{F2}, $\theta_{F1}+\theta_T$ or $\theta_{F2}+\theta_T$ to get a corresponding set of linear[ized] 2nd-order differential equations:

$$\begin{aligned} -f &= \frac{I_{F1}}{L_1}\frac{d^2\theta_{F1}}{dt^2} + F_{AR}\theta_{F1} - (am_1+m_2)g(\theta_{F1}+\theta_T) \\ &= \frac{I_2}{bL_2}\frac{d^2\theta_{F2}}{dt^2} + \frac{1}{b}F_{AR}\theta_{F2} - m_2 g(\theta_{F2}+\theta_T) \end{aligned} \tag{5.6}$$

The force f to be eliminated, on the other hand, can be specified by the horizontal acceleration at CM_2 (α_2) or its corresponding displacement (x_2) via Newton's second law (Huat *et al.*, 2004):

$$f = m_2\alpha_2 = m_2\frac{d^2x_2}{dt^2} = m_2\left(L_1\frac{d^2\theta_{F1}}{dt^2} + bL_2\frac{d^2\theta_{F2}}{dt^2}\right) \tag{5.7}$$

Eqs (5.6) and (5.7) are combined to remove f and, representing the 2nd derivatives in terms of the differential operator $(\mathbb{D} \equiv d/dt)$ will yield the following coupled 2nd-order differential equations in a matrix form:

$$\begin{bmatrix} \left(\frac{I_{F1}}{L_1}+m_2L_1\right)\mathbb{D}^2 + [F_{AR}-(am_1+m_2)g] & m_2bL_2\mathbb{D}^2 \\ m_2L_1\mathbb{D}^2 & \frac{I_{F2}}{bL_2}\mathbb{D}^2 + \left(\frac{1}{b}F_{AR}-m_2g\right) \end{bmatrix}\begin{bmatrix}\theta_{F1}\\ \theta_{F2}\end{bmatrix} = \begin{bmatrix}(am_1+m_2)g\\ m_2\ g\end{bmatrix}\theta_T \tag{5.8}$$

In the present study, this set of differential equations will not be attempted to be solved any further for two different oscillation angles, θ_{F1} and θ_{F2}; rather, another bold presumption would be made to have

$$\theta_{F1} \simeq \theta_{F2} \equiv \theta_F$$

viz., the dual-body pendulum would be reduced to a single-pendulum model.

The resulting model system of swinging fountain represented by such a simple pendulum would then be expressed mathematically as

$$I_F\frac{d^2\theta_F}{dt^2} + \left(F_{AR}L_F - m_FL_F^{\mathrm{CM}}g\right)\theta_F = m_FL_F^{\mathrm{CM}}g\theta_T \tag{5.9}$$

This is essentially a 2nd-order differential equation for a simple harmonic oscillation, which can be solved for the system angular frequency ω_F—with the *gravity-equilibrated* F_{AR} given by Eq. (5.2) and the *small-angle approximation* for θ_T, *i.e.*, $\cos\theta_T \cong 1$—to yield the *natural*

frequency of [harmonic] oscillation:

$$\omega_F^2 \equiv (2\pi f_F)^2 = \frac{m_F\left(L_F - L_F^{\mathrm{CM}}\right)g}{I_F} \tag{5.10}$$

which signifies the ratio of the torque imposed by gravity on the mass of the pendulum to the resistance to acceleration defined by the moment of inertia. The swinging frequency of the acoustic fountain in this study is then specified via Eq. (5.1) as

$$f_{\mathrm{fount}} = 2f_{\mathrm{pend}}(\equiv 2f_F) = \frac{1}{\pi}\sqrt{\frac{m_F\left(L_F - L_F^{\mathrm{CM}}\right)g}{I_F}} \tag{5.11}$$

In this rather general expression, each parameter on the right-hand side could be provided as follow:

- ▻ The total mass moment of the fountain consisting of Bodies 1 and 2, the geometries of which are respectively a cone of the base radius R_1 and the height L_1, and a cylinder of the radius R_2 and the height L_2:

$$\begin{aligned} I_F &= I_1 + m_1(aL_1)^2 + I_2 + m_2(L_1 + bL_2)^2 \\ &= m_1\left(\frac{3}{10}R_1^2 + \frac{1}{9}L_1^2\right) + m_2\left(\frac{1}{2}R_2^2 + L_1^2 + L_1L_2 + \frac{1}{4}L_2^2\right) \end{aligned} \tag{5.11a}$$

- ▻ The total mass itself of the fountain:

$$m_F = m_1 + m_2 = \rho_L\pi\left(\frac{1}{3}R_1^2L_1 + R_2^2L_2\right) \tag{5.11b}$$

- ▻ The apparent center of mass for the fountain as a whole (L_F^{CM}) as well as the fountain length itself (L_F) combined as

$$L_F - L_F^{\mathrm{CM}} = \frac{m_1[(1-a)L_1 + L_2]g \; + \; m_2(1-b)L_2g}{m_1 + \; m_2}$$

or

$$m_F\left(L_F - L_F^{\mathrm{CM}}\right) = \left(\frac{2}{3}L_1 + L_2\right)m_1g + \frac{1}{2}L_2m_2g \tag{5.11c}$$

Comparison(s) of the model-evaluated frequency $2f_F$ range—along with specific/representative values of the model parameters, determined based on the images obtained in this study—with the experimentally found (FFT-evaluated, dominant) frequency are summarized in **Table 5.1**. Reasonable agreement between these values appear to be obtained.

Table 5.1 Comparison of model-predicted and FFT-evaluated values for fountain-swinging frequency

Input power (W/cm^2)	L_1 (mm)	L_2 (mm)	R_1 (mm)	R_2 (mm)	$10^4 m_1$ (kg)	$10^5 m_2$ (kg)	$10^{10} I_1$ (kg m^2)	$10^{11} I_2$ (kg m^2)	Pred [Eq. (4)] $2f_F$ (Hz)	Exp (FFT) Main freq. (Hz)
3.5 @2°	10.8	4.8	2.9	0.8	0.95	0.96	2.4	0.31	19.1–21.5	21
5.0 @2°	16.6	5.2	3.5	1.0	2.10	1.60	7.7	0.81	16.2–17.9	21
5.0 @5°	14.7	6.2	3.1	0.7	1.50	0.95	4.3	0.23	18.4–19.0	18
6.5 @2°	18.5	8.2	3.0	1.0	1.70	2.60	4.6	1.30	13.4–17.3	24

As inferred from the above modeling outcome, the (asymmetric) fountain swinging observed in this study is of a resonant nature—*i.e.*, occurring at or (if not completely undamped, or $\beta_i \neq 0$) near the natural frequency of the fountain as a whole. In dimensionless form, it can be expressed in terms of the resonance Strouhal number (Sr) based on the resonance frequency f_{fount} (or f_F in view of purely modeling perspective) together with some characteristic length and velocity. The latter two characteristics are selected in this study to be the basal diameter of the fountain, d_{base} ($= 2R_1$), and the propagation velocity of a capillary waveform (Fan and Tsuchiya, 1990) or the so-called capillary–inertial velocity (Liu *et al.*, 2014) along the acoustic fountain surface. Such a specification will lead to the Strouhal number defined by

$$Sr_F = \frac{f_F\, d_{\text{base}}}{\sqrt{2\sigma/\rho_l d_{\text{base}}}} = \frac{f_F\, l_c}{\sqrt{2\sigma/\rho_l l_c}} \left(\frac{d_{\text{base}}}{l_c}\right)^{\frac{3}{2}} \tag{5.12}$$

Note in this equation that the capillary length l_c defined by

$$l_c = \sqrt{\sigma/\rho_l g} \tag{5.13}$$

is explicitly introduced into the expression, along with the reduced basal diameter.

Further evaluation of the current model performance in providing the dominant frequency of the laterally oscillating liquid acoustic fountain in the air—besides comparing it with the FFT-evaluated values—is attempted in terms of thus defined Strouhal number. To do so, a well-accepted convention, in multiphase fluid mechanics area, of plotting this dimensionless number against the Reynolds number (Re) is adopted in the present study; specifically utilized is a simple relationship/correlation proposed by Fan and Tsuchiya (1990)—and well-supported by, *e.g.*, Sankaranarayanan *et al.* (2002)—given by the following form:

$$\frac{Sr}{Sr_0} = \left(1 - \frac{Ta_0}{Ta}\right)^2 \tag{5.14}$$

where Ta is the Tadaki number defined by $Ta \equiv Re\, Mo^{0.23}$ with $Re \equiv d_{\text{base}}\sqrt{2\sigma/\rho_l d_{\text{base}}}/(\mu_l/\rho_l)$—in this particular phenomenon of UsA fountain oscillations—and the Morton number which depends only on the liquid properties, $Mo \equiv \mu_l^4 g/(\sigma^3 \rho_l)$. The two correlative parameters, Sr_0 and Ta_0, are system-specific.

Figure 5.9 depicts, first of all, the present results for estimated values of the resonance Sr_F, obtained based on the above idealized model as well as the FFT-supported values of $Sr_{\text{fount}} = 2Sr_{\text{pend}}$ ($\equiv 2Sr_F$), each in four data points. To be compared with this liquid fountain "pendulum" is a single (gas) bubble associated with its wake—more specifically, the *primary wake* closely following the (zigzag) rising bubble in a stationary liquid—or their combined entity, "bubble–wake pendulum" exhibiting a similar oscillating/rocking motion (Tsuchiya and Fan, 1988; Fan and Tsuchiya, 1990). The figure includes some selected data (seven) points along with the specifically "tuned" correlation—linear in the given coordinates—of such a gas (dispersed)–liquid system (Fan and Tsuchiya, 1990). It should be noted that both the pendulum systems compare reasonably well with each other in terms of not only the linearly increasing trend but also the range of ordinate ($Ta\, Sr^{1/2}$) values—an encouraging outcome.

Also shown in Fig. 5.9 are: the acoustic liquid fountain consisting of a chain of beads/drops in contact, or the corrugated jet of liquid, studied specifically in Chapter 4, which exhibits characteristic oscillations in individual beads shape; and fixed solid spheres exhibiting the surrounding fluid (gas or liquid) oscillations, known as vortex shedding behind the sphere (or in its wake), some data of which are selected from the compilation presented by Fan and Tsuchiya (1990) in their Fig. 4.8. The former involves two modes of shape oscillations—assigned by n, the order corresponding to the representative shape of an oscillating drop (here, its vertical cross section being an ellipse: $n = 2$, and a diamond: $n = 4$; Chapter 4). While not the same type of oscillations—*pendulum swinging* vs. *shape fluctuations*—their frequencies in terms of $Ta\, Sr^{1/2}$ demonstrate a similar range as well as trend. The latter falls essentially in the same range as well, despite—again—the different type of (*surrounding flow*) *oscillations*. The fact that all these comparisons (see **Table 5.2** for a detailed list of the relevant data sets selected) apparently lead to the similar trend and range in the dimensionless frequency signifies that the relationship between Re and Sr, or more specifically, the linear

relationship between Ta and $Ta\ Sr^{1/2}$ should provide quite a robust predictive scheme for a variety of *resonance* frequencies.

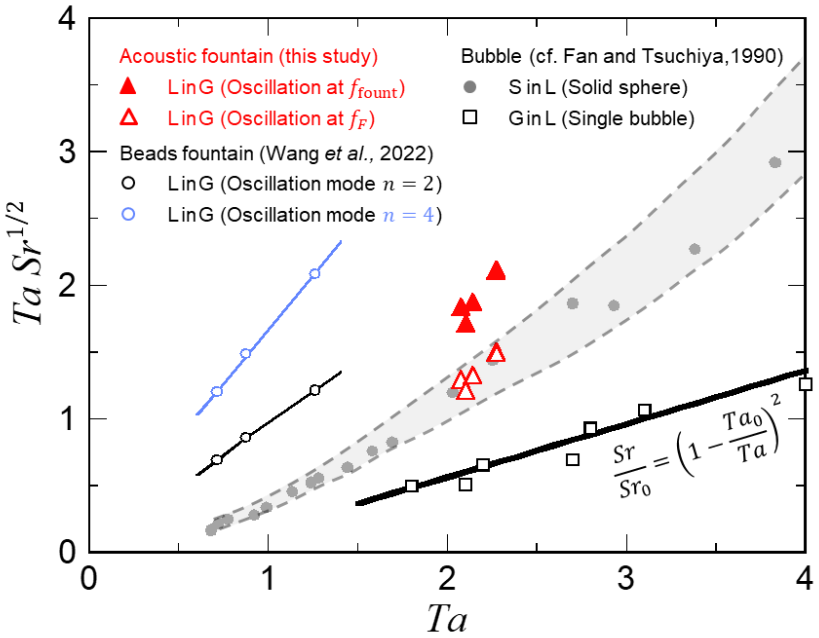

Figure 5.9 Resonance frequencies of various pendulum-like (or rocking), shape-deforming and disturbed surrounding-flow oscillations represented by dimensionless form correlatable via a simple expression proposed by Fan and Tsuchiya (1990).

Table 5.2 Comparison of model-predicted Strouhal numbers in different aspects of oscillating phenomena of UsA fountain

Liquid fountain (W/cm²)	d_{base} (mm)	f_{fount} (Hz)	f_F (Hz)	U_{capil} (m/s)	Re_{fount}	Sr_F	Sr_{fount}	Ta_{fount}	$Ta\ Sr_F^{1/2}$	$Ta\ Sr_{fount}^{1/2}$
3.5 @2°	2.9	21.5	10.7	0.16	1030	0.39	0.79	2.07	1.30	1.84
5.0 @2°	3.5	17.9	9.0	0.14	1130	0.44	0.87	2.27	1.50	2.12
5.0 @5°	3.1	19.0	9.5	0.15	1060	0.39	0.77	2.14	1.33	1.88
6.5 @2°	3.0	17.3	8.7	0.16	1040	0.34	0.67	2.10	1.22	1.72
Beads fountain (MHz)	d_{bead} (mm)	f_2 (kHz)	f_4 (kHz)	U_{capil} (m/s)	Re_{bead}	Sr_2	Sr_4	Ta_{bead}	$Ta\ Sr_2^{1/2}$	$Ta\ Sr_4^{1/2}$
1.0	1.47	0.13	0.38	0.21	114	0.92	2.68	1.28	1.22	2.09
2.0	0.74	0.36	1.08	0.29	81	0.91	2.72	0.91	0.86	1.49
3.0	0.49	0.66	1.99	0.36	66	0.90	2.70	0.74	0.70	1.21

5.4 Concluding Remarks

For ultrasound irradiated out of the transducer used with its installation angles ranging 0°–6° or higher (up to 10° examined) and input power densities of 3.5–6.5 W/cm^2, the UsA fountain will exhibit a sequence of oscillating/intermittent features. Our main findings are summarized below:

A slight tilt in irradiation of ultrasound should be of advantages in both operational and mist-generating performances. The acoustic liquid fountain will become improved in its operability/stability by avoiding the disruption of oscillation rhythm of the fountain from vertically interacting tip-separated drops;

The atomization, or mist generation, is mostly—almost exclusively—triggered and enhanced as the *laterally* swinging fountain *comes across the direction of irradiation*, more specifically, with its inclined angle being shifted from positive to negative in the 0°±5° range. The degree of occurrence of mist generation and the amount of identifiable mist generated would decrease, associated with reduction in both the growth rate and breakup frequency of the fountain on the tilt;

In line with such *axial* extents of growth and breakup of the fountain, both taking maximum values at the transducer installation angle of 2°, its optimum value should be recommended to be slightly tilted 2° from the viewpoint of stability of the UsA fountain and not to exceed 5° from that of effective mist generation;

A mechanistic view of UsA process is provided in terms of the swinging periodicity of liquid fountain with mist generated intermittently, in particular, if the ultrasound is irradiated on the tilt—under the influence of gravity. The periodicity of both the axial and lateral oscillations has been quantified—the latter in particular being model-predicted based on a simple *planar pendulum* concept proposed, partly confirmed via FFT-evaluated dominant frequency.

References

Aikawa, T. and N. Kudo, "Relation between thresholds of free radical generation and atomization under ultrasound exposure," *Jpn. J. Appl. Phys.*, **60**, SDDD13 (2021). http://doi.org/10.35848/1347-4065/abf600.

Alexander, R.M., *Principles of Animal Locomotion*, Princeton University Press, Princeton, NJ

(2003). https://doi.org/10.1515/9781400849512. https://press.princeton.edu/books/paperback/9780691126340/principles-of-animal-locomotion.

Dalmoro, A., A. A. Barba and M. d'Amore, "Analysis of size correlations for microdroplets produced by ultrasonic atomization," *Sci. World J.*, **2013**, 482910 (2013). https://doi.org/10.1155/2013/482910.

Dong, Z., C. Yao, X. Zhang, J. Xu, G. Chen, Y. Zhao and Q. Yuan, "A high-power ultrasonic microreactor and its application in gas–liquid mass transfer intensification," *Lab Chip*, **15**, 1145–1152 (2015). https://doi.org/10.1039/c4lc01431f.

Fan, L.-S. and K. Tsuchiya, *Bubble Wake Dynamics in Liquids and Liquid–Solid Suspensions*, Butterworth–Heinemann, Stoneham, MA (1990). https://www.sciencedirect.com/book/9780409902860/bubble-wake-dynamics-in-liquids-and-liquid-solid-suspensions.

Fujita, K. and K. Tsuchiya, "Cavitating bubble inside liquid fountain of beads associated with ultrasonic atomization," *Proc. 8th Int. Conf. Multiphase Flow (ICMF 2013)*, Paper 863/1–5 (2013).

Hinman, J. G., J. J. Hinman, B. E. Janicek, P. Y. Huang, K. S. Suslick and C. J. Murphy, "Ultrasonic nebulization for TEM sample preparation on single-layer graphene grids," *Nano Lett.*, **19**, 1938–1943 (2019). http://doi.org/10.1021/acs.nanolett.8b05117.

Huat, O. J., D. N. Ghista, N. K. Beng and T. C. C. John, "Optimal stride frequency computed from the double-compound pendulum of the leg, and verified experimentally as the preferred stride frequency of jogging," *Int. J. Comput. Appl. Technol.*, **21**, 46–51 (2004). https://doi.org/10.1504/IJCAT.2004.005338.

Kaur, J., R. R. Singh, E. Khan, A. Kumar and A. Joshi, "Piperine-loaded PLGA nanoparticles as cancer drug carriers," *ACS Appl. Nano Mater.*, **4**, 14197–14207 (2021). https://doi.org/10.1021/acsanm.1c03664.

Kawase, Y., T. Masuya, K. Yasuda and M. Nakamura, "Effects of flow mode of carrier gas on performance of ultrasonic atomization," *J. Chem. Eng. Jpn.*, **39**, 842–845 (2006). https://doi.org/10.1252/jcej.39.842.

Kim, G., S. Cheng, L. Hong, J.-T. Kim, K. C. Li and L. P. Chamorro, "On the acoustic fountain types and flow induced with focused ultrasound," *J. Fluid Mech.*, **909**, R2 (2021).

http://doi.org/10.1017/jfm.2020.1012.

Kim, H., J. Lee and Y.-Y. Won, "A simple derivation of the critical condition for the ultrasonic atomization of polymer solutions," *Ultrason.*, **61**, 20–24 (2015). https://doi.org/10.1016/j.ultras.2015.04.007.

Kirpalani, D.M. and K. Suzuki, "Ethanol enrichment from ethanol–water mixtures using high frequency ultrasonic atomization," *Ultrason. Sonochem.*, **18**, 1012–1017 (2011). http://doi.org/10.1016/j.ultsonch.2010.05.013.

Kobara, H., M. Tamiya, A. Wakisaka, T. Fukazu and K. Matsuura, "Relationship between the size of mist droplets and ethanol condensation efficiency at ultrasonic atomization on ethanol–water mixtures," *AIChE J.*, **56**, 810–814 (2010). https://doi.org/10.1002/aic.12008.

Kooij, S., A. Astefanei, G.L. Corthals and D. Bonn, "Size distributions of droplets produced by ultrasonic nebulizers," *Sci. Rep.*, **9**, 6128 (2019). https://doi.org/10.1038/s41598-019-42599-8.

Kudo, T., K. Sekiguchi, K. Sankoda, N. Namiki and S. Nii, "Effect of ultrasonic frequency on size distributions of nanosized mist generated by ultrasonic atomization," *Ultrason. Sonochem.*, **37**, 16–22 (2017). https://doi.org/10.1016/j.ultsonch.2016.12.019.

Kunde, G.B. and B. Sehgal, "Application of sol-gel assisted ultrasound-induced atomization in the mesostructuring of nickel aluminate UF membranes," *Microporous Mesoporous Mater.*, **325**, 111299 (2021). https://doi.org/10.1016/j.micromeso.2021.111299.

Lee, J., K. Yasui, T. Tuziuti, T. Kozuka, A. Towata and Y. Iida, "Spatial distribution enhancement of sonoluminescence activity by altering sonication and solution conditions," *J. Phys. Chem. B*, **112**, 15333–15341 (2008). https://doi.org/10.1021/jp8060224.

Lee, J., M. Ashokkumar, K. Yasui, T. Tuziuti, T. Kozuka, A. Towata and Y. Iida, "Development and optimization of acoustic bubble structures at high frequencies," *Ultrason. Sonochem.*, **18**, 92–98 (2011). https://doi.org/10.1016/j.ultsonch.2010.03.004.

Liu, F., G. Ghigliotti, J.J. Feng and C.-H. Chen, "Numerical simulations of self-propelled jumping upon drop coalescence on non-wetting surfaces," *J. Fluid Mech.*, **752**, 39–65 (2014). https://doi.org/10.1017/jfm.2014.320.

Mahamuni, N.N. and Y.G. Adewuyi, "Advanced oxidation processes (AOPs) involving

ultrasound for waste water treatment: A review with emphasis on cost estimation," *Ultrason. Sonochem.*, **17**, 990–1003 (2010). https://doi.org/10.1016/j.ultsonch.2009.09.005.

Mai, N.L., Y.-M. Koo and S.H. Ha, "Separation characteristics of hydrophilic ionic liquids from ionic liquids-water solution by ultrasonic atomization," *Ultrason. Sonochem.*, **53**, 187–191 (2019). http://doi.org/10.1016/j.ultsonch.2019.01.004.

Marjanian, M.M., S. Shahhosseini and A. Ansari, "Investigation of the ultrasound assisted CO_2 absorption using different absorbents," *Process Saf. Environ. Prot.*, **149**, 277–288 (2021). https://doi.org/10.1016/j.psep.2020.10.054.

Matsuura, K., M. Kobayashi, M. Hirotsune, M. Sato, H. Sasaki and K. Shimizu, "New separation technique under normal temperature and pressure using an ultrasonic atomization," *Jpn Soc. Chem. Eng. Symp. Ser.*, **46**, 44–49 (1995).

Nii, S. and N. Oka, "Size-selective separation of submicron particles in suspensions with ultrasonic atomization," *Ultrason. Sonochem.*, **21**, 2032–2036 (2014). http://doi.org/10.1016/j.ultsonch.2014.03.033.

Orisaki, M. and T. Kajishima, "Numerical analysis of water surface rising caused by underwater ultrasonic wave," *Trans. JSME* (in Japanese), **88**, 21-00377 (2022). https://doi.org/10.1299/transjsme.21-00377.

Panão, M., "Ultrasonic atomization: new spray characterization approaches," *Fluids*, **7**, 29 (2022). https://doi.org/10.3390/fluids7010029.

Sankaranarayanan, K., X. Shan, I.G. Kevrekidis and S. Sundaresan, "Analysis of drag and virtual mass forces in bubbly suspensions using an implicit formulation of the lattice Boltzmann method," *J. Fluid Mech.*, **452**, 61–96 (2002). https://doi.org/10.1017/S0022112001006619.

Sato, M., K. Matsuura and T. Fujii, "Ethanol separation from ethanol–water solution by ultrasonic atomization and its proposed mechanism based on parametric decay instability of capillary wave," *J. Chem. Phys.*, **114**, 2382–2386 (2001). https://doi.org/10.1063/1.1336842.

Simon, J.C., O.A. Sapozhnikov, V.A. Khokhlova, L.A. Crum and M.R. Bailey, "Ultrasonic atomization of liquids in drop-chain acoustic fountains," *J. Fluid Mech.*, **766**, 129–146 (2015). https://doi.org/10.1017/jfm.2015.11.

Son, Y., M. Lim, M. Ashokkumar and J. Khim, "Geometric optimization of sonoreactors for the enhancement of sonochemical activity," *J. Phys. Chem. C*, **115**, 4096–4103 (2011). https://doi.org/10.1021/jp110319y.

Tamidi, A.M., K.K. Lau and S.H. Khalit, "A review of recent development in numerical simulation of ultrasonic-assisted gas-liquid mass transfer process," *Comput. Chem. Eng.*, **155**, 107498 (2021). https://doi.org/10.1016/j.compchemeng.2021.107498.

Tay, W.H., K.K. Lau and A.M. Shariff, "High frequency ultrasonic-assisted CO_2 absorption in a high pressure water batch system," *Ultrason. Sonochem.*, **33**, 190–196 (2016). https://doi.org/10.1016/j.ultsonch.2016.04.004.

Tay, W.H., K.K. Lau and A.M. Shariff, "High performance promoter-free CO_2 absorption using potassium carbonate solution in an ultrasonic irradiation system," *J. CO_2 Util.*, **21**, 383–394 (2017). https://doi.org/10.1016/j.jcou.2017.08.003.

Tsuchiya, K. and L.-S. Fan, "Prediction of the wake size of a single gas bubble in liquid and/or liquid–solid media—the pendulum model," *Chem. Eng. Sci.*, **43**, 2893–2897 (1988). https://doi.org/10.1016/0009-2509(88)80033-2.

Tsuchiya, K., H. Hayashi, K. Fujiwara and K. Matsuura, "Visual analysis of ultrasonic atomization and its associated phenomena," *Earozoru Kenkyu* (*J. Aerosol Res.* in Japanese), **26**, 11–17 (2011). https://doi.org/10.11203/jar.26.11.

van Bijlert, P.A., A.J.K. van Soest and A.S. Schulp, "Natural frequency method: estimating the preferred walking speed of tyrannosaurus rex based on tail natural frequency," *R. Soc. Open Sci.*, **8**, 201441 (2021). https://doi.org/10.1098/rsos.201441.

Wei, J., J. Gu, J. Guo, W. Li, C. Wang and J. Zhang, "Simultaneous removal of nitrogen oxides and sulfur dioxide using ultrasonically atomized hydrogen peroxide," *Environ. Sci. Pollut. Res.*, **26**, 22351–22361 (2019). https://doi.org/10.1007/s11356-019-05531-1.

Xu, Z., K. Yasuda and X. Liu, "Simulation of the formation and characteristics of ultrasonic fountain," *Ultrason. Sonochem.*, **32**, 241–246 (2016). http://doi.org/10.1016/j.ultsonch.2016.03.016.

Yasuda, K., H. Honma, Z. Xu, Y. Asakura, and S. Koda, "Ultrasonic atomization amount for different frequencies," *Jpn. J. Appl. Phys.*, **50**, 07HE23 (2011). https://doi.org/10.1143/JJAP.50.07HE23.

Chapter 6

Ultrasonic atomization—from onset of protruding free surface to emanating beads fountain—leading to mist spreading

6.1 Introduction

Ultrasonic atomization (UsA), as a means of generating rather uniform distribution of a swarm of small droplets, or mist, requires the prior formation of a fountain or jet of liquid having developed out of initially induced protrusion of the free surface (Tsuchiya *et al.*, 2011).

Various aspects of the UsA in its fundamental nature have been described in the literature: the droplet size distribution (DSD) of emerging mist (*e.g.*, Kobara *et al.*, 2010; Sekiguchi *et al.*, 2010; Kudo *et al.*, 2017); the selective separation/concentration of solute (or "targeted" suspension) into the mist with its extent and mechanisms (*e.g.*, Sato *et al.*, 2001; Nii and Oka, 2014); the structure and dynamics of the (general) liquid fountain observed visually (*e.g.*, Tsuchiya *et al.*, 2011); more extensive visual elucidation of the beads-structured fountain associated with internal cavity and/or (external) droplets bursting (Fujita and Tsuchiya, 2013; Tomita, 2014; Simon *et al.*, 2012, 2015); and the periodic nature or some dominant frequencies of the fountain-beads (or ideal cases of isolated-drops) oscillations (Shen *et al.*, 2010; Bouwhuis *et al.*, 2013; Watanabe *et al.*, 2018).

Among these aspects listed above, the UsA's structural aspect is of the primary concern here; more specifically, it is the present study's intent to focus on *four* representative transitions/demarcations in the acoustic fountain structure and dynamics: 1) the *onset* of a protrusion on otherwise flat free surface; 2) the *appearance* of undulation along the growing protuberance; 3) the *triggering* of emanating beads fountain out of this foundation-like region; and 4) the *induction* of droplets bursting and/or mist spreading. Prior to providing the relevant literature findings specific to each transitional "state/phase," the UsA mechanisms—*i.e.*, how the mist generation would occur in association with selective separation into the mist—are reviewed first.

In the literature, selective separation of solute or suspended particles (or surfactants) from a solution—probably the most important scientific impact recognized for the UsA—has been claimed to be attained through two possible mechanisms proposed: *capillary-wave* and *cavitation* hypotheses. The former has been supported by, *e.g.*, Qi *et al.* (2008), Collins *et al.* (2012), and Blamey *et al.* (2013); the latter by, *e.g.*, Neppiras and Noltingk (1951), Kojima *et al.* (2010), Ramisetty *et al.* (2013), and Inui *et al.* (2021). Cavitation bubbles, if present, could contribute to such selective separation from a multicomponent system like alcohol–water solutions—in symbiosis with capillary instabilities—associated with UsA (*e.g.*, Kirpalani and Toll, 2002); other supportive references of this *conjunction hypothesis* include Boguslavskii and Eknadiosyants (1969), Rozenberg (1973), Barreras *et al.* (2002), Simon *et al.* (2012, 2015), Tomita (2014), and Zhang *et al.* (2020).

Surface oscillations occurring along a perturbed protrusion or a conical fountain/column of solution have been reported, with some visual evidence (Barreras *et al.*, 2002; Tsuchiya *et al.*, 2011), in regard to the formation of μm-size droplets—pinched off under parametric decay instability of *capillary waves of microscale* (Sato *et al.*, 2001). There has been, however, little direct (visual) evidence that links the mist formation to the occurrence/prevalence of *cavitating bubbles within the liquid fountain* (Fujita and Tsuchiya, 2013; Tomita, 2014; Simon *et al.*, 2015).

The first limited support for the presence of cavitation bubbles under sonication—or "active" bubbles of size usually too small to be individually imaged—comes from a long-time exposure of the sono[chemical] luminescence, *i.e.*, the extent of sonochemical activity signifying the cavitation yield (Lee *et al.*, 2008, 2011; Son *et al.*, 2011). Second, a few are available among those cavitation–sonochemistry studies that provide explicit evidence for the simultaneous occurrence of both the cavitation formation and the UsA mist emergence within and out of the liquid fountain, respectively (*e.g.*, Kojima *et al.*, 2010).

The following four "sub-sections" are to be described in terms of "stability of the liquid-surface protrusion" or its dynamic "structural variation" by specifying its controlling factors: *radiation* pressure (or *traveling* wave) field, *anti-resonant* pressure (or *standing* wave) field, induced flow field, and the factors' thresholds levels.

Protrusion on free surface: Simon *et al.* (2015) claimed that, for a *focused* ultrasound

wave, the *radiation force* from the wave will induce a protuberance, or "mound," on the surface. When the protuberance prevails, coherent interactions between the waves *incident on and reflected from* the *pressure-release* (*i.e.*, wave-absorbing) interface would result in the generation of numerous cavitation bubbles inside the protuberance. Deeper insights—spanning physicochemical as well as hydrodynamic aspects—into the involvement of cavitation in driving the UsA could be gained from the two competing mechanisms proposed for the liquid flow associated with the sonic-generated cavitation bubbles underneath a rather flat free surface—thus in the absence of the UsA liquid fountain: 1) acoustic *radiation pressure*/force, as above, in a *traveling*-wave field and 2) acoustic *streaming* in a *standing*-wave field (Lee *et al.*, 2008, 2011; Son *et al.*, 2011).

Lee *et al.* (2011), examining three different driving frequencies, 0.17, 0.45 and 0.73 MHz in particular, at a fixed input power of 20 W (1.1 W/cm^2), reported the following trends: at the lower frequency, a strong standing-wave field prevailed homogeneously along the near central, vertical axis above the transducer, especially at early stages of wave propagation; at the intermediate frequency, the attenuation of acoustic pressure amplitude became appreciable with an increase in the driving frequency, leading to the development of a traveling-wave field near the transducer in competition against the standing wave still prevailing near the free surface; at the higher frequency, the attenuation of the acoustic energy became so significant—developing an energy gradient in the direction of the propagating acoustic wave—that the dominant mechanism shifted, with increasing driving frequency, from the radiation pressure caused by the traveling wave to the acoustic streaming.

Orisaki and Kajishima (2022) conducted a direct numerical simulation of the very beginning phase of water surface rising/protruding under 0.5-MHz ultrasound irradiation. Depending on the rising rate of the water surface, its height-increasing process was divided into three phases/stages: increasing slightly, with acceleration and at constant speed. Separate explanations of the protruding mechanisms for the individual stages were provided: 1) The acoustic radiation pressure equals the acoustic kinetic energy density, resulting in a slight rise in the water surface; 2) As the region between the sound source and the free surface turns to *resonance*, the acoustic radiation pressure acting on the surface will increase significantly, causing the surface to rise rapidly. By entraining a fluid owing to rapid rising of water surface, acous-

tic streaming is induced towards the risen region; 3) Eventually, the water surface will shift to *non-resonance*, leading to the acoustic radiation pressure decreasing significantly. In this last phase, the velocity of the acoustic streaming towards the rising is reported to become nearly constant.

Stability of growing protuberance: Xu *et al.* (2016), in their numerical simulation to realize the shape and to quantify the height of the acoustic fountain under varying input pressure level, found that "the ultrasonic field between the transducer flat disk and the fountain surface was an anti-resonant pressure (*i.e.*, standing wave) field"; with this finding they claimed that the radiation pressure is a minimum, leading to the fountain surface tending to be stable. Regarding the geometry/structure of the fountain, however, it was limited to a mere precursory structure or mound-like fountain.

Likewise for still an essentially protuberant state of water fountain, Kim *et al.* (2021) investigated experimentally the mechanism controlling its stability. For better spatiotemporal control, such fountains were induced by *focused* ultrasound at two distinct frequencies of ultrasound, 0.55 and 1.1 MHz; particle image velocimetry (PIV) was used to determine "the induced flow field around the ultrasonic *focal spot*." By varying the pressure level of the transducers, they observed three different regimes, *viz.* weak, intermediate (stable) and highly forced (explosive) fountains, with their claim of the acoustic radiation force being the dominant driving force for the fountain formation.

Aikawa and Kudo (2021) reported the "relationship between thresholds of *free radical generation* and atomization," which should provide very useful insights into a demarcation in the structural variation of dynamic fountains to be examined in the present study. The former is closely related to (or an outcome of) the *cavitation collapsing* process; the latter to the shape transition of free surface from a protuberance to a fountain of aspect ratio greater than unity. They detected essentially the *identical threshold* level in the increased transducer driving voltage—or equivalently, input power density (of 2.5 W/cm^2)—for all these four [cavitation collapsing—free radical(s) generation—free-surface shape transition: from protuberance to "prolate" fountain—atomization] phenomena. Utilizing *focused* shadowgraphy, they further detected the *spotty-shaped high-intensity nodes*—originating from the pressure-release interface (Simon *et al.*, 2015) of shape resembling a parabolic mirror; its convergence effect would

promote the generation of cavitation bubbles inside the protuberance; the induction of cavitation promoted by such high-intensity nodes in turn could trigger the rapidly growing or "abruptly shape-transitioning" fountain that leads to the atomization.

Emergence of beads fountain: When the ultrasonic wave has sufficient intensity or acoustic radiation pressure to overcome some threshold limit, a beads fountain—a fountain consisting of a chain (sometimes limited to a doublet or triplet) of beads in contact—will emerge from the foundation-like region, often accompanied by bursting droplets (Fujita and Tsuchiya, 2013; Tomita, 2014; Simon *et al.*, 2012, 2015). Fujita and Tsuchiya (2013), applying ultrahigh-speed imaging (at 0.25 megaframes/s) with a set of parameters (a *flat* ultrasound of 2.4 MHz with 2.0 W/cm^2 intensity), managed to capture a series of evidential images of a cavity—comprised of either a single void/bubble or a tightly clustered cavitating bubbles—near the central interior of a fountain bead. As this cavity moved across laterally towards the gas–liquid interface, *droplet bursting* eventually occurred.

Tomita (2014), using a different type of transducer with *focused* ultrasound (of 1 MHz), provided visual evidence (at 50 kfps) for cavitation in the primary bead of a double-beads fountain/jet to identify the threshold conditions for surface elevation and jet breakup, accompanied by fine droplets (*i.e.*, sprayed mist) at the neck between the primary and secondary beads—claimed to occur due to the *collapse of capillary waves*. Simon *et al.* (2015) employed focused transducers as well (at 5–30 kfps), with ultrasound waves of *moderate focal* acoustic intensities [mostly up to several hundreds, but requiring at least 180, of W/cm^2—a minimum level for atomization to first appear—though inconsistently (Simon *et al.*, 2012)]. For the given ranges of ultrasonic frequencies (2.165 mainly, 1.04 and as low as 0.155 MHz) and liquid sound speeds (1.14–1.90 km/s), they reported that atomization was attained as the acoustic intensity exceeds a liquid-dependent threshold.

Droplets bursting and/or mist spreading: Specific to the structure and dynamics of acoustic fountains to be examined in this study, a typical fountain is no longer a mere protrusion, not stable and associated with mist spreading [out of the Finely-Structured Surface Region (FSSR)] as well as large drops and/or liquid ligaments formed as a result of tip breakup [the Lumped-Crest Region (LCR)] (Tsuchiya *et al.*, 2011).

Kojima *et al.* (2010) investigated, at a fixed driving frequency of 0.49 MHz for different

input powers of 5–50 W (≅ 0.25–2.5 W/cm^2), the patterns of liquid flow and the spatial distribution of acoustic pressure through a laser Doppler velocimetry (LDV) along with a laser-sheet imaging and through sonochemical luminescence, respectively. With increasing input power (> 1.5 W/cm^2), they demonstrated that a liquid fountain formed with appreciable atomization and that sonochemical luminescence was observable not only in the bulk liquid near the liquid surface but also in the fountain while ultrasonic atomization taking place.

Simon *et al.* (2015) reported a non-spherical (triangular) deformation of the fountain beads prior to atomization, demonstrating that cavitation bubbles are a significant driving force for atomization in beads fountains. In Chapter 4, the surface oscillations of beads fountain, before atomization set in, from ellipsoid- to diamond-shape and finally to a hexagonal were observed. We suggested that atomization concurs with the fountain periodicity with a limited extent of probability. In addition, a minimum driving frequency was roughly identified to be ≈0.8 MHz or higher; however, a systematic evaluation of this lower bound has not been given yet.

In the present study, high-speed, high-resolution visualization is utilized to identify the surface dynamics of different states of acoustic fountain—ranging from a mere protruding state to a mist-associated state of higher aspect ratio—over wider ranges of acoustic parameters (mainly, the excitation frequency and the input power density). The study involves three main objectives: to find the relevant acoustic thresholds for the demarcations in the structural variations of dynamic fountains; to quantify the periodicity of fountain fluctuations via experimental frequency analysis (fast Fourier transform); and to investigate the formation mechanisms associated with fountains and atomization.

6.2 Experimental

The experimental setup used for visualizing the UsA process is shown in **Fig. 6.1**. An ultrasonic transducer having a wide range of driving/excitation frequencies [KAIJO QT-011 with frequency shifting/tuning capability: f_{ex} = 0.43, adjustable between 0.60 and 0.95 (with an increment of 0.05), 1.0, 1.6, 2.0 and 3.0 MHz] was placed on the bottom of a square vessel with its dimensions 200×200×185(height) mm. The transducer element (an oscillating circular disk) was 20.0 mm in diameter, having an effective oscillating diameter of 16 mm. For selected runs, on top of the transducer's oscillating disk was installed directly a Teflon® nozzle with a conical hollow structure (inner diameter of 2 mm at the top)—to help stabilize the liquid column. The installation or setting angle of the ultrasonic transducer was fixed at 0° (*viz.*, the ultrasonic irradiation was directed vertically). The input power applied to the transducer was changed over 1–20 W (input power density examined then ranged I_0 = 0.5–10 W/cm^2, which is exclusively used in this study as an operating parameter).

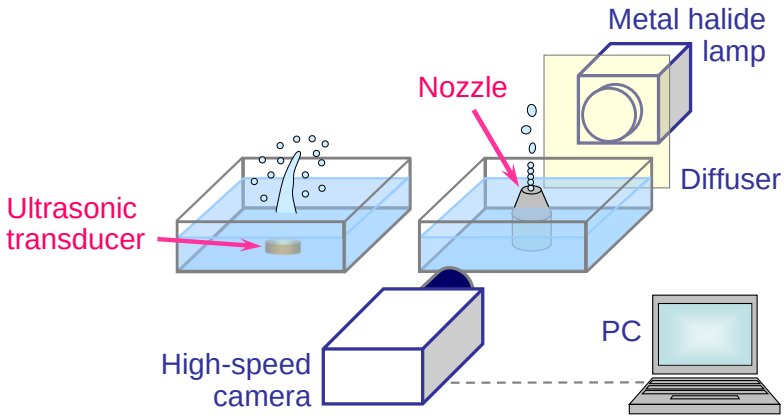

Figure 6.1 Schematic diagram of the experimental system for visual observation of ultrasonic atomization process in the absence/presence of a "regulating" nozzle equipped.

The distance from the center of the oscillator to the free surface of the solution (effective liquid depth) was kept 25 mm, or 32.5 mm above the vessel bottom. The liquid used was an aqueous ethanol solution with initial concentration of 50 wt% (28 mol%), temperature of which was set, before each run, to 25°C in a constant temperature bath. During the UsA over 10 seconds of operation at most, the bulk ethanol concentration is presumed not to vary, thus the liquid properties kept invariant.

6.2.1 High-speed visualization

High-speed imaging was made via a digital camera (Photron FASTCAM MINI AX100) attached with a macro-lens (Nikon Micro-Nikkor 105 mm f/2.8) to observe the dynamics of liquid protrusion or fountain and the associated phenomena, especially in detecting the ever-changing outline of the fountain surface and the onset position of droplet bursting. Each specific projection was captured—at frame rate(s) up to 5,000 fps, with a resolution of at least 512×512 pixels, and an exposure time as short as 197 μs—under backlighting using a metal halide lamp (Lighterrace MID-25FC). The imaging was started 5 s after the transducer was turned on, and a 0.2-s period of data were recorded. A sheet of light diffuser was installed between the liquid fountain and the lamp, thus reducing the non-uniformity of backlighting.

6.2.2 Image processing

Two types of image analyses were conducted: *dynamic tracking* (including time-series data) of the free-surface protrusion and *static outlining* (time-averaged, instantaneous shape) of the fountain beads. The former (see Section 6.3.1 for the resulting outcome) was realized with an image analysis software (DITECT Dipp Motion) and the latter (see Section 6.3.2) with another software (DITECT Dipp Macro). In particular, for the details in a sequence of the procedures for image processing and data acquisition of the latter, refer to Section 4.2.2. The original images of the liquid surface (both the protrusion and the column) in the air were binarized; the threshold for the binarization was set at the brightness level of the "shadow" in the very vicinity of the gas–liquid interface. Filling in blank(s) then extracted the interface boundary/outline, confined by thinning it down to 1 pixel. A video analysis software (KEYENCE Movie Editor) was used to determine the shape of an ellipse representing each bead in contact along the liquid column; the lowest two beads above the bottom of the liquid column were regarded stable and equivalent (or representative) spherical diameters of the two were measured in each image; this "vertical" apparent/effective chord length is determined to be the characteristic size of the fountain beads—an average over 60 pieces of the relevant images (30 frames of images with two beads each) obtained under each experimental condition.

6.3 Results and Discussion

The UsA sequence of the initiating free-surface protuberance or "mound," the resulting liquid fountain, followed by its associated mist, observed under the present wide ranges of experimental conditions, is characterized and discussed in both static/time-averaged and dynamic natures, over specific ranges of driving frequencies as broad as $f_{ex} = 0.43–3.0$ MHz and input power densities, $I_0 = 0.5–10$ W/cm^2 (see Section 6.2). **Figure 6.2** shows typical images of the four states/phases signifying the transitions described in Section 6.1, along with the relevant acoustic conditions summarized in **Table 6.1**.

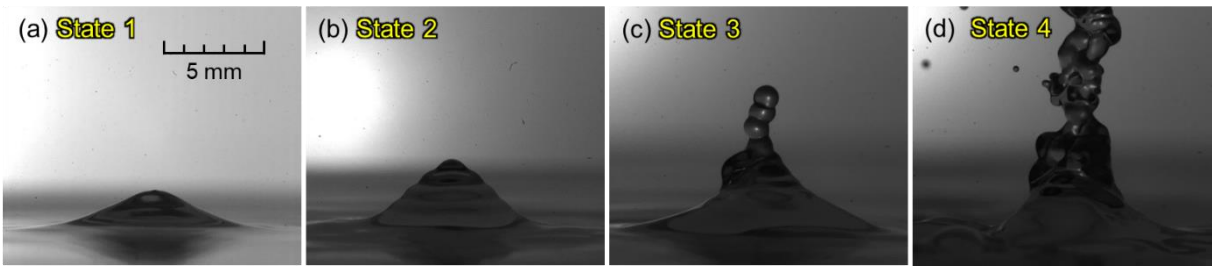

Figure 6.2 Typical images of four distinguishable transitional states at different input power densities for driving frequency of 3.0 MHz.

The first state has a shape of rather shallow, smooth mound kept stationary [see Fig. 6.2(a)] under the sets of acoustic conditions (driving frequencies and input power densities) as given (on the 1st and 2nd columns in Table 6.1). As the combination of these two parameters is properly adjusted (3rd column—vs. 1st—in Table 6.1), the protrusion becomes sharper with appearance of characteristic waves "dissecting" its surface; its shape as a whole still maintains the bell-like mound [Fig. 6.2(b)]. With the combination of the parameters in different settings (4th column as well as 1st in Table 6.1)—requiring a minimum/threshold driving frequency greater than 0.43 (as high as 0.80) MHz—a chain of liquid beads will emanate out of the mound [Fig. 6.2(c)]. As the minimum driving frequency is further raised, such a beads structure would be destabilized, exhibiting a complex structure [Fig. 6.2(d)]. A similar set of transitional states, reported (for water fountaining) by Kim *et al.* (2021) who applied *focused* ultrasound at two distinct frequencies, 0.55 and 1.1 MHz, were termed as weak, intermediate (stable) and highly forced (explosive) fountains (Section 6.1). The detailed description of each transition state is provided below in a separate section.

Table 6.1 Relevant acoustic conditions required for the four transition states

Driving frequency (MHz)	Input power density (W/cm^2)			
	State 1	State 2	State 3	State 4
0.43	6, 7, 8	9, 10	— [b]	— [b]
0.80	6, 7	8	9, 10	— [b]
1.0	— [a]	0.5	1, 1.5, 2	2.5
1.6	— [a]	0.5	1	1.5

[a] Not detected below the lowest operational limit (0.5 W/cm^2)

[b] Not detected above the highest operational limit (10 W/cm^2)

6.3.1 Free-surface protrusion and its growth

The geometric characterization of the bell-shaped mound of the liquid free surface can be made by tracing its outline, as shown in **Fig. 6.3**. As an outcome of the image processing described in Section 6.2.2, the interface boundary/outline extracted, by confining it down to 1 pixel, is provided, each for a specific combination of the two operating parameters: (a) for the lowest driving frequency of 0.43 MHz with varying (over a widest range of) input power density from the minimum of 6 W/cm^2—below which no appreciable protrusion was visually recognized in this study—to 10 W/cm^2; (b) for the proper combinations (listed in Table 6.1) to realize the second state [see Fig. 6.2(b)].

Geometric universality: An important finding to be stressed here [shown in Fig. 6.3(a)] is that—while the mound exhibits an essentially identical height as well as shape for the input power range of 6–8 W/cm^2—the height will increase *stepwise* as the power is raised from 8 to 9 W/cm^2 and again maintains the same *yet new* level at 9 and 10 W/cm^2. Similar observations, with quantitative evaluations of the steady-attained height of acoustic fountain, were made by Xu *et al.* (2016) numerically and Kim *et al.* (2021) experimentally, who both reported a step increment—with an increase in the acoustic pressure—of half the ultrasound wavelength. Such a stepwise transition from the 1st to 2nd state identified in this study would correspond to that from the weak to the stable fountain reported by Kim *et al.* (2021); this regime spanning the states of topologically identical geometries should be a crucial "stage" covering from the induction to the establishment of the Foundation Region (FR; Tsuchiya *et al.*, 2011) of the general configuration of the UsA fountain. It is to be added here that the bottom diameter, or

width, of the protrusion appears to be preserved, due probably to the driving frequency fixed at 0.43 MHz, *i.e.*, under the same *directivity* of ultrasound irradiated.

Another point to be noted in regard to the mound geometry is shown in Fig. 6.3(b): its outline for the 2nd state, *i.e.*, the being-established, rather steady/stable FR of the fountain, extracted via image processing, shares essentially the same "universal" shape and—more importantly—height for all the combinations of the two acoustic conditions as listed on the 1st and 3rd columns in Table 6.1. In this set of combinations, however, the width of protrusion differs slightly, depending on the driving frequency used; in general, the higher the frequency is, the narrower—with some exception—the width would be.

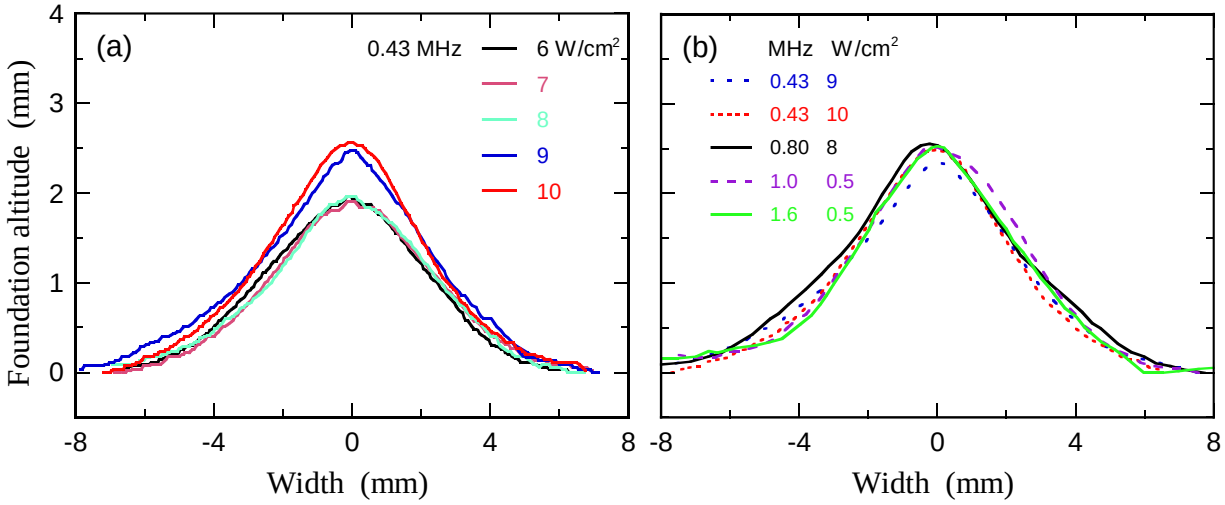

Figure 6.3 Effects of (a) input power densities, and (b) driving frequencies on the local altitude of liquid-fountain foundation.

Protrusion of concentric circles induced on free surface: As can be seen in Fig. 6.2(b), the mound will "grow"—become higher—with either increasing input power density (at a fixed driving frequency) or vice versa; this process is often observed to concur with the appearance of "regular undulation" (a series of concentric circles) superimposed on the general surface outline, some indication of which could be already recognizable at lower input powers in the 1st state. As claimed by Tsuchiya *et al.* (2011), who proposed that the vertical distance spanning each "local peak" of the undulation (undulation "pitch") should correspond to *half* the wavelength, a unique feature of such undulation lies in its *regularity* being controlled by the frequency—thus the *wavelength*—of the propagating ultrasound.

Figure 6.4 depicts such undulation along the mound surface observed at different driving frequencies. For the driving, or excitation, frequencies of $f_{ex} = 0.80$, 1.0 and 2.0 MHz, the undulation pitches are measured to be 0.90, 0.79 and 0.34 mm, respectively, corresponding to roughly *half* the ultrasonic wavelength. Note that the pertaining wavelengths ($\lambda_{wave} = v_{wave}/f_{ex}$—as excited) are estimated to be 1.84, 1.47 and 0.74 mm, respectively, where the sound speed v_{wave} of 1,470 m/s in 50-wt% ethanol aqueous solution at 25°C (Mijaković *et al.*, 2011) is employed, and also that Tsuchiya *et al.* (2011) used an ultrasound transducer (Honda Electronics HM-2412) with a driving frequency of 2.4 MHz to provide—though limited—the detected undulation having a vertical distance of 0.32 mm for each local peak.

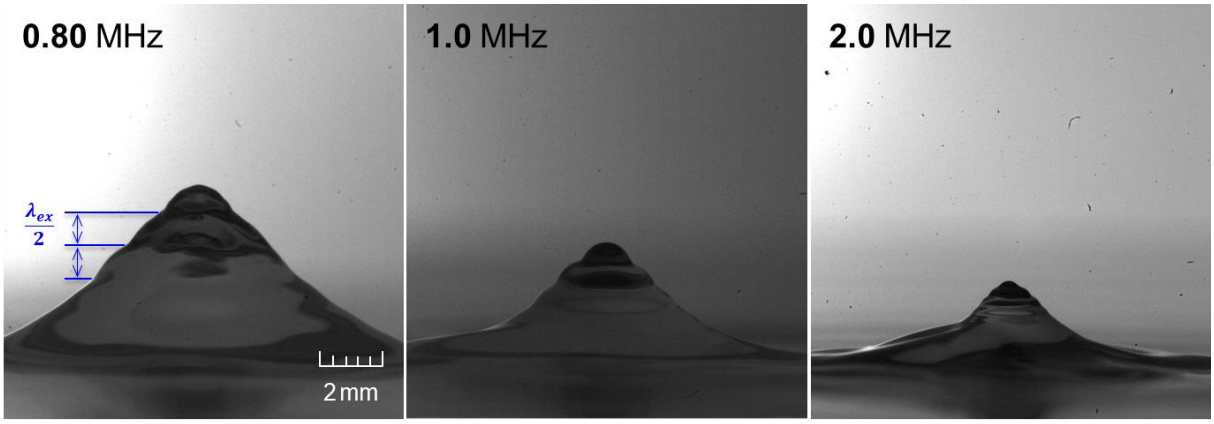

Figure 6.4 Images of the undulation on the surface outline at different driving frequencies.

The *wave-specific* nature—*i.e.*, the characteristic length being strongly dependent on the acoustic wavelength—in a phenomenon of concern, as above, appears to have a playing role in physically describing (almost) every state of the UsA process. In such a description, it is important to realize that the frequency of the ultrasonic wave f_{wave} may not always equal f_{ex}: it has been claimed in the literature that once sufficient instabilities are set in to induce the liquid-column fluctuations observed (in the 3rd state to be described in detail below), there is a tendency to have $f_{wave} = f_{ex}/2$ (*e.g.*, Lang, 1962; Qi *et al.*, 2008)—otherwise $f_{wave} = f_{ex}$ (Tomita, 2014; Simon *et al.*, 2015). In describing the above undulation prevailing in the 2nd state of negligible fluctuating instability, which can be characterized by the vertical span of peak-to-peak distance of the undulation or its pitch, the *two* pitches were found—and are presumed—to correspond to $\lambda_{wave} = v_{wave}/f_{wave}$ where $f_{wave} = f_{ex}$.

Height fluctuations: While a first-sight outline of the 2nd-state protrusion appears stable/steady, detailed observations reveal that its height will start fluctuating with small amplitudes—(indication at least of) an onset of an instability, in addition to its surface undulation. **Figure 6.5** demonstrates typical oscillation patterns exhibited in terms of time-series data/signals for the protrusion/fountain altitude/height and their corresponding FFT outcomes. The periodicity in the height fluctuations appears to be of "quasi-nature." At 0.43 MHz, the signals inherently contain a dominant frequency of 6 Hz (in rather a wider range spanning 6–24 Hz) and 12 Hz (in a much narrower range) for 9 and 10 W/cm^2 [Fig. 6.5(a) and (b)], respectively; the effects of input power density are inconclusive, though some critical shift in periodic trend appears to exist between these two values. As the driving frequency is raised from 0.43 to 0.80, 1.0 and 1.6 MHz, the dominant frequency of height fluctuations tends to increase from 6 to 10, 22 and 54 Hz; the assigned values of the input power density here are irrelevant in discussing the trend for this set of data attaining the 2nd state (see Table 6.1).

Bulk-liquid cavitation: As stated in Section 6.1 repeatedly, obtaining the information regarding the concurrent formation of cavitation—along with the structural transitioning of the free surface from flat to protruding to jetting—should be quite helpful (Simon *et al.*, 2015; Aikawa and Kudo, 2021). While it is extremely difficult in the present study to visually capture any images of cavitation bubbles inside the protuberance, doing so through the bulk liquid above the UsA transducer up to the free surface has been attempted.

Figure 6.6 shows the spatial distribution of bubbles, which should have originated from cavitation, generated within the bulk liquid and captured via side-lighting. Note that two sets of comparisons are made in terms of two-parameters (f_{ex}, I_0) combinations: different f_{ex}'s of 0.43 and 0.80 MHz for a given I_0 of 8 W/cm^2; and different I_0's of 8 and 9 W/cm^2 for a given f_{ex} of 0.80 MHz. In the first series of images (top row), the bubbles appear encircling around the vertical axis of acoustic wave propagation in a standing-wave pattern (for $t \geq 0.93$ ms with t being the time elapsed after having turned on the UsA transducer). As the time has exceeded 1.8 ms, some ripples begin to appear on the liquid surface (not recognizable in the figure); the bubbles then spread out appreciably towards the vessel wall as they approach the free surface ($t \geq 5.0$ ms), prior to the free surface to start rising into a mound (appreciation of the 1st state, 6.3 ms).

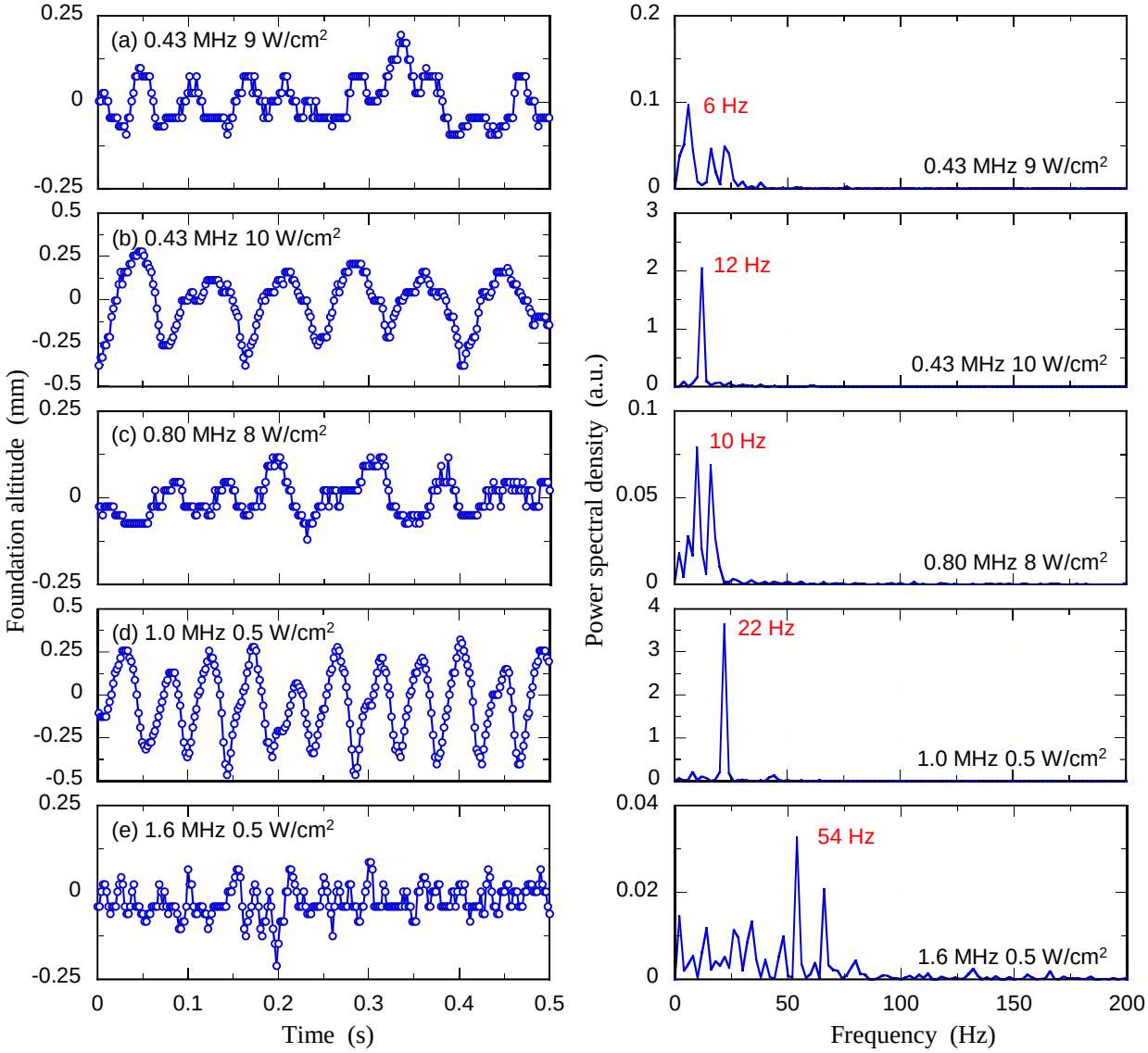

Figure 6.5 Time variations in altitude (or tip height) of acoustic protrusion or (foundation-like) fountain (left) and corresponding outcomes of FFT analysis (right): Set of acoustic parameters (f_{ex}, I_0) specified from (a) to (e).

For the same I_0 (8 W/cm^2) but with f_{ex} increased to 0.80 MHz (middle row), the free-surface rippling was recognizable at 0.4 ms; a bell-shaped mound with some undulation was observed to start developing (at 0.93 ms, 2nd state). In comparison to the first case, some additional information has been obtained: The size of the visible bubbles was significantly reduced at the higher f_{ex}; Despite faint streaks between nodes being identified, the standing-wave structure was clearly disrupted; The bubbles were mainly localized near the transducer with no obvious tendency to spread. Maintaining f_{ex} (0.80 MHz) while increasing I_0 to 9 W/cm^2, a developing protrusion began to appear as early as at 0.12 ms, having resulted in the

solid formation of a beads fountain at 1.92 ms. An apparent structure of the standing wave was no longer identifiable in the images; only randomly dispersed/migrating bubbles of very limited number could be identified closer to the liquid surface. Note that such a series of cavitation-associated behaviors in the bulk liquid would resemble those reported by Lee *et al.* (2011), who investigated the mechanism of liquid flow by monitoring the spatial distribution of visible bubbles, for a similar range of f_{ex} but different I_0 values (see Section 6.1).

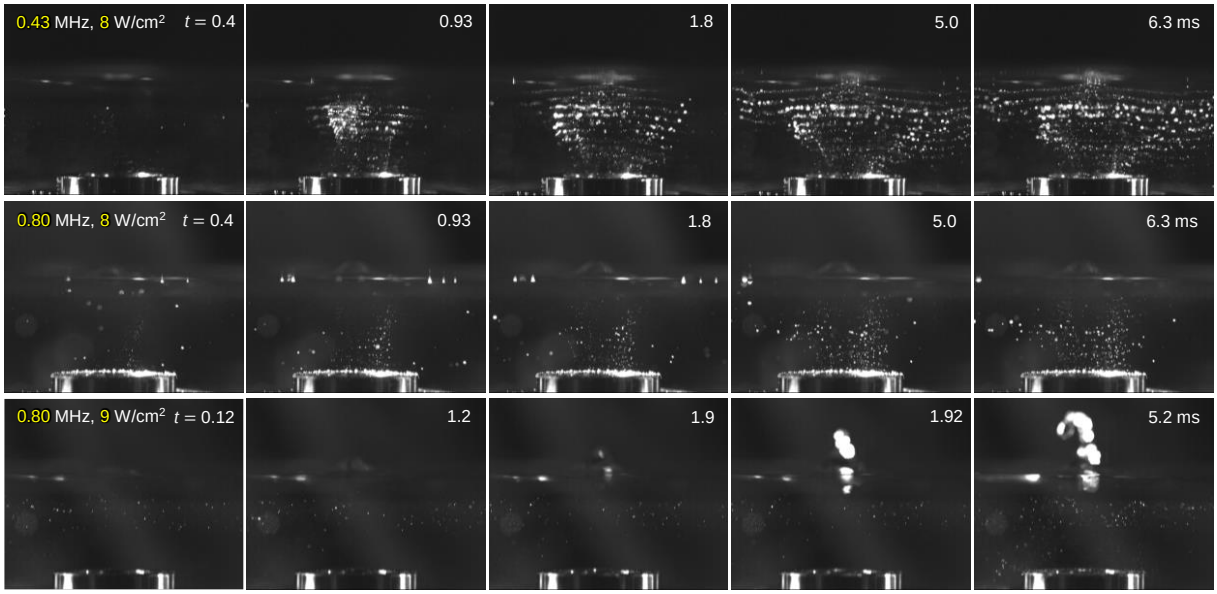

Figure 6.6 Development of the bubble structure in liquid as a function of time for different frequencies.

Further discussion regarding the dynamic behavior of the bulk-phase cavitation bubbles are possible such that: Those visible bubbles would be expelled from the pressure antinodes and become trapped at adjacent pressure nodes due to active bubbles merged by actions of the primary and secondary Bjerknes forces (Lee *et al.*, 2011). The larger bubbles or bubble clusters/clouds generated via coalescence can scatter and attenuate the ultrasound wave (Choil *et al.*, 2019). It is generally known that the size of bubbles will decrease with increasing ultrasound frequency (Leighton, 1994; Laborde *et al.*, 1998; Yasui, 2002; Brotchie *et al.*, 2009; Merouani *et al.*, 2015); in the present study, though, no further attempts in this regard have been made in extended ranges of the acoustic operating conditions. To be somewhat conclusive, however, in light of the difference in bubble flow between 8 and 9 W/cm^2 at 0.80 MHz, it

could be presumed under the present conditions that acoustic streaming is most likely responsible for reaching the instability-associated fountain formation. The large "gap" in the applied power density detected between 0.80 MHz (9 W/cm^2) and 1.0 MHz (1 W/cm^2) further implies that, behind the mechanism of acoustic fountain formation, there could be some "unforeseen" thresholding factor(s) responsible for it, which should be clarified in a future (or the upcoming) work.

6.3.2 Characterization of emanating beads fountain

In regard to a chain of beads emanating out of the foundation-like region [Foundation Region (FR) alone when no appreciable fluctuating instabilities are apparent yet, or Bumpy-Surface Region (BSR) on top of it otherwise; Tsuchiya *et al.*, 2011; Chapter 5], some experimental and model-based findings were made in Chapter 4. The acoustic pair of conditions were confined to f_{ex} = 1–3 MHz mostly and I_0 = 4–6 W/cm^2, in the presence of the stabilizing nozzle, to obtain two quantitative/inherent relationships for: 1) the beads size (d_{bead}) vs. f_{ex} (size specificity) and 2) the beads resonance/natural frequency (f_{bead} or f_n) vs. f_{ex} (periodicity). The present study is to extend the same line of analyses to a wider range of the paired parameters with or without the nozzle equipped.

Minimum driving frequency for triggering beads fountain: One specific aspect to be clarified in this extended work lies in the uncertainty of minimum driving frequency for realizing the beads fountain (3rd state; see Fig. 6.2 and Table 6.1). **Figure 6.7** provides a series of images implying the critical role played by the UsA-driving frequency—over the range f_{ex} = 0.65–3.0 MHz—in the formation of beads fountain. The specificity as well as uncertainty (associated with utilizing the "frequency shifting/tuning capability" provided on the ultrasonic transducer; see Section 6.2) in I_0, on the other hand, is noted to be rather insignificant or even irrelevant over a typical range examined, as reported in Chapter 4. As the driving frequency is increased—except f_{ex} = 0.65 MHz, the beads diameter tends to decrease; the extent of reduction can be clearly seen for $f_{ex} \geq$ 1.0 MHz. It is noteworthy that, for this lowest 0.65 MHz tested, no triggering of beads fountain has been detected (on all the images obtained under the same conditions repeated) even at the highest operational limit tested (I_0 = 10 W/cm^2).

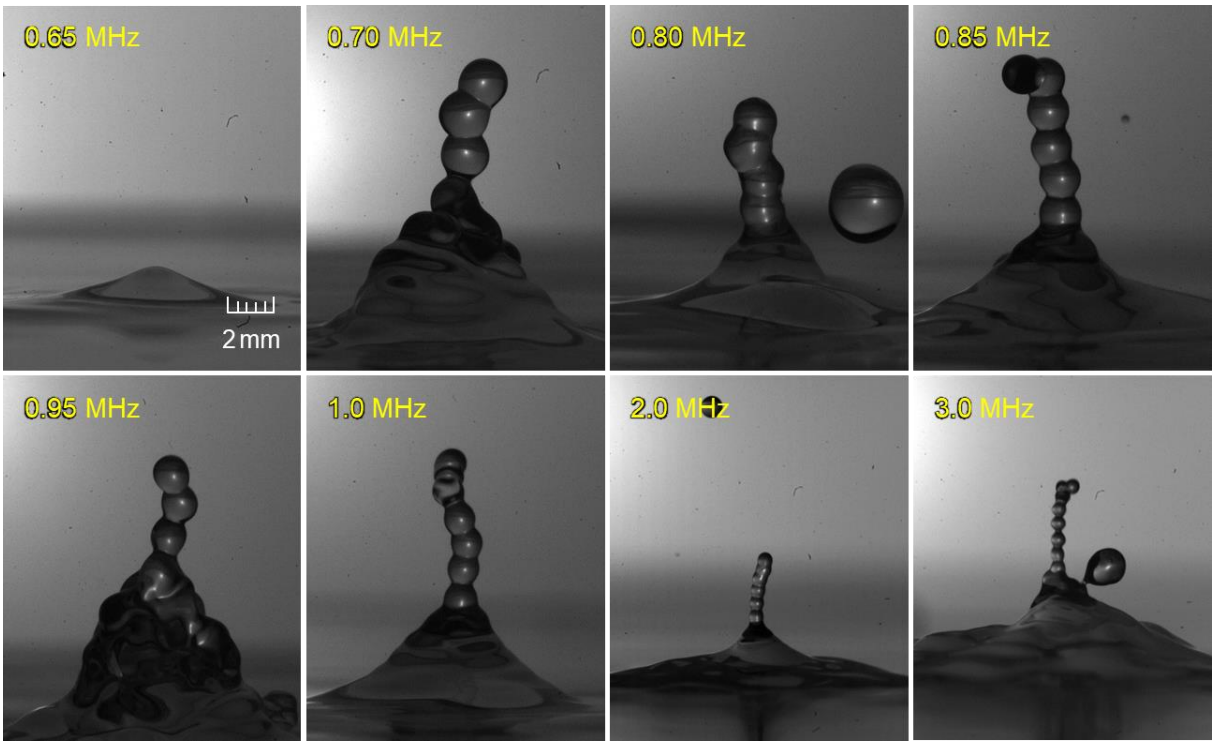

Figure 6.7 Images of beads-like liquid fountain obtained at different driving frequencies.

It is to be noted here that in Chapter 4, We presumed the required frequency should be greater than at least 0.8 MHz, based on their argument that "the characteristic bead diameter d_{bead} should not exceed (or at least comparable to) the capillary length (l_c)":

$$l_c = \sqrt{\sigma/\rho_l g} \tag{6.1}$$

where σ and ρ_l are the surface tension and density of the liquid, respectively, and g the gravitational acceleration. As we argued, with this condition ($d_{bead} > l_c$) met, the gravitational wave would dominate over the surface-tension/capillary wave. For the present 50-wt% ethanol aqueous solution at 25°C, $l_c = 1.80$ mm with the density and surface tension of 902 kg/m^3 and 28.8 mN/m used (Khattab *et al.*, 2012). The characteristic bead diameter, on the other hand, would be estimated—if exists—to be $d_{bead} \cong \lambda_{wave}/2 = \left(\frac{1}{2}\right) 1{,}470/(800\times10^3/2) = 1.84$ mm, thus $d_{bead} > l_c$, for f_{ex} of 0.80 kHz.

Phase-averaged size specificity of beads fountain: **Figure 6.8** shows the average diameter of the fountain beads obtained under each specific condition tested, plotted as a function of the driving frequency; for ease of specific and detailed comparison between every data point, all the obtained values (of standard deviation as well as average) are summarized in **Table 6.2**.

Plotted in log-log scale (to "expand" the lower range of the frequency), the trends exhibited by the experimental data can be well represented by straight lines of slope -1. Such trends, *i.e.*, d_{bead} increases—in line with the hyperbolic variation—with decreasing f_{ex}, can be represented by the physical principle:

$$kd_{bead} \cong \lambda_{wave} = v_{wave}/f_{wave} = kv_{wave}/bf_{ex} \tag{6.2}$$

where two parameters k and b are introduced: the former signifies, as stated above (see Section 6.3.1 concerning the protrusion of concentric circles induced on the free surface), whether the frequency of the ultrasonic wave f_{wave} equals f_{ex} or not; the latter concerns with possible "bifurcation" in d_{bead} whose onset may occur below some critical excitation frequency. Depending on the fluctuating instabilities set in on the protuberance, $k = 2$ if they are sufficient (States 3 and 4) but $k = 1$ otherwise (States 1 and 2).

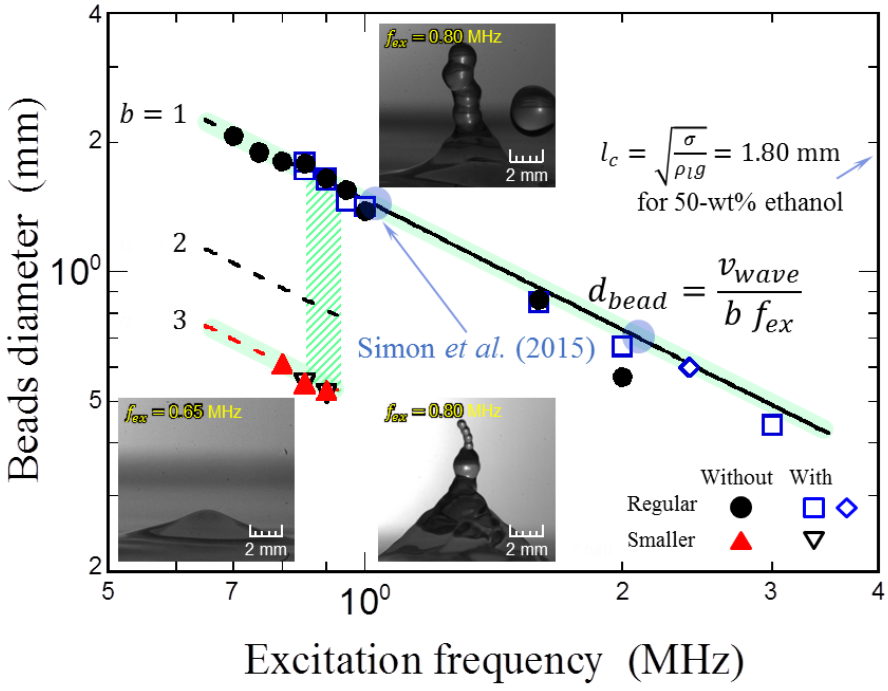

Figure 6.8 Increasing trend in beads diameter with decreasing UsA-driving, or ultrasound-excitation, frequency predicted by simple physical principle (solid straight line); experimental data including both with and without regulating nozzle; and possible bifurcation in the diameter for limited number of data (red dashed line with $b = 3$).

It is to be noted in the figure that the beads diameter appears to be not influenced by the presence/absence of the regulating nozzle equipped. In principle, its value is argued not to exceed the capillary length—in our present ethanol solution $d_{bead} \leq l_c = 1.80\,\text{mm}$. The exper-

imental results indicate that d_{bead} carefully obtained could take a value as high as 2.07 mm at $f_{ex} = 0.70$ MHz. While this largest value of d_{bead} might be in the gravitational-wave (rather than capillary-wave) domain, it could be inferred that the minimum driving frequency discussed in the previous "sub-section" would be as low as 0.7 MHz—in comparison to the preliminary value 0.8 MHz proposed in Chapter 4.

Table 6.2 Diameters of constituent beads varying with driving frequencies

Driving frequency (MHz)	Beads diameter without nozzle (μm)	Beads diameter with nozzle (μm)
0.65	—[a]	—[a]
0.70	2065±37	—[a]
0.75	1902±23	—[a]
0.80	1810±76 610±20	—[a]
0.85 (0.80)	—[b] 551±15	1731±34 547±19
0.85 (1.0)	1792±41	1803±29
0.90 (0.80)	—[b] 533±26	1653±28 516±19
0.90 (1.0)	1662±36	1641±35
0.95 (1.0)	1554±22	1461±50
1.0	1394±25	1420±80
1.6	859±18	850±37
2.0	573±14	670±40
3.0	—[b]	440±25

[a] Not detected below the highest operational limit (10 W/cm^2).
[b] Not detected.

It is also noteworthy in Fig. 6.8 that a separate set of data points shown for the frequencies lower than 0.9–1.0 MHz could be an indication of possible bifurcation, though not providing solid evidence at this stage of data taking, requiring further verification. As a piece of partial evidence, shown in **Fig. 6.9**, beads with diameters of about one-third of the "normal" ones (see the data along the solid line in Fig. 6.8) can be detected concurrently between 0.80 and 0.90 MHz—possible bifurcation into the normal-sized beads [primary beads; $b = 1$ in Eq. (6.2)] and smaller ones (secondary beads; $b = 3$), apparently occurring alternately.

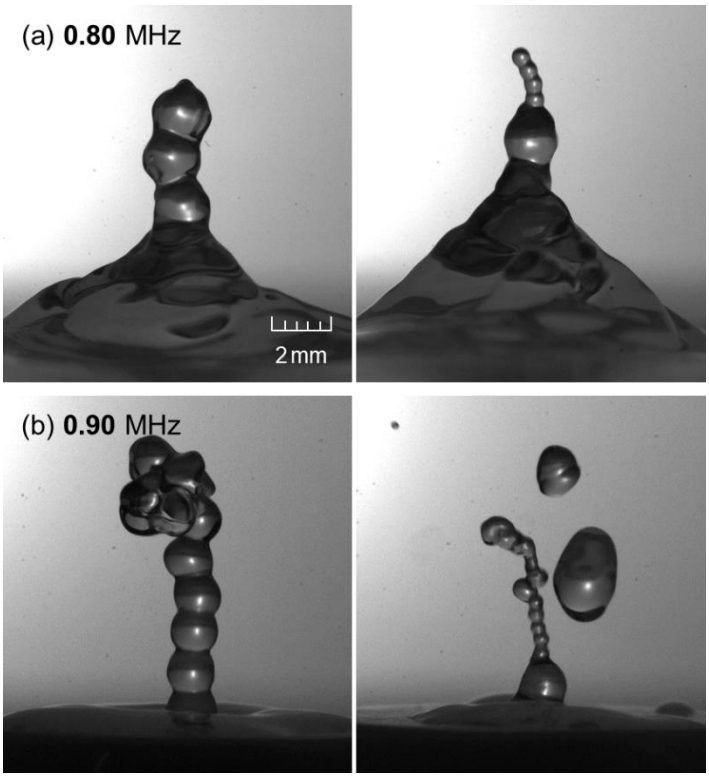

Figure 6.9 Images of two sizes of beads-like liquid fountain obtained at (a) 0.80 MHz and (b) 0.90 MHz (with nozzle).

The appearance of secondary beads is often accompanied by the formation of a single primary beads right above the foundation region; its diameter follows the capillary length. The following hypothesis has been made regarding secondary beads formation: When the driving frequency is at a critical threshold, the highly excited radial oscillations become unstable causing the acoustic radiation force to be insufficient to support the stable formation of a beads fountain. At this point, the drop of the primary bead acts as an energy concentrator, and the acoustic radiation pressure is effectively trapped inside the drop and focused towards the tip, resulting in a secondary bead of roughly one-third the diameter of the primary bead. We hypothesize that the ultrasonic threshold for instability is a transition of the dominant mechanism leading to fountain formation—from acoustic radiation pressure to streaming. Although the present experimental data do not directly prove the relationship between the secondary beads and the primary bead but can at least suggest that the secondary beads are related to the capillary wavelength.

6.4 Concluding Remarks

Upon ultrasonic irradiation under a wide range of operating conditions—driving frequencies of 0.43–3.0 MHz and input power densities of 0.5–10 W/cm^2, the UsA fountain can be differentiated into four formation mechanisms: 1) the *onset* of a protrusion on otherwise flat free surface; 2) the *appearance* of undulation along the growing protuberance; 3) the *triggering* of emanating beads fountain out of this foundation-like region; and 4) the *induction* of droplets bursting and/or mist spreading. A qualitative determination of the four representative transition/demarcation acoustic thresholds was performed by visually tracing their outline.

The undulation height of the protrusion is equivalent to half the UsA wavelength, and the periodicity of the undulation height can be characterized by the dominant frequency obtained (FFT-evaluated) experimentally. The bead diameter is found to almost coincide with *half* the UsA wavelength, which can be specified by *half* the UsA excitation/driving frequency, and independent of the presence of the nozzle. The driving frequency threshold for bead fountain formation is 0.7 MHz.

As observed between 0.8 and 1.0 MHz, a significant difference in input power density was observed for beads fountain. This indicates that a boundary may exist for the formation of liquid fountains, and at this bifurcation, there may be a sudden qualitative or topological change in the beads fountain behavior.

References

Aikawa, T. and N. Kudo, "Relation between thresholds of free radical generation and atomization under ultrasound exposure," *Jpn. J. Appl. Phys.*, **60**, SDDD13 (2021). http://doi.org/10.35848/1347-4065/abf600.

Barreras, F., H. Amaveda and A. Lozano, "Transient high-frequency ultrasonic water atomization," *Exp. Fluids*, **33** 405–413 (2002). https://doi.org/10.1007/S00348-002-0456-1.

Blamey, J., L.Y. Yeo and J.R. Friend, "Microscale capillary wave turbulence excited by high frequency vibration," *Langmuir*, **29**, 3835–3845 (2013). https://doi.org/10.1021/la304608a.

Boguslavskii, Yu.Ya. and O.K. Eknadiosyants, "Physical mechanism of the acoustic

atomization of a liquid," *Sov. Phys. Acoust.*, **15** 14–21 (1969).

Bouwhuis, W., K. G. Winkels, I. R. Peters, P. Brunet, D. van der Meer and J. H. Snoeijer, "Oscillating and star-shaped drops levitated by an airflow," *Phys. Rev. E*, **88**, 023017 (2013). https://doi.org/10.1103/PhysRevE.88.023017.

Brotchie, A, F. Grieser and M. Ashokkuma, "Effect of power and frequency on bubble-size distributions in acoustic cavitation," *Phy. Rve. Lett*, **102**, 5084302 (2009). https://doi.org/10.1103/PhysRevLett.102.084302.

Choi, J., J. Khim, B. Neppolian and Y. Son, "Enhancement of sonochemical oxidation reactions using air sparging in a 36 kHz sonoreactor," *Ultrason. Sonochem.*, **51**, 412–418 (2019). https://doi.org/10.1016/j.ultsonch.2018.07.032.

Collins, D. J., O. Manor, A. Winkler, H. Schmidt, J. R. Friend and L.Y. Yeo, "Atomization off thin water films generated by high-frequency substrate wave vibrations," *Phys. Rev. E*, **86**, 056312 (2012). https://doi.org/10.1103/PhysRevE.86.056312.

Fujita, K. and K. Tsuchiya, "Cavitating bubble inside liquid fountain of beads associated with ultrasonic atomization," *Proc. 8th Int. Conf. Multiphase Flow (ICMF 2013)*, Paper 863/1–5 (2013).

Inui, A., A. Honda, S. Yamanaka, T. Ikeno and K. Yamamoto, "Effect of ultrasonic frequency and surfactant addition on microcapsule destruction," *Ultrason. Sonochem.*, **70**, 105308 (2021). https://doi.org/10.1016/j.ultsonch.2020.105308.

Khattab, I. S., F. Bandarkar, M. A. A. Fakhree and A. Jouyban, "Density, viscosity, and surface tension of water–ethanol mixtures from 293 to 323K," *Korean J. Chem. Eng.*, **29**, 812–817 (2012). https://doi.org/10.1007/s11814-011-0239-6.

Kim, G., S. Cheng, L. Hong, J.-T. Kim, K. C. Li and L. P. Chamorro, "On the acoustic fountain types and flow induced with focused ultrasound," *J. Fluid Mech.*, **909**, R2 (2021). http://doi.org/10.1017/jfm.2020.1012.

Kirpalani, D. M. and F. Toll, "Revealing the physicochemical mechanism for ultrasonic separation of alcohol–water mixtures," *J. Chem. Phys.*, **117**, 3874–3877 (2002). https://doi.org/10.1063/1.1495849.

Kobara, H., M. Tamiya, A. Wakisaka, T. Fukazu and K. Matsuura, "Relationship between the size of mist droplets and ethanol condensation efficiency at ultrasonic atomization on

ethanol–water mixtures," *AIChE J.*, **56**, 810–814 (2010). https://doi.org/10.1002/aic.12008.

Kojima, Y., Y. Asakura, G. Sugiyama and S. Koda, "The effects of acoustic flow and mechanical flow on the sonochemical efficiency in a rectangular sonochemical reactor," *Ultrason. Sonochem.*, **17**, 978–984 (2010). https://doi.org/10.1016/j.ultsonch.2009.11.020.

Kudo, T., K. Sekiguchi, K. Sankoda, N. Namiki and S. Nii, "Effect of ultrasonic frequency on size distributions of nanosized mist generated by ultrasonic atomization," *Ultrason. Sonochem.*, **37**, 16–22 (2017). https://doi.org/10.1016/j.ultsonch.2016.12.019.

Laborde, J.-L, C. Bouyer, J.-P. Caltagirone and A. Gérard, "Acoustic cavitation field prediction at low and high frequency ultrasound," *Ultrasonics*, **36**, 581–587 (1998). https://doi.org/10.1016/S0041-624X(97)00106-6.

Lang, R. J., "Ultrasonic atomization of liquids," *J. Acoust. Soc. Am.*, **34**, 6–8 (1962). https://doi.org/10.1121/1.1909020.

Lee, J., K. Yasui, T. Tuziuti, T. Kozuka, A. Towata and Y. Iida, "Spatial distribution enhancement of sonoluminescence activity by altering sonication and solution conditions," *J. Phys. Chem. B*, **112**, 15333–15341 (2008). https://doi.org/10.1021/jp8060224.

Lee, J., M. Ashokkumar, K. Yasui, T. Tuziuti, T. Kozuka, A. Towata and Y. Iida, "Development and optimization of acoustic bubble structures at high frequencies," *Ultrason. Sonochem.*, **18**, 92–98 (2011). https://doi.org/10.1016/j.ultsonch.2010.03.004.

Leighton, T., *The acoustic bubble*, Academic Press, London, UK (1994). https://doi.org/10.1016/B978-0-12-441920-9.X5001-9.

Merouani, S., H. Ferkous, O. Hamdaoui, Y. Rezgui and M. Guemini, "A method for predicting the number of active bubbles in sonochemical reactors," *Ultrason. Sonochem.*, **22**, 51–58 (2015). https://doi.org/10.1016/j.ultsonch.2014.07.015.

Mijaković, M., B. Kežić, L. Zoranić, F. Sokolić, A. Asenbaum, C. Pruner, E. Wilhelm and A. Perera, "Ethanol–water mixtures; ultrasonics, Brillouin scattering and molecular dynamics," *J. Mol. Liq.*, **164**, 66–73 (2011). https://doi.org/10.1016/j.molliq.2011.06.009.

Neppiras, E. A. and B. E. Noltingk, "Cavitation produced by ultrasonics: theoretical conditions for the onset of cavitation," *Proc. Phys. Soc. B*, **64**, 1032–1038 (1951). https://doi.org/10.1088/0370-1301/64/12/302.

Nii, S. and N. Oka, “Size-selective separation of submicron particles in suspensions with ultrasonic atomization,” *Ultrason. Sonochem.*, **21**, 2032–2036 (2014). http://doi.org/10.1016/j.ultsonch.2014.03.033.

Orisaki, M. and T. Kajishima, “Numerical analysis of water surface rising caused by underwater ultrasonic wave,” *Trans. JSME* (in Japanese), **88**, 21-00377 (2022). https://doi.org/10.1299/transjsme.21-00377.

Qi, A., L.Y. Yeo and J.R. Friend, “Interfacial destabilization and atomization driven by surface acoustic waves,” *Phys. Fluids*, **20**, 074103 (2008). https://doi.org/10.1063/1.2953537.

Ramisetty, K.A., A.B. Pandit and P.R. Gogate, “Investigations into ultrasound induced atomization,” *Ultrason. Sonochem.*, **20**, 254–264 (2013). https://doi.org/10.1016/j.ultsonch.2012.05.001.

Rozenberg, L.D. (Ed.), “Physical principles of ultrasonic technology,” **2**, 4–88 Springer (1973).

Sato, M., K. Matsuura and T. Fujii, “Ethanol separation from ethanol–water solution by ultrasonic atomization and its proposed mechanism based on parametric decay instability of capillary wave,” *J. Chem. Phys.*, **114**, 2382–2386 (2001). https://doi.org/10.1063/1.1336842.

Sekiguchi, K., D. Noshiroya, M. Handa, K. Yamamoto, K. Sakamoto and N. Namiki, “Degradation of organic gases using ultrasonic mist generated from TiO_2 suspension,” *Chemosphere*, **81**, 33–38 (2010). https://doi.org/10.1016/j.chemosphere.2010.07.009.

Shen, C.L., W.J. Xie and B.Wei, “Parametrically excited sectorial oscillation of liquid drops floating in ultrasound,” *Phys. Rev. E*, **81**, 046305 (2010). https://doi.org/10.1103/PhysRevE.81.046305.

Simon, J.C., O.A. Sapozhnikov, V.A. Khokhlova, L.A. Crum and M.R. Bailey, “Ultrasonic atomization of liquids in drop-chain acoustic fountains,” *J. Fluid Mech.*, **766**, 129–146 (2015). https://doi.org/10.1017/jfm.2015.11.

Simon, J.C., O.A. Sapozhnikov, V.A. Khokhlova, Y.-N. Wang, L.A. Crum and M.R. Bailey, “Ultrasonic atomization of tissue and its role in tissue fractionation by high intensity focused ultrasound,” *Phys. Med. Biol.*, **57**, 8061–8078 (2012). https://doi.org/10.1088/0031-9155/57/23/8061.

Son, Y., M. Lim, M. Ashokkumar and J. Khim, “Geometric optimization of sonoreactors for the enhancement of sonochemical activity,” *J. Phys. Chem. C*, **115**, 4096–4103 (2011). https://doi.org/10.1021/jp110319y.

Tomita, Y., “Jet atomization and cavitation induced by interactions between focused ultrasound and a water surface,” *Phys. Fluids*, **26**, 097105 (2014). https://doi.org/10.1063/1.4895902.

Tsuchiya, K., H. Hayashi, K. Fujiwara and K. Matsuura, “Visual analysis of ultrasonic atomization and its associated phenomena,” *Earozoru Kenkyu* (*J. Aerosol Res.* in Japanese), **26**, 11–17 (2011). https://doi.org/10.11203/jar.26.11.

Watanabe, A., K. Hasegawa and Y. Abe, “Contactless fluid manipulation in air: droplet coalescence and active mixing by acoustic levitation,” *Sci. Rep.*, **8**, 10221 (2018). https://doi.org/10.1038/s41598-018-28451-5.

Xu, Z., K. Yasuda and X. Liu, “Simulation of the formation and characteristics of ultrasonic fountain,” *Ultrason. Sonochem.*, **32**, 241–246 (2016). http://doi.org/10.1016/j.ultsonch.2016.03.016.

Yasui, K., “Influence of ultrasonic frequency on multibubble sonoluminescnece,” *J. Acoust. Soc. Am.*, **112**, 1405–1413 (2002). https://doi.org/10.1121/1.1502898.

Zhang, H., X. Zhang, X. Yi, F. He, F. Niu and P. Hao, “Dynamic behaviors of droplets impacting on ultrasonically vibrating surfaces,” *Exp. Therm. Fluid Sci.*, **112**, 110019 (2020). https://doi.org/10.1016/j.expthermflusci.2019.110019.

Chapter 7

Concluding remarks

7.1 Conclusions

This study is claimed to be the dynamic elucidation through a sequence of images, captured through high-speed, high-resolution visualization, of the periodically oscillating acoustic fountain, as well as the quantitative evaluation of the effect of acousto-related operating conditions on the structure and dynamics of the fountain and an attempt to reveal factor(s) triggering mist emergence via experimental frequency analysis and theoretical prediction, respectively.

To avoid the avoided complexities involved in the fountain dynamics with droplets bursting and mist spreading—once the input power is raised. our first attempt at resolving this problem was to reduce the input power and equip the regulating nozzle so as to maintain the stability of the beads fountain. Chapter 4 deals with quantitatively elucidating the effects of the UsA driving frequency on the structure [including characteristic dimension(s)] and dynamics [viz., characteristic frequency(ies)] of a chain-of-beads fountain realized under lower input power intensity. Upon ultrasonic irradiation—driving frequencies of 1–3 MHz and input power densities of 3–6 W/cm^2, the UsA fountain takes the form of a chain of "beads" in contact, recurring steadily. The recurring beads themselves are characterized by the UsA wave-inherent, "effective" dimension. This effective beads diameter is found to almost coincide with half the UsA wavelength, which can be specified by half the UsA excitation/driving frequency. This predictive scheme is realized via physical principle that the wavelength decreases in inverse proportion to the increasing frequency for a given liquid (thus for a fixed ultrasound speed). The scheme appears to hold as long as the beads diameter will not exceed the capillary length. The cyclic properties of the UsA beads fountain, visually exhibited via high-speed imaging, are characterized by the dominant frequency obtained (FFT-evaluated) experimentally. This primary periodicity is found to be well predicted based on the simple theoretical model proposed by Rayleigh (1879) with a proper assignment of the mode of cyclic deformation of the fountain beads themselves. It is further found that such dynamics in (time-

series data for) the fountain structure at given height(s) along a series of beads would *signal* "bursting" of liquid droplets emanating out of a highly deformed bead often followed by a cloud of tiny droplets, or mist. In particular, the time–frequency analysis, via DWT, revealed that bursting appears to be not a completely random phenomenon but should concur with the fountain periodicity with a limited extent of probability.

In Chapter 5, we used a transducer with driving frequency of 2.4 MHz, which is commonly used in ultrasonic atomization technology. In general, If the installation angle/direction is exactly vertical, *viz.*, the transducer disk parallel to (or its angle being 0° vs.) the horizontal free surface, the acoustic fountain will be disturbed rather profoundly—directly by relatively large drops of liquid separated from the fountain tip and then falling or indirectly by the associated undulation of the surrounding free surface. To solve this problem, we applied high-speed imaging/image processing to observe/analyze detailed dynamics of the acoustic fountain by changing the angle of ultrasonic irradiation. For ultrasound irradiated out of the transducer used with its installation angles ranging 0°–6° or higher (up to 10° examined) and input power densities of 3.5–6.5 W/cm^2, the UsA fountain will exhibit a sequence of oscillating/ intermit-tent features. As the extent of tilt (from the vertical direction) in the irradiation angle was increased, the degree of occurrence of mist generation and the amount of identifiable mist generated would decrease. This trend was associated with reduction in both the growth rate and breakup frequency of the fountain on the tilt. In line with such axial extents of growth and breakup of the fountain, both taking maximum values at the transducer installation angle of 2°, its optimum value should be recommended to be slightly tilted 2° from the viewpoint of stability of the UsA fountain and not to exceed 5° from that of effective mist generation. The atomization, or mist generation, is mostly—almost exclusively—triggered and enhanced as the laterally swinging fountain comes across the direction of irradiation, more specifically, with its inclined angle being shifted from positive to negative in the 0°±5° range. It is further found, through the analysis of time variation in the resulting angle of liquid-fountain inclination, that the swinging fountain fluctuates periodically in an *asymmetric* manner and its periodicity can fairly be predicted based on a simple "pendulum" model proposed. Thus, A slight tilt in irradiation of ultrasound should be of advantages in both operational and mist- generating performances. The acoustic liquid fountain will become improved in its operability/stability by

avoiding the disruption of oscillation rhythm of the fountain from vertically interacting tip-separated drops.

Chapter 6 focuses on the process of ultrasonic atomization involves a series of dynamic/topological deformations of free surface realized by changing some acousto-related operating conditions, including ultrasound excitation frequency, acoustic strength or input power density, and the presence/absence of a "regulating" nozzle. By utilizing high-speed, high-resolution images, UsA fountains could be qualitatively identified as four representative transitions/demarcations: 1) the onset of a protrusion on otherwise flat free surface; 2) the appearance of undulation along the growing protuberance; 3) the triggering of emanating beads fountain out of this foundation-like region; and 4) the induction of droplets bursting and/or mist spreading. On the basis of Chapter 4, quantitatively examined were the two parameters specification—for the degrees as well as induction—of the periodicity in the protrusion-surface and beads-fountain oscillations, observed over wider range of driving/excitation frequencies (0.43–3.0 MHz) and input power densities (0.5–10 W/cm^2) of ultrasonic transducers with or without the stabilizing nozzle equipped. The resulting time variations for the extended operating ranges in the "measured" fountain structure, associated with the recurring-beads size "scalable" to the ultrasound wavelength, confirm the wave nature predictable from simple physical principle. Specifically, the thresholds in acoustic conditions for each of the four transition states of the fountain structure have been identified; in particular, the onset of possible "bifurcation" in the chain-beads diameter below a critical excitation frequency.

The ultimate goal of this project is to be able to predict mist generation from the periodicity of fountain oscillations, which will improve the practicality of atomization. The lower input power and equip the regulating nozzle so as to maintain the stability of the beads fountain. The steady formation of beads fountain would allow us to apply Rayleigh's theory. While it is failed to make any quantitative prediction about droplets bursting or mist spreading, we have found that the atomization of the fountain should be closely related to the higher-order deformation of the beads and the droplet/mist is not a completely random phenomenon. For higher-power ultrasonic irradiation, an optimal tilt angle of 2° is proposed, which will improve fountain stability and potentially increase the frequency of atomization occurs. In addition, the quantitative prediction of the oscillation frequency of the fountain provides a basis

for the quantitative prediction of mist generation. In future work, it is necessary to discuss how to quantify the amount of mist generated by the fountain during a single swing period. This will open up new possibilities in further investigating ultrasonic atomization.

7.2 Publication list

Wang, X., Y. Mori and K. Tsuchiya, “Periodicity in ultrasonic atomization involving beads-fountain oscillations and mist generation: Effects of driving frequency,” *Ultrason. Sonochem.*, **86**, 105997 (2022). https://doi.org/10.1016/j.ultsonch.2022.105997.

Wang, X. and K. Tsuchiya, “Frequency specificity of liquid-fountain swinging with mist generation: Effects of ultrasonic irradiation angle,” *Fluids*, **7**, 306 (2022). https://doi.org/10.3390/fludis7090306.

Tsuchiya, K. and X. Wang, “Ultrasonic atomization—from onset of protruding free surface to emanating beads fountain—leading to mist spreading,” *Chem. Eng. Sci.*, (Submitted).

Acknowledgment

It is my great pleasure to express my deep gratitude to Professor K. Tsuchiya, my supervisor, who has helped me in these 10 years from my bachelor's to my Ph.D. studies here in Japan, for his patient guidance, enthusiastic encouragement, and useful critiques of my research. During our conversations, I received more life advice than just research insights. The positive attitude he has and the knowledge he shares strongly influence me.

I would like to thank Professor Y. Mori for his kind support and valuable advice on research. I wish to thank Drs. Z. Cao, S. Zou, W. Zhang, Y. Zheng and Q. Mao for giving me much constructive advice during my Ph.D. studies.

Thank you also to my colleagues, all members in Tsuchiya's lab. With their company, I spent a very beatific life in Japan. I would also like to thank my friends, D. Yu, M. Wen, H. Zhao and E. Chen for taking care of me throughout my daily life, which gives me the strength to continue my studies.

A special thanks should be given to my boyfriend, T. Zhang, and his family for supporting my choice and dream.

Finally, I wish to thank my family members for their love, support, patience and encouragement throughout my study.

Xaiolu WANG

March, 2023

Kyoto, Japan